PHOTOCATALYTIC DEGRADATION OF PARACETAMOL ON NITROGEN-DOPED CARBON DOTS / TITANIUM DIOXIDE PHOTOCATALYTIC MEMBRANE UNDER VISIBLE LIGHT IRRADIATION

KHOR JIA XUAN

A project report submitted in partial fulfilment of the requirements for the award of Bachelor of Engineering (Honours) Chemical Engineering

Lee Kong Chian Faculty of Engineering and Science
Universiti Tunku Abdul Rahman

April 2020

DECLARATION

I hereby declare that this project report is based on my original work except for citations and quotations which have been duly acknowledged. I also declare that it has not been previously and concurrently submitted for any other degree or award at UTAR or other institutions.

Signature :

Name : Khor Jia Xuan

ID No. : 1504238

Date : 27 April 2020

APPROVAL FOR SUBMISSION

I certify that this project report entitled **“PHOTOCATALYTIC DEGRADATION OF PARACETAMOL ON NITROGEN-DOPED CARBON DOTS / TITANIUM DIOXIDE PHOTOCATALYTIC MEMBRANE UNDER VISIBLE LIGHT IRRADIATION”** was prepared by **KHOR JIA XUAN** has met the required standard for submission in partial fulfilment of the requirements for the award of Bachelor of Engineering (Honours) Chemical Engineering at Universiti Tunku Abdul Rahman.

Approved by,

Signature :

Supervisor : Ir. Dr. Chong Woon Chan

Date : 27 April 2020

ACKNOWLEDGEMENTS

I offer my sincere appreciation to Universiti Tunku Abdul Rahman (UTAR) for the opportunity to learn and involve in this research. My deep sense of gratitude goes to my research supervisor, Ir. Dr. Chong Woon Chan for her enormous patience, thoughtful guidance and insightful advices throughout the development of my research. Her immense knowledge and constructive suggestions had guided me to complete this research successfully. Without her guidance and supervision, this research would not have been possible.

I would also like to take this opportunity to thank the lab staffs in UTAR for their heartfelt patience and guidance in operating the lab equipment. Furthermore, I would like to thank my friends who directly or indirectly helped me throughout my research period. Special thanks to my senior, Heng Zeng Wei and my research’s associate, Lien Sook Hui. This project would not be completed without their assistance and collaboration.

Lastly, I would like to express my deepest gratitude to my beloved parents for their profound love and encouragement whenever I faced difficulties throughout this period.

ABSTRACT

Paracetamol is a common component contains in various analgesic medicines. It is often detected as a pharmaceutical waste in water sources due to its wide applications in the production of medicine. The removal of paracetamol from water sources is challenging due to its non-biodegradable property and low concentration in water bodies. Hence, this research was conducted to study the photocatalytic degradation of paracetamol by using hybrid nitrogen-doped carbon dots/titanium dioxide (N-CDs/TiO_2) photocatalyst under visible light. To eliminate the recycling step of the hybrid photocatalyst, chemical grafting was employed to attach the hybrid photocatalyst on membrane surface to produce photocatalytic membrane. Firstly, hydrothermal technique was used to synthesize the N-CDs solution from oil palm fronds. The prepared N-CDs solution was incorporated with pure anatase phase TiO_2 by using the ex-situ hydrothermal method in four different loadings of N-CDs (1, 2, 3 and 4 mL). The hybrid photocatalyst with 3 mL N-CDs loading showed the best photocatalytic degradation of paracetamol with an outstanding rate constant of 0.0187 min^{-1}. This hybrid photocatalyst was therefore chosen for the fabrication of photocatalytic membrane. To fabricate the photocatalytic membrane, different loadings (0.1, 0.2 and 0.3 wt%) of the hybrid photocatalyst were chemically grafted on polyethersulfone (PES) membrane with 1.0 wt% PVP by using polyacrylic acid (PAA) monomer, ethylene glycol (EG) as the cross-linker and potassium persulfate (PP) as the initiator. Based on the photocatalytic degradation study on paracetamol, photocatalytic membrane with the highest loading of hybrid photocatalyst (0.3 wt%) showed the best photocatalytic activity at a rate of 0.0028 min^{-1}. However, the permeability of photocatalytic membrane plunged due to the alteration of membrane morphology by the grafted PAA monomer. The synthesized photocatalysts were characterized by using X-ray diffraction (XRD) analysis, Fourier transform infrared (FTIR) spectrometer, zeta potential analysis, scanning electron microspocy (SEM) and energy dispersive X-ray (EDX) spectroscopy to study their crystallographic phases, functional groups, surface charges and morphologies respectively. Meanwhile, FTIR and SEM analyses were conducted to identify the functional groups and morphologies of the fabricated membranes. This study showed that by immobilizing 0.3 wt% of the synthesized hybrid photocatalyst with the optimum amount of 3 mL N-CDs loading to PES membrane by using chemical grafting method, the fabricated photocatalytic membrane demonstrated great potential in the removal of paracetamol under the irradiation of visible light.

TABLE OF CONTENTS

CHAPTER

1 INTRODUCTION

2 LITERATURE REVIEW

3 METHODOLOGY AND WORK PLAN

4 RESULTS AND DISCUSSIONS

5 CONCLUSIONS AND RECOMMENDATIONS

LIST OF TABLES

LIST OF FIGURES

LIST OF SYMBOLS / ABBREVIATIONS

Δt	permeation time, h
A	area of membrane, 0.00146 m^2
Abs_f	final absorption of paracetamol solution
Abs_i	initial absorption of paracetamol solution
C	final paracetamol concentration
C_o	initial paracetamol concentration
D	crystallite size
E_g	band gap, eV
G	grafting yield, %
J	pure water flux, L/m^2h
k	photocatalytic rate constant
K	Scherrer's constant
M	mass gain, %
m	mass of permeate, kg
m_c	mass of photocatalysts added to dipping solution, g
m_f	mass of grafted and dried membrane, g
m_i	mass of membrane before grafting, g
t	irradiation time
V	volume of permeated water, L
$e-$	electron
$h+$	hole
λ	wavelength
β	peak width
θ	angle between beam and normal to the reflecting plane
ρ	density of water, 997 kg/m^3
BET	Brunner-Emmet-Teller
CDs	carbon dots
CMC	carboxymethylcellulose
CNB	remazol black XP
CRB	coralline red BS

DSC	dye-sensitized solar cells
EDA	ethylenediamine
EDX	Energy Dispersive X-ray Spectroscopy
EFB	empty fruit bunch
EG	ethylene glycol
FTIR	Fourier Transforms Infrared Spectrometer
FWHM	full-width-half-maximum
HOMO	highest occupied molecular orbital
HPC	hybrid photocatalyst
ID	inner diameter
IPA	isopropanol
LUMO	lowest unoccupied molecular orbital
MB	methylene blue
MF	microfiltration
MG	malachite green
NF	nanofiltration
NMP	*N*-methyl-2-pyrrolidone
OD	outer diameter
OPF	oil palm frond
OPT	oil palm trunk
PA	polyamide
PAA	polyacrylic acid
PAN	polyacrylonitrile
PES	polyethersulfone
PESBM	polyethersulfone bare membrane
PESPCM	polyethersulfone photocatalytic membrane
PET	polyethylene terephthalate
PL	photoluminescence
PP	potassium persulfate
PSF	polysulfone
PTFE	polytetrafluoroethylene
PVDF	polyvinylidene fluoride
PVP	polyvinylpyrrolidone
PWF	pure water flux

QCE	quantum confinement effect
R	organic pollutant
RBX	reactive brilliant red X-3BS
RhB	rhodamine
SEM	Scanning Electron Microscopy
SWNT	single-walled carbon nanotubes
TC	tetracycline
TEM	transmission electron microscopy
TiO_2	titanium dioxide
TMP	transmembrane pressure, bar
TTIP	titanium tetraisopropoxide
UCPL	up-converted photoluminescence
UF	ultrafiltration
UV	ultraviolet
XRD	X-ray Diffraction

LIST OF APPENDICES

CHAPTER 1

INTRODUCTION

1.1 Pharmaceutical Waste in Water Source

Along with the industrial development and advancement in technology, sustainable development becomes an important aspect that must be taken into consideration to ensure the improvement of human life without compromising the quality of environment. Environmental pollution has been a major issue and water pollution is one of the most problematic pollution as it affects the aquatic habitat as well as the quality of drinking water (Saranya and Nithyanandhi, 2017).

Pharmaceutical waste has becoming an alarming issue to the public due to their negative impacts to the aquatic organisms even if it presents in trace amount (Saranya and Nithyanandhi, 2017). These pharmaceutical drugs enter the water system via various sources such as hospital and health centre wastewater, domestic or industrial discharges, as well as from the disposal of unused drugs and drug manufacturing wastes that leach into water through landfill. Along with the increasing practice of reuse water due to water scarcity, the concentration of pharmaceutical content in water is expected to increase due to the accumulation of pharmaceutical content in the water if it is not well-treated (Saranya and Nithyanandhi, 2017).

Among various pharmaceutical wastes, paracetamol which is also known as acetaminophen, is a common component found in a wide variety of medicines due to its analgesic and antipyretic properties (Dalgic et al., 2017). Hence, it is chosen as the pharmaceutical waste sample in this research. The molecular structure of paracetamol is shown in Figure 1.1.

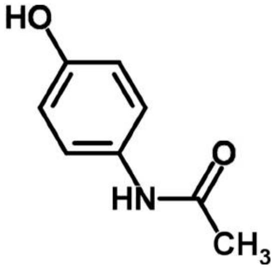

Figure 1.1: Molecular Structure of Paracetamol.

Ranking as one of the top three drugs prescribed in England, paracetamol is often detected in water system due to its wide applications (Jallouli et al., 2017). Concentration of paracetamol ranges from less than 0.01 μg/L up to approximately 200 μg/L, depending on the sources of water (Al-Kaf et al., 2017). In Malaysia, 0.07 μg/L of paracetamol was detected in the effluent of sewage treatment plant in Kajang, Selangor in April 2009 (Al-Odaini et al., 2010).

Conventional wastewater treatment method such as the use of activated sludge alone is inefficient to remove active pharmaceutical components in water. Several pharmaceutical waste treatment methods such as electro-coagulation, advance biological method, adsorption, oxidation and photocatalytic degradation have been researched and practised to remove pharmaceutical constituents from water (Ahmadi et al., 2017). However, the removal of pharmaceutical components from waterwater is fairly complex due to the existence of non-biodegradable solvents and salinity content in the waste (Saranya and Nithyanandhi, 2017). Recently, photocatalytic degradation process with the use of carbon dots has been studied extensively in removing pharmaceutical components from the water due to its facile operation, excellent functionality and relatively lower cost (Ahmadi et al., 2017).

1.2 Carbon Dots

Carbon dots (CDs) are newly discovered carbon-based nanomaterials that generally characterized by their distinct, quasi-spherical nanoparticles with sizes smaller than 10 nm. CDs were first formed by accident during the purification of single-walled carbon nanotubes (SWNT) through a preparative electrophoretic method conducted by Xu et al. in 2004. Separated from the arc discharge carbon soot, a by-product was produced during the process and was found to possess high fluorescent characteristic in different colours under ultraviolet (UV) light with 365 nm. This fluorescent nanomaterial was documented as the name of carbon dots (CDs) after two years of the discovery and boosted widespread of interests after the synthesis of CDs by Sun et al. (2006). Figure 1.2 shows the CDs produced from the purification of SWNT, possessing fluorescent properties under UV light radiation.

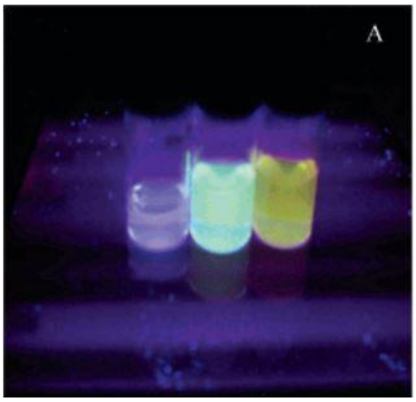

Figure 1.2: Carbon Dots Emitting Fluorescent Light under 365 nm UV Light (Xu et al., 2004).

Over the years, various CDs synthesis methods have been developed which include hydrothermal, microwave-assisted, pyrolysis, laser ablation, electrochemical exfoliation and others. Meanwhile, biomass has been extensively used as the carbon precursor for the fabrication of CDs mainly due to its environmentally friendliness and fairly cheap raw material cost. Table 1.1 summarizes some examples of biomass used as carbon precursors for CDs (Meng et al., 2019).

Table 1.1: Biomass as Carbon Precursors in the Synthesis of CDs (Meng et al., 2019).

Vegetable-Derived CDs	▪ Onion ▪ Garlic ▪ Potato ▪ Cabbage	▪ Yam ▪ Sweet Potato ▪ Carrot ▪ Pipe tobacco
Fruit-Derived CDs	▪ Winter melon ▪ Papaya ▪ Orange juice ▪ Pomegranate ▪ Dragon fruit	▪ Pomelo peel ▪ Banana juice ▪ Lemon juice ▪ Apple
Other Biomass-Derived CDs	▪ Grass ▪ Bee pollens ▪ Fish scale ▪ Rice husk	▪ Black tea ▪ Egg white ▪ Prawn shell

Ever since the discovery of CDs, comprehensive researches have been conducted to study the properties of CDs. Aside from the fluorescent property, CDs are found to possess various advantages including their excellent solubility in water, non-toxicity, inexpensive synthesis, excellent electron transfer and reservoir properties, which make them possible in a wide variety of applications including photocatalysis (Wang and Hu, 2014).

1.3 Photocatalysis Application of Carbon Dots

Photocatalysis is one of the methods used to degrade pharmaceutical pollutants in water. The basic principle of photocatalysis is that the presence of light causes the oxidation of photogenerated holes and the reduction of photogenerated electrons simultaneously, which result in the occurrence of chemical reaction to degrade toxic compounds in water (Leong et al., 2014).

Recent studies introduced CDs into photocatalyst to improve the photocatalytic performance for pollutant removal from water. Owing to the excellent light absorption and up-converted photoluminescence (UCPL) properties, CDs are capable in enhancing the performance of photocatalysts as well as to restrain the recombination of electron-hole pairs of traditional photocatalysts (Cong and Zhao, 2017).

Studies on the fabrication of photocatalytic membrane to achieve efficient photocatalytic activity were conducted by Fischer et al. (2015), Zhang et al. (2016), Athanasekou et al. (2012) and Lin et al. (2012). Photocatalysts were immobilized onto the surface of the existing microfiltration (MF) or ultrafiltration (UF) membranes. It was found that surface located photocatalysts generally performed better than the membranes with photocatalysts entrapped in the membrane matrix. This is because surface located photocatalytic membrane enables all the photocatalysts to be exposed for light irradiation and well-mixed with the targeted molecules so that photocatalysis can take place. On the other hand, the entrapped photocatalysts in membrane matrix are inefficient for photocatalysis to occur since they are not exposed to light irradiation and hidden in the membrane matrix, thus do not contact with the targeted molecules (Fischer et al., 2015).

1.4 Problem Statement

Over the years, the issue of detecting active pharmaceutical constituents in water has gained increasing attention due to the negative impacts they foster even in very low concentration. Due to the modern technology and scarcity of drinkable water sources, the recycling and reuse of water become a norm of practice. This leads to the percentage of pharmaceutical constituents in water to increase by accumulation after multiple times of recycling without efficient pharmaceutical wastewater treatment method. Therefore, proper segregation methods of pharmaceutical wastes from water must be developed to reduce the concentration of pollutants in water (Fischer et al., 2015).

Photocatalysis is found to be one of the effective methods that is capable to oxidize the non-biodegradable pollutants in water. In the previous decade, titanium dioxide (TiO_2) has been widely studied and used as photocatalyst owing to its high photocatalytic performance, chemically and biologically stable, and proven synthesis technique (Ahmadi et al., 2017). However, there are also several drawbacks of this material such as the rapid recombination of electron-hole pairs as well as the narrow band gap of 3.2 eV which limits the absorption band at UV region only (Ahmadi et al., 2017). Besides, the inevitable agglomeration of TiO_2 nanoparticles is also one of the major disadvantages (Ahmadi et al., 2017). In order to overcome these challenges, CDs are introduced to be incorporated to TiO_2 photocatalysts as they are able to restrain the recombination of electron-hole pairs and alter the band gap to visible light absorption region, as well as reducing the agglomeration of TiO_2 nanoparticles (Ahmadi et al., 2017). Furthermore, CDs also possess excellent UCPL property which enhances the photocatalytic activity of TiO_2.

Agriculture industry is one of the promising contributors to the country’s economy. Among the various agriculture products, palm oil is one of the biggest agriculture industries in Malaysia due to the suitable climate and abundance of rain. Large scale plantation and palm oil production lead to major waste disposal issue as only 15% of the entire oil palm tree which are the fresh fruits are able to be processed into final product, while the remaining 85% are considered as biomass wastes (Khalil et al., 2012). By exploiting the abundance oil palm biomass wastes, they are hence used as carbon precursors for the fabrication of CDs in this study.

Generally, semiconductor photocatalysts such as TiO_2 are developed as suspended powder form in photocatalytic reactor. Despite the large specific surface area of powdered photocatalyst which exhibits excellent photocatalytic performance, the nanosized photocatalyst must be removed from the treated water to recover the photocatalyst as well as to prevent the formation of secondary pollutants (Shi et al., 2019). However, the segregation of the nanosized particles from water is difficult and complex. Hence, membrane technology is suggested to overcome this issue by incorporating the nanosized photocatalyst on the membrane surface, where photocatalysis reaction occurs at the membrane and thus separation of powdered photocatalyst from treated water will not be required.

1.5 Aims and Objectives

The aim of this research is to produce photocatalytic membrane incorporated with nitrogen-doped carbon dots/titanium dioxide (N-CDs/TiO_2) photocatalysts for the removal of paracetamol from water under visible light. The objectives of this study include:

(i) To prepare N-CDs nanomaterial using oil palm fronds as the carbon precursor.

(ii) To synthesize and characterize the N-CDs/TiO_2 hybrid photocatalyst with varying loadings of N-CDs solution in terms of crystal structure, functional groups, morphology and surface charges.

(iii) To fabricate photocatalytic membrane by immobilizing hybrid photocatalyst on the membrane surface using chemical grafting method.

(iv) To investigate the performance of photocatalytic membrane in terms of permeability and photocatalytic activity in the removal of paracetamol from aqueous water under visible light.

1.6 Scope of the Study

CDs were prepared by using oil palm fronds as the biomass carbon precursors mainly due to its abundant availability as biomass waste. Ethylenediamine (EDA) was used as the nitrogen source to synthesize nitrogen-doped CDs as it enhanced the photoluminescence (PL) property and promoted the electron transfer capability of CDs. Hybrid N-CDs/TiO_2 photocatalysts were produced using hydrothermal method by manipulating different loadings of N-CDs. Upon the completion of photocatalysts synthesis, the hybrid photocatalyst was immobilized on to the surface of PES membrane via chemical grafting method. Photocatalytic activity of the photocatalyst produced was tested in both suspension form and membrane to remove paracetamol from aqueous water.

Hereafter, a series of characterization techniques were carried out on the synthesized powdered photocatalysts and photocatalytic membrane. The synthesized powdered photocatalysts were tested by XRD to study the crystallographic phase and crystallite size of nanoparticles. Next, FTIR was conducted to study the functional groups attached on the photocatalysts. Zeta potential was also conducted to determine the surface charges of photocatalysts. Last but not least, SEM-EDX analysis was performed to study the morphologies and elemental composition of photocatalysts. In terms of the fabricated photocatalytic membranes, FTIR and SEM analyses were carried out to identify the functional groups and morphologies of membranes respectively.

CHAPTER 2

LITERATURE REVIEW

2.1 Photocatalysis Mechanism

According to Zhu and Wang (2017), the mechanism of photocatalysis can be described in 4 major steps, as illustrated in Figure 2.1.

.

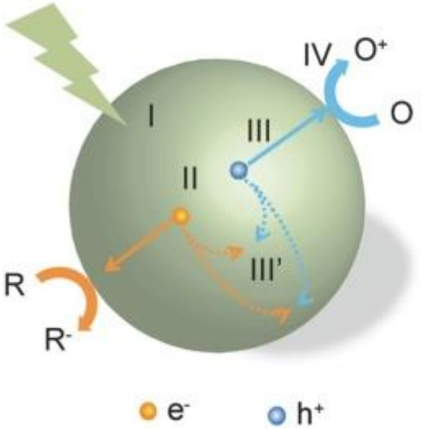

Figure 2.1: Steps Involved in Photocatalytic Reaction (Zhu and Wang, 2017).

As shown in Figure 2.1, the steps of photocatalysis are listed as below:

(I) Absorption of light to form electron-hole pairs.
(II) Segregation of excited charges.
(III) Transfer of electrons and holes to the photocatalysts surfaces.
(IV) Utilization of charges for redox reactions to occur on the surface.

A photocatalyst is a material that is capable to promote photocatalytic reaction by absorbing light, generating electron-hole pairs for reaction to occur while regenerating its chemical composition after each cycle of reaction (Khan, Adil and Al-Mayouf, 2015). The general photocatalysis mechanism was explained by Leong et al. (2014) on titanium-based photocatalyst and the schematic diagram of photocatalysis by TiO_2 is shown in Figure 2.2.

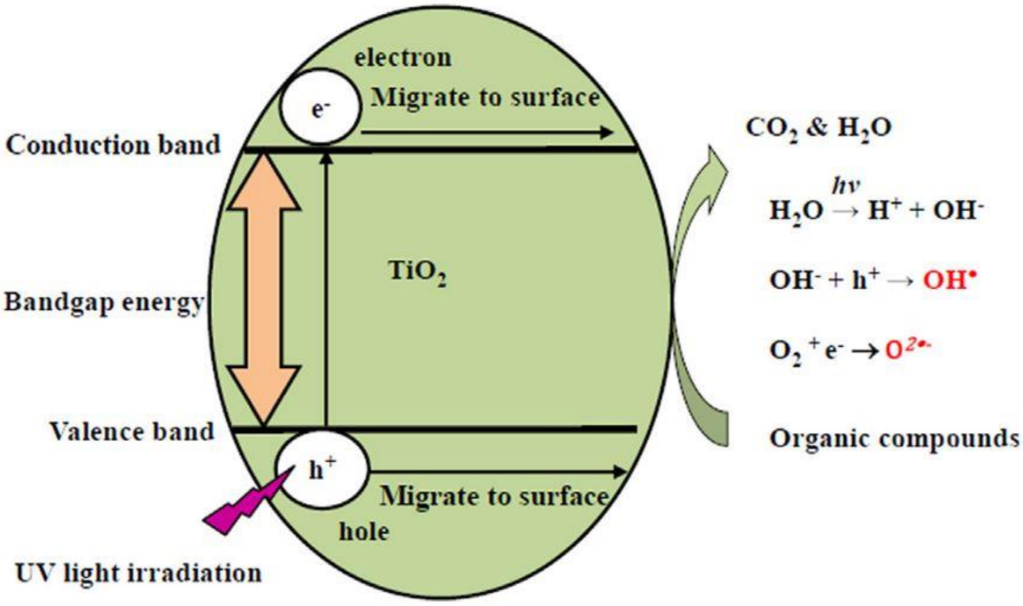

Figure 2.2: Schematic Diagram of Photocatalysis by TiO_2 (Leong et al., 2014).

When TiO_2 photocatalyst is exposed to UV light irradiation, the energy of UV ray is higher than the band gap energy of photocatalyst, thus exciting electrons (e^-) from the valence band to the conduction band. This leaves a positively charged hole (h^+) at the valance band. Both negative electrons and positive holes then move to the surface of photocatalyst, where a series of redox reactions will then be initiated. Firstly, Ti^{4+} are reduced to Ti^{3+} with the presence of electrons, and further react with oxygen molecules (O_2) that are absorbed on the surface of TiO_2 to form superoxide radicals ($O_2^{\cdot-}$). Simultaneously, water molecules (H_2O) that are absorbed on TiO_2 surface react with the positively charged holes to form hydroxyl radicals ($OH^{\cdot}$). These oxygen reactive radicals have strong oxidizing ability and thus able to oxidize organic pollutants (R) into harmless carbon dioxide and water. The steps of photocatalysis are simplified into the following expressions.

$$Ti^{4+} + e^- \rightarrow Ti^{3+}$$

$$Ti^{3+} + O_2 \rightarrow Ti^{4+} + O_2^{\cdot-}$$

$$H_2O + h^+ \rightarrow OH^{\cdot} + H^+$$

$$OH^{\cdot} + R \rightarrow intermediates \rightarrow H_2O + CO_2$$

$$O_2^{\cdot-} + R \rightarrow intermediates \rightarrow H_2O + CO_2$$

To define a good photocatalyst, the material should include several important features such as the desired electron band gap, suitable morphology, particle size distribution, high surface area, high stability and reusability (Khan, Adil and Al-Mayouf, 2015). Among the properties of photocatalyst, electron band gap of photocatalyst plays the most important role (Argurio et al., 2018). In terms of electron band gap, Sharma et al. (2019) stated that photocatalyst with wide band gap ($E_g \geq 3$ eV) can only absorb UV light due to the higher energy demand for electron excitation, while photocatalyst with narrow band gap ($E_g \leq 3$ eV) is capable of absorbing visible light as the additional energy is not needed for electron excitation. Typically, visible light absorption is favourable as non-natural UV sources are costly and require higher protection for their usage in water purification (Sharma et al., 2019).

2.2 Carbon Dots

2.2.1 Structure of Carbon Dots

CDs emerged as a new member in the nanocarbon family and showed various unique advantages compared to the other well-developed nanocarbons. Extensive studies and researches have been carried out to investigate the properties of CDs in order to utilize them in multiple applications.

CDs are quasi-spherical nanoparticles having particle diameter lesser than 10 nm. They can either be in amorphous or crystalline structure depending on their carbon clusters. Main differences between amorphous and crystalline CDs are summarized in Table 2.1. The amorphous configuration of CDs is caused by the relatively higher amounts of oxygen or nitrogen containing moieties that distort the systematic carbonic framework through covalent bonds (Wang et al., 2015).

Besides, CDs possess good aqueous solubility due to the various functional groups such as carbonyl and hydroxyl groups that are attached on the surface of CDs, which further influence the electronic structure of CDs (Cong and Zhao, 2017). The highest occupied molecular orbital (HOMO) and lowest unoccupied molecular orbital (LUMO) levels of CDs can be modulated simultaneously by certain functional groups. These functional groups include the electron donating and electron withdrawing groups which cause small changes in the CDs band gap. The electron donating groups will increase

HOMO and LUMO levels to higher energy, while electron withdrawing groups will cause a drop of total energy levels (Cong and Zhao, 2017).

Table 2.1: Comparison between Amorphous and Crystalline CDs.

	Amorphous	**Crystalline**
Structure	Spherical	Disk
Particle Diameter	<10 nm	<20 nm
Hybridization of Carbon Atom	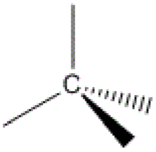 *sp*^{3}	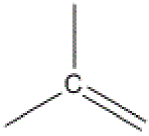 *sp*^{2}

2.2.2 Properties of Carbon Dots

Characterization of CDs is important for better understanding of the unique properties of the nanomaterials in order to attain their benefits for a wide range of applications. Being the newly discovered member to the nanocarbon family, CDs possess various unique advantages over the other well-developed nanocarbons such as graphene, carbon nanotube and organic fluorophores.

One of the most unique properties of CDs is their strong optical absorption attributed to the π-π^* transition of C=C bonds (Jelinek, 2017). The absorption of CDs is the strongest in the UV region with the wavelength of 260 - 320 nm, and a tail extending to the visible range, as shown in Figure 2.3.

The optical absorption of CDs provides PL property to the nanoparticles, which makes CDs versatile and possible for various applications. As illustrated in Figure 2.3 and Figure 2.4, the emitting colour of CDs can be readily tuned according to variation in excitation wavelength. This remarkable feature has attracted much interest from various fields to study the underlying properties that contribute to their PL properties.

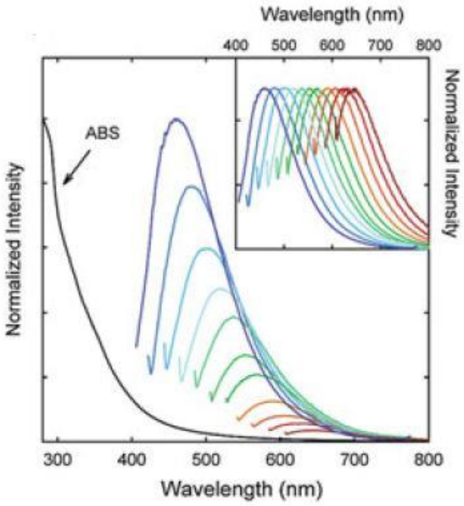

Figure 2.3: Absorbance and Photoluminescence Emission Spectrums at Exciting Wavelengths of 20 nm Increments from 400 nm. Inset Shows the Emission Spectrums of CDs at Normalised Intensity (Sun et al., 2006).

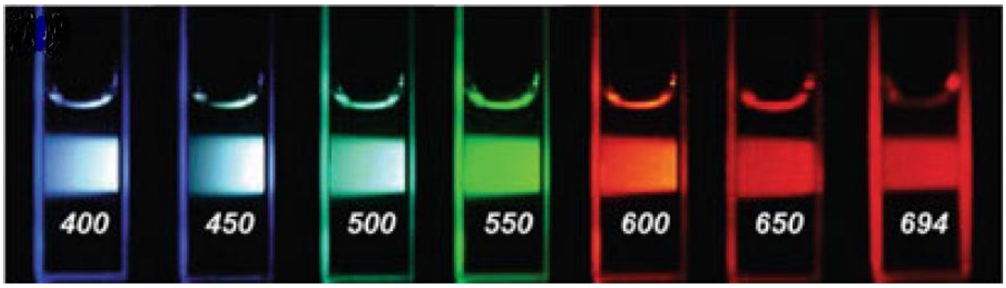

Figure 2.4: Polyethylene Glycol Passivated CDs Excited at Indicated Wavelengths (Sun et al., 2006).

Li et al. (2010) suggested that the emitting colour of CDs strongly depends on the differences in particle size; where small CDs emit UV light, medium-sized CDs emit visible light and large CDs emit near-infrared light. To confirm this theory, theoretical calculations were further performed to study the relationship between the PL property of CDs and their crystallite sizes. The results from the study are illustrated in Figure 2.5 and can be interpreted as the decrease in CDs sizes will increase the band gap between HOMO and LUMO, which further increases the strength of emission. This result agrees to the quantum confinement effect (QCE), where a reduction in CDs band gap is expected when particle size increases (Cong and Zhao, 2017).

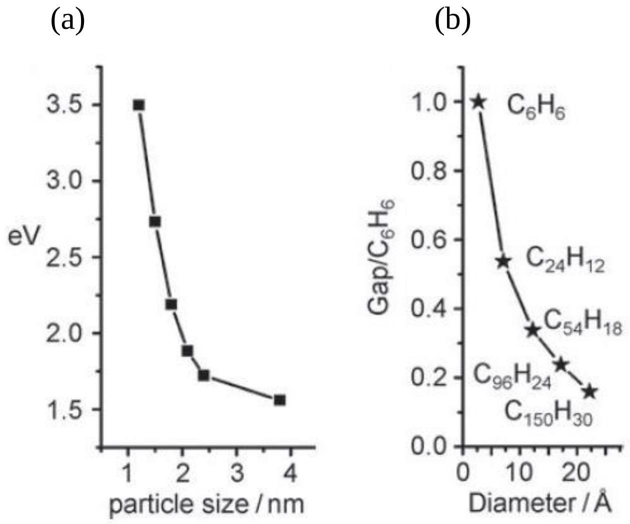

Figure 2.5: (a) Relationship between Sizes of CDs and Their Respective PL Properties and (b) HOMO-LUMO Gap Dependence on the Carbon Dots Sizes (Li et al., 2010).

Furthermore, another popular optical property of CDs is the UCPL property, which could be resulted from the multi-photon activation process. UCPL is the anti-Stokes emission whereby light with shorter wavelength is emitted by a longer excitation wavelength (Wang and Hu, 2014). This property is especially advantageous in cell imaging with two-photon luminescence microscopy and photocatalysis in the visible to near-infrared region (Wang and Hu, 2014). However, according to Cong and Zhao (2017), it is still debatable whether UCPL property is truly caused by the simultaneous absorption of multiple photons with longer wavelength. This is because in the recent study on UCPL property of CDs by Wen et al. (2014), it was found that the so-called UCPL is in fact emerged from the normal fluorescence excited by the leaking component from fluorescence spectrophotometer. Therefore, it is crucial to eliminate the normal fluorescence during the observation of UCPL in CDs by exciting the CDs under high power density via a femtosecond pulsed laser, as suggested by Cong and Zhao (2017).

Beside the major property of CDs which is the superior optical property, CDs possess multiple beneficial properties that further put CDs as the leading nanomaterial for various applications. A summary of CDs' properties are tabulated in Table 2.2.

Table 2.2: Summary of the Superior Properties of CDs (Singh et al., 2018).

Advantages	Description
Inexpensive	Various synthesizing methods can be used to produce CDs from abundant and inexpensive source of raw materials.
PL	Tunable PL property.
UCPL	CDs have a sharply defined emission peak from longer excitation wavelength.
Electronic Properties	Electrochemical luminescence and chemiluminescence properties derived from the unique electronic properties of CDs as electron donors and receivers.
Biological Properties	Extraordinary biological properties include the highly hydrophilic, non-toxicity and good biocompatibility guarantee their applications in bioimaging, biosensors and drug delivery.
Chemically Inert	High chemical stability of CDs.

2.2.3 Applications of Carbon Dots

Since the discovery of CDs in 2004, extensive studies and researches on CDs have been carried out to investigate its fascinating properties for the use of various applications. In recent years, the applications of CDs in various fields have been increased extensively and became an important element especially in the modern society.

One of the common applications of CDs is the biomedical field. CDs are popular for bioimaging via in-vitro and in-vivo methods due to their fluorescent property with low biotoxicity and good biocompatibility (Wang and Hu, 2014). Having high water solubility, flexibility in surface modification, high photostability and good cell permeability, CDs also act as biosensor for visual monitoring of cellular copper, glucose, potassium, iron, phosphate and nucleic acid in the body (Wang and Hu, 2014).

Next, the discovery of CDs hugely contributed to the development and improvement in optronics. One of the applications in optronics is the use of CDs as sensitizers to capture sunlight in dye-sensitized solar cells (DSC), to overcome the issues encountered in the traditional DSC which include the high cost for photobleaching of organic dyes as well as the toxicity of ruthenium (Wang and Hu, 2014). Besides, owing to its phenomenal electrochemical performance, CDs see a huge potential in supercapacitor industry as CD-based hybrids and CD-based ionic liquid. As reported by Wang and Hu (2014), CDs are also emerging as LED materials due to their eco-friendliness and stability in light emission.

Along with the ability to generate charge carriers such as electrons and holes, as well as the excellent light absorption and UCPL properties, CDs have great potentials in photocatalysis including energy conversion and environmental remediation (Cong and Zhao, 2017). In the aspect of energy conversion and renewable energy, CDs typically modified into CDs/TiO_2 composites while the CDs act as a photosensitizer as well as an electron reservoir to efficiently split the photoinduced electron-hole pair of TiO_2 (Wang and Hu, 2014). Meanwhile, in the environmental aspect, CDs composite photocatalysts have been utilized in pollutant degradation especially in water treatment industry.

Furthermore, CDs can be utilised as chemical sensors to detect the presence and amount of substances by monitoring the differences between the fluorescence intensity of CDs as different substances will react differently with the surface functional groups of CDs. Several substances that can be identified through this method are iron(III) (Fe^{3+}), glucose, nitrites, hydrogen sulphide (H_2S), thrombin, biothiol, silver (Ag^+), mercury (Hg^{2+}) and copper(II) (Cu^{2+}) (Wang and Hu, 2014).

Recently, the application of CDs has further extended into membrane technologies in separation processes. The development of CDs in membrane sector is mainly due to two distinctive advantages of CDs which are the inexpensive production as well as their superior physiochemical properties, which include the chemical inertness, super-small sizes, tunable hydrophilicity, good biocompatibility, various surface functional groups and antifouling property (Zhao and Chung, 2018). On top of these advantages, the utilizations of CDs in various membrane designs such as reverse osmosis, forward osmosis, nanofiltration, ultrafiltration, membrane distillation, organic solvent nanofiltration and other processes are still being explored and improved to bring their benefits into this field (Zhao and Chung, 2018).

2.3 Preparation of Carbon Dots

In the past 10 years, numerous methods on synthesizing CDs have been reported, which mainly classified into two categories of top-down and bottom-up approaches. As an overview, top-down method is the breaking down of large carbonaceous materials while bottom-up method is the carbonization of smaller precursors followed by chemical fusion to form CDs (Cong and Zhao, 2017). Despite the differences in preparation methods, both top-down and bottom-up approaches face three major issues which are (i) carbonaceous aggregation during carbonization, (ii) particle size control and uniformity, as well as (iii) surface properties that are vital for solubility (Wang and Hu, 2014). Post-synthetic treatments and other perfect synthetic routes are adopted to overcome these barriers. The synthesis of CDs via top-down and bottom-up methods are shown in Table 2.3.

Table 2.3: CDs Preparation via Top-down and Bottom-up Methods (Cong and Zhao, 2017).

Top-down	**Bottom-up**
▪ Arc Discharge	▪ Microwave Assisted Pyrolysis
▪ Laser Ablation	▪ Hydrothermal Treatment
▪ Electrochemical Exfoliation	▪ Oxidative Acid Treatment

2.3.1 Top-down Route

As mentioned, top-down route is the fragmentation of larger carbon precursors such as carbon nanotubes, carbon fibres, graphite powders, carbon black, and tire soot into CDs. Although these carbonic precursors have abundant crystalline sp^2 carbon structures, they have ineffective band gap for luminesce excitation and thus, the breaking down of large carbon matters into nano-scale particles is an important step to provide the CDs with PL property (Wang et al., 2015).

The first CD was fabricated through accident using top-down oxidizing arc discharge soot with nitric acid, HNO_3, along with the extraction of sediment by using sodium hydroxide, NaOH solution around pH 8.4, resulting in a dark suspension. Gel electrophoresis separation was then carried out to purify the black suspension where a highly fluorescent CD with the size of approximately 18 nm was found (Singh et al., 2018). These nano-sized CDs showed PL properties by emitting green-blue, yellow and orange fluorescent light when excited by 366 nm UV irradiation. However, the PL quantum yield achieved by this method was only 1.6%, too less for any practical application (Wang et al., 2015).

Next, fabrication of CDs can be accomplished by laser ablation method which was first conducted by Sun et al. in 2006. The process was carried out by laser ablation of the sample in the presence of water vapour with argon gas at high operating conditions of 75 kPa and 900 °C. The sample produced at this stage possessed no PL property as it was dominated with nano-scale carbon particles with wide range of sizes. 2.6 M nitric acid was then used to treat the sample and refluxed for 12 hours, followed by surface passivation of attaching simple organic species to the treated sample. Through these steps, CDs with adjustable luminescence emission was produced (Sun et al., 2006).

A simple laser ablation method was demonstrated by ablating a suspension of carbon material in organic solvents such as diamine hydrate, diethanolamine and polyethylene glycol (PEG_{1500N}). The synthesized CDs were found to be 1 - 8 nm with green/blue fluorescence (Wang et al., 2015). Besides, another simpler laser ablation was carried out by Li et al. (2010) by using nano-carbon materials with the size of <50 nm as the starting material, as well as solvent and water as the liquid medium to synthesize CDs. Wang and Hu (2014) stated that the origin of luminescence property of CDs depends on the ligands that were attached on the surface of CDs. Hence, it is able to achieve tunable light emission property by modifying the surface states of CDs through the use of different organic solvents. The pros of laser ablation are its effortlessness and environmentally friendly approach. However, this method requires large amount of carbon matter for carbon targets development as well as highly skilled personal to perform the synthesis and post-synthetic procedures (Singh et al., 2018).

Furthermore, another recognised top-down method is the electrochemical exfoliation method. This method is an effective and scalable approach to synthesize CDs by applying direct current to bulk carbon precursors without using strong acid and further purification. Two platinum sheets were used as auxiliary electrodes, submerged into ionic fluid/water solution. Due to the differences in static potentials and the exchange of anionic intercalation between the ionic fluid and water, carbon matter was exfoliated. CDs fabricated by this method range from 1 to 10 nm with possible PL quantum yield up to 14%, where the sizes of the CDs increase with the increasing potential difference (Wang et al., 2015).

2.3.2 Bottom-up Route

The more commonly used CDs synthesizing method is the bottom-up route which synthesizes CDs from small precursors such as carbohydrates, citrate, and other natural or synthetic polymers (Chu et al., 2019). Bottom-up methods are more preferable compared to top-down methods due to their simple, environmentally friendly and cost effective characteristics with wide variety of available precursors. In addition, the optical properties of CDs synthesized from these methods can be easily tuned by manipulating the reaction conditions (Chu et al., 2019).

One common bottom-up method is the microwave assisted method, which is the breaking of chemical bonds and carbonizing the precursors by using electromagnetic radiation of microwave energy (Chu et al., 2019). Various experiments and studies were carried out in the past by using varying microwave power and microwave exposure duration of different precursors to obtain CDs with different particle sizes and PL properties. For instance, green luminescent CDs with PL quantum yield of 2.4% were obtained by single-step microwave irradiating sucrose (carbon precursor) and diethylene glycol (reaction medium) for 1 minute (Liu et al., 2014). Huo et al. (2017) fabricated pale yellowish CDs using microwave radiation on citric acid and ethylenediamine at 800 W for 10 minutes. The CDs obtained were then modified into cadmium selenide photocatalyst (CDs/CdSe) which showed enhanced degradation property for the degradation of tetracycline hydrochloride (antibiotic pollutant). Overall, microwave assisted method is known for its rapid and short reaction time, relatively simple synthesizing method and cost effectiveness. Regardless, the down side of this method is the difficulty in finely controlling the synthesizing process which may lead to poor quality CDs with irregular sizes and shapes (Chu et al., 2019).

Hydrothermal synthesis process is the most commonly used and facile CDs synthetic method. Typically, solutions of organic precursors are sealed in an autoclave with the present of water or organic solvent while reacting under high temperature and pressure to be converted into carbon structure. Particle sizes of CDs synthesized by this method strongly depends on the reaction temperature, where higher reaction temperature yields the smaller particle sizes, which directly increase the PL quantum yield (Liu et al., 2012). CDs synthesized by Liu et al. (2012) via hydrothermal approach from grass precursors have been used as chemical sensors to detect Cu^{2+} ions in lake water. Moreover, the similar team of researchers also fabricated CDs from pomelo peel, sizing 2 - 4 nm with PL quantum yield of 6.9%, were utilized for Hg^{2+} detection. Various other environmental friendly precursors such as glucose, sugarcane juice, orange juice, banana juice, chitosan and others were used to synthesize CDs via hydrothermal method (Jhonsi, 2018). In fact, hydrothermal synthesis method is the most attractive and commonly used method owing to the low costing, eco-friendly green precursors, simple one-step preparation, non-toxic materials and low energy consumption. The only limitation of hydrothermal approach is the poor control over the particle sizes (Chu et al., 2019).

Next, Jhonsi (2018) stated that oxidative acid treatment is another bottom-up method which involves the reflux of carbon waste soot in acidic medium accompanied by further centrifugation, neutralization and purification to obtain the fluorescent CDs. Waste soot used in this method came from the combustion of natural gas or other fuel materials. There were two alternative methodologies of oxidative acid treatment to obtain CDs. The first method used was the mixing of several grams of waste soot with 5 M nitric acid, refluxed for 12 hours and set to cool down to obtain fluorescent CDs. Alternatively, the mixture of waste soot and nitric acid was neutralised by adding sodium carbonate (Na_2CO_3), where CDs were obtained after extensively dialyzing the mixture against double distilled water via a dialysis membrane (Jhonsi, 2018). Oxidative acid treatment has various benefits which include its effectiveness in introducing functional groups to the CDs, good water solubility, absence of post-synthetic aggregation, as well as the prepared CDs can be used directly for imaging applications without surface passivation. On the other hand, the down side of this method is its poor storage stability due to the defects on the surface of CDs (Jhonsi, 2018).

Table 2.4 summarizes the advantages and disadvantages of the top-down and bottom-up methods.

Table 2.4: Advantages and Disadvantages of Various CDs Fabrication Methods (Wang and Hu, 2014; Jhonsi, 2018; Chu et al., 2019).

	Method	Advantages	Disadvantages
Top-down Route	Arc Discharge	▪ Widely accessible ▪ Abundant sources	▪ Drastic processes with harsh conditions ▪ More than one step ▪ Low quantum yield ▪ Poor size control
	Laser Ablation	▪ Rapid and effortless ▪ Effective and tunable surface states	▪ Low quantum yield ▪ Poor size control
	Electrochemical Exfoliation	▪ Controllable nanostructure and size ▪ Stable ▪ One-step process	▪ Limited carbon precursors

Table 2.4 (Continue)

	Method	Advantages	Disadvantages
Bottom-up Route	Microwave Assisted Method	▪ Simple and rapid reaction ▪ Inexpensive and eco-friendly	▪ Poor size control
	Hydrothermal Treatment	▪ Low cost ▪ Low energy consumption ▪ Eco-friendly precursors ▪ Simple one-step preparation	▪ Poor size control
	Oxidative Acid Treatment	▪ Able to introduce various functional groups ▪ Good solubility in water ▪ No formation of post-synthetic aggregation	▪ Poor storage stability

2.4 Biomass as Carbon Precursor

The development of CDs has prompted the utilization of a more environmentally friendly method to fabricate CDs in large scale for its wide potential in various applications. Biomass waste is a suitable candidate to be used as the carbon precursor due to its low raw material cost, renewable and green resources, which also promotes sustainable development at the same time (Meng et al., 2019). Biomass refers to various organisms including animals, plants and microorganisms, which mainly made-up of carbon atoms, and hence is suitable to be used as carbon precursors.

Ever since the discovery of CDs in 2004, various biomass materials have been used as carbon precursor for CDs, such as fruit-derived CDs, vegetable-derived CDs and other sources. Table 2.5 summarizes some of the CDs derived from biomass resources.

Table 2.5: CDs Prepared from Various Biomass Sources and Their Properties.

Biomass	**Synthesizing Method**	**Size (nm)**	**Quantum Yield (%)**	**References**
Orange juice	Hydrothermal	1.5 - 4.5	26	(Sahu et al., 2012)
Lemon juice	Hydrothermal	4.6	28	(Oza et al., 2015)
Lemon peel	Hydrothermal	1 - 3	14	(Tyagi et al., 2016)
Papaya	Hydrothermal	3.4	18.98	(Wang et al., 2016)
Coconut water	Microwave-assisted	1 - 6	54	(Purbia and Paria, 2016)
Oatmeal	Hydrothermal	20 - 40	37.4	(Yu et al., 2015)
Prawn shell	Hydrothermal	6	54	(Gedda et al., 2016)
Peanut shell	Pyrolysis	0.4 - 2.4	9.91	(Xue et al., 2016)
Grass	Pyrolysis	2 - 5	30	(Krysmann, Kelarakis and Giannelis, 2012)
Black tea	Hydrothermal	4.6	-	(Song et al., 2017)

2.4.1 Oil Palm Biomass as Carbon Precursor

Malaysia is blessed with tropical and humid climate which is optimum for the growth of oil palm throughout the year. As one of the biggest agricultural product from Malaysia, oil palm industry has boosted the economy of the country. However, the large scale production of oil palm also created the major waste disposal problem (Abdullah and Sulaiman, 2013). According to Khalil et al. (2012), the useful fresh fruit only accounts for 15% of the entire oil palm tree, while the rest of the plant is considered as oil palm wastes where approximately 70 million tonnes/year of oil palm biomass wastes had been produced in Malaysia alone. The three major oil palm biomass wastes include oil palm frond (OPF) which accounts for 70% of the oil palm tree, empty fruit bunch (EFB) taking up about 10% of the plant and oil palm trunk (OPT) which accounts for only 5% of the plant, as illustrated in Figure 2.6.

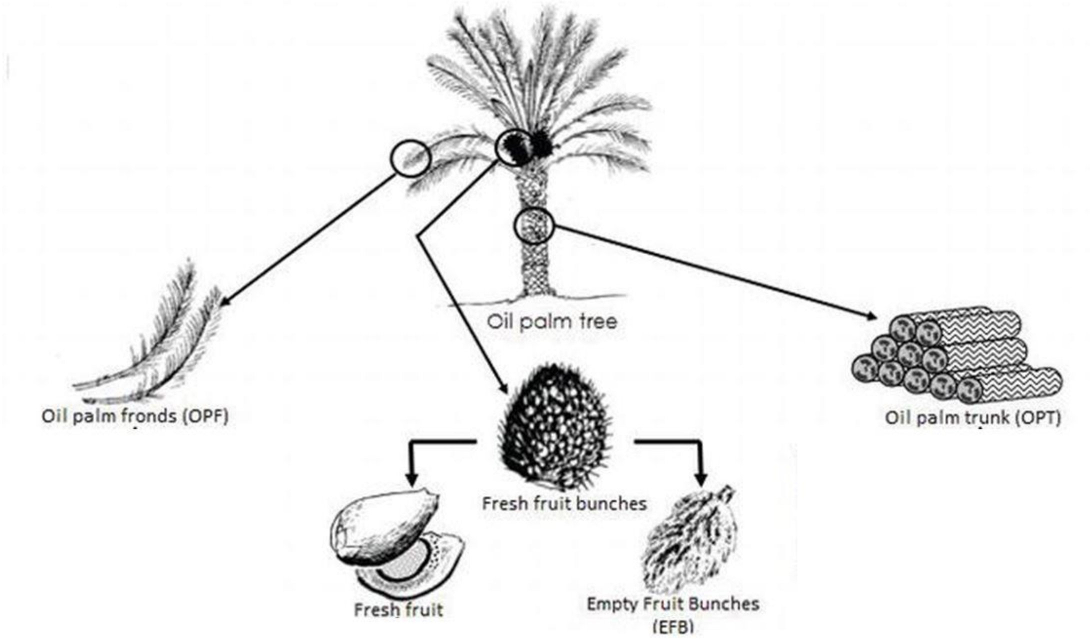

Figure 2.6: Oil Palm Biomass (Dungani et al., 2018).

First of all, the most widely-known oil palm waste is EFB which is the leftovers after fresh oil palm fruits are harvested from oil palm processing. In Malaysia, about 12.4 million tonnes/year of EFB are disposed from oil palm refineries (Khalil et al., 2012). Even though oil palm EFB contains high cellulose fibres and highly potential to be natural fibre resources, the applications of EFB are still very limited and often thrown away as unwanted products.

Next, being the most abundant oil palm biomass wastes, the annual disposal of OPF in Malaysia is about 24 million tonnes/year (Khalil et al., 2012). OPF can be easily obtained daily as the OPF typically falls off from the oil palm trunk by its own or during the harvesting of palm fruits bunches. OPF has high contents of lignocellulose as well as carbohydrates which has a potential to be used a livestock feed. OPFs are usually left rotting under oil palm trees as they are beneficial for nutrient recycling as well as soil conservation and erosion control (Khalil et al., 2012).

Last but not least, abundant OPTs from old oil palm trees are discarded every 25 to 30 years for replantation purpose. Approximately 3 million tonnes/year of OPTs are discarded in Malaysia (Khalil et al., 2012). Differ from EFB and OPF, OPT consists of mainly vascular bundles and parenchayma which generally has no economic value. However, studies have been conducted to make use of OPT in the production of polymer composites, hybrid plywood, paper, furniture and others.

Among these oil palm biomass wastes, OPF is chosen as the carbon precursor over EFB and OPT for the synthesizing of CDs. One of the reasons being its high lignin content up to 25 wt% of biomass as reported by Kavitha and Kumar (2018). High lignin content tends to produce higher quality carbon material and thus OPF is favourable in the synthesizing of CDs. Besides, OPF constitutes for about 70% of the entire oil palm plant which is easily available as an environmental friendly biomass source. Taking the advantage of huge availability of OPF in Malaysia and its high lignin content, OPF is thus a promising carbon precursor for the synthesizing of CDs.

2.4.2 Synthesis of CDs from Oil Palm Biomass

According to Abdullah et al. (2019), nitrogen-doped CDs was fabricated by using EFB derived carboxymethylcellulose (CMC) and ethylenediamine (EDA) via one-pot hydrothermal carbonization method. Nitrogen doping has been proven to enhance the fluorescence efficiency by disordering the hexagonal ring structure of CDs, thus introducing emissive trap states within the crystalline sp^2 core (Abdullah et al., 2019). This statement is further supported by Zhang et al. (2018) who stated that nitrogen doping efficiently induces delocalization of charges, reduces the work function as well as efficiently promotes the capability of electron transfer for CDs. Abdullah et al.

(2019) also revealed that the main factors that affect the quantum yield of CDs produced are the reaction temperature, time and EDA weight.

The preparation of CDs from CMC was carried out by first grinding the CMC into small pieces. A mixture containing 0.3 g fine CMC dispersed in deionized water and 23.3 wt% of EDA was sonicated, placed into a 50 mL autoclave, sealed and heated for 6 hours at 270 ºC in an oven. After cooling down naturally to room temperature, CDs were separated from the dark brown dispersion by centrifugation for 10 minutes and filtered with a membrane with pore size of 0.22 μm (Abdullah et al., 2019).

CDs fabricated from EFB derived CMC exhibited as dark brown solution under daylight and emitted blue fluorescence under UV irradiation of 365 nm. A maximum luminescence was found at 426 nm under the maximum excitation of 320 nm. Furthermore, the full-width-half-maximum (FWHM) of XRD result was found to be 96 nm, indicating the CDs produced are suitable for a broad range of applications (Abdullah et al., 2019).

Another recent study was conducted by Jamaludin, Andul and Tan (2018), to synthesize CDs from EFB biochar, which is the carbon-rich remnants from the incomplete combustion of biomass or the process of pyrolysis, via hydrothermal method. Biochar from EFB can be synthesized by two methods, either by using the conventional heating furnace or microwave-assisted method (Mubarak et al., 2016). The raw EFB sample was first washed for a few times by using tap water and finally with distilled water. Next, the EFB sample was dried in the oven at 105 ºC for 1 day to remove the moisture in the sample until a constant weight was obtained. Then, depending on the synthesizing methods, the dried EFB sample was ready to be processed into biochar.

To produced EFB biochar via microwave-assisted method, uniform particle sizes of <150 μm were achieved by crushing and sieving the dried EFB sample. Next, 20 g of sieved EFB sample was put into a quartz tube with the length of 500 mm, outer diameter of 35 mm, inner diameter of 38 mm. It was then underwent pyrolysis in a microwave muffle system oven. The process parameters including the reaction temperature, duration and power of microwave were optimized to obtain biochar with high surface area as well as high product yield. After the reaction was completed, the sample was cooled to room temperature and further washed with water to neutralize the pH level (Mubarak et al., 2016).

Similarly, the conventional heating furnace method used 20 g of the dried EFB with the particle size <150 μm was placed into a quartz tube with the length of 1000 mm, outer diameter of 75 mm, inner diameter of 70 mm. This tube was then inserted into a high temperature horizontal furnace where both ends were sealed by metal enclosures. Once again, the process parameters including the carbonization temperature and reaction duration were optimized. Then, the sample was cooled to room temperature and washed with distilled water to neutralise the pH level (Mubarak et al., 2016).

According to Jamaludin, Andul and Tan (2018), a mixture of 0.06 g EFB biochar and 6 mL of isopropanol (IPA) was added into a steel tube reactor and sonicated for 5 minutes. Next, it was transferred into an oven with a temperature of 250 ºC for 1 hour. It was then cooled down in a water bath for 4 hours and the final CDs solution was obtained by centrifugation to remove unreacted biochar (Jamaludin, Andul and Tan, 2018).

The result showed that the CDs fabricated from EFB biochar existed in light brown solution under daylight and emitted a blue luminescence under UV irradiation. The maximum emission peak of 430 nm was achieved with an excitation wavelength of 300 nm. Owing to the excellent luminescence property, the synthesized CDs possess a promising potential in optical and electrical applications (Jamaludin, Andul and Tan, 2018).

2.5 Carbon Dots Nanocomposite

Throughout the years, various materials were explored to be utilized as photocatalysts. Metal oxides and semiconductors are very popular for this purpose, owing to their material characteristics such as light absorption and excitation of electrons from valence band to conduction band for the formation of electron-hole pair (*e-*/*h+*) (Khan, Adil and Al-Mayouf, 2015). For metal oxides, the photocatalytic activity generally comes from two sources, the formation of $^{\cdot}OH$ radicals by oxidation of OH^- anions and the formation of O_2^- radicals by reduction of O_2. These photogenerated electron-hole pairs are capable to either oxidize or reduce the toxic compounds that attached to the photocatalyst surface, hence detoxifying the toxic compounds into harmless by-products (Khan, Adil and Al-Mayouf, 2015).

Unfortunately, these photocatalysts face challenges in providing a high efficiency photocatalysis to degrade toxic chemicals in pharmaceutical wastewater treatment mainly due to the rapid photogenerated electron-hole recombination as well as the poor efficiency in harvesting visible light. Zhu and Wang (2017) stated that the recombination of electron-hole pairs releases the harvested energy in the form of heat or light emission to the surrounding instead of degrading the toxic components, which then lowers down the efficiency of photocatalysis.

To overcome these problems, CDs are introduced to bind with the available photocatalysts to improve the overall efficiency of photocatalysis. This is because all the optical and structural properties of CDs meet the requirement of photocatalysis, which include the utilization of solar spectrum, rapid migration of charge carriers and efficient redox reaction on the photocatalyst surface (Cong and Zhao, 2017). Furthermore, ever since the discovery of the tunable optical property of CDs, as well as the PL and UCPL properties, CDs become widely utilized for photocatalysis as they are able to promote electron-hole separation and broaden light response (Cong and Zhao, 2017).

According to Chu et al. (2019), there are two methods to synthesize CDs incorporated photocatalyst, which are the in-situ or ex-situ approach. In-situ approach is the mixing of all CDs precursors and photocatalyst together to be treated further. A more commonly used method is the ex-situ approach, where the separately-prepared CDs and photocatalyst are incubated and mixed together (Chu et al., 2019).

Throughout the years, several photocatalysts have been used to combine with CDs to degrade toxic compounds in water. The CDs precursors, synthesizing methods, and the result of photocatalysis including the structure of nanocomposites and their photocatalytic efficiency are studied.

2.5.1 Lead/Carbon Dots in Titanium Dioxide (Pb-CDs-TiO_2)

Owing to the good oxidizing ability, environmentally friendly characteristic, as well as the high thermal and chemical stability, TiO_2 has been one of the most promising and widely used photocatalysts (Chu et al., 2019). Mehta et al. (2018) studied the sensing of toxic metals by CDs as well as detoxifiying dyes by photocatalysis method with a kill waste by waste concept. The nanocomposites of Pb-CDs-TiO_2 were used to degrade industrial dyes including remazol black XP (CNB), coralline red BS (CRB) and reactive brilliant red X-3BS (RBX). TiO_2 has been proven to possess excellent record for photocatalytic dye degradation and hence is popular in photocatalysis. However, the single down side of TiO_2 is its band gap (3.2 eV) which only actives in UV region. Hence, wet impregnation method was used by immersing Pb-CDs solution in TiO_2 to synthesize Pb-CDs-TiO_2 nanocomposite to change the energy band gap to 2.8 eV, causing the composite to active under visible light irradiation.

In the research conducted by Mehta et al. (2018), carbon precursor used was ascorbic acid which can be found in most citrus fruits such as orange, lemon, grapefruit, as well as vegetables like broccoli and cauliflower. The ascorbic acid used in this study was analytical grade chemical obtained from Loba Chemie Ltd. The synthesis of Pb-CDs-TiO_2 was first dissolving 0.5 g of kollicoat and ascorbic acid at 1:1 w/w% in water under continuous stirring. 20 minutes later, 5 mL of the sample was pipetted out and transferred into a glass reaction vessel which was further heated in the microwave synthesizer. The reaction temperature was set at 130 ºC with the reaction duration of 30 minutes at 300 W powers. The formation of CDs was confirmed by the formation of yellow colour in the solution. Next, a suspension of 0.5 g TiO_2 in 20 mL of water was stirred continuously at room temperature, where 1 mL of Pb-CDs (1:1 v/v) solution was added dropwise into the suspension. In order to guarantee a homogeneous solution, the stirring was continued for 8-10 hours. Lastly, after washing and drying, the as-synthesized solid photocatalyst Pb-CDs-TiO_2 was obtained.

Under XRD analysis, Pb-CDs-TiO_2 showed its amorphous structure with an average crystallite size of 5-6 nm calculated by using Scherrer equation. Transmission electron microscopy (TEM) showed the spherical morphology of as-synthesized CDs having an average diameter of 7 nm. Furthermore, the Brunner-Emmet-Teller (BET) test based on N_2 adsorption and desorption curves showed that all adsorption-desorption isotherms are type-IV, indicating the mesoporous nature of nanocomposites.

The photocatalytic activity of Pb-CDs-TiO_2 was monitored by performing control experiments revealing that the most toxic industrial dyes including CNB, CRB and RBX were unable to degrade in dark or through photolysis. This proves that in order to allow photodegradation of dyes to occur, the shared effect of both light and photocatalyst are important. Result showed that the degradation efficiency of Pb-CDs-TiO_2 for CRB, CCN and RBX dye was 85%, 99% and 100% respectively, having a higher activity than bare TiO_2 and CDs-TiO_2 due to perfect band alignment after the formation of composite as well as the formation of high oxidative radicals. Similarly, Pb-CDs-TiO_2 tested to degrade dyes in real water sample in Patiala, India also showed excellent result where the efficiency reached 99% as well.

2.5.2 Carbon Dots with N-doped Zinc Oxide (CDs/N-doped-ZnO)

Aside from TiO_2 that have been widely utilized as photocatalyst, zinc oxide (ZnO) is another popular metal oxide in photocatalysis owing to its high catalytic activity, wide band gap (~3.37 eV), relatively lower cost as well as its environmental friendliness compared to other photocatalysts (Muthulingam et al., 2016). However, ZnO faces challenges which include the quick recombination of photo-generated electron hole pairs as well as the narrow absorption band at limited UV region which restrict the photocatalytic efficiency of ZnO. In order to resolve the challenges, ZnO can be incorporated with CDs and nitrogen doping to alter the band gap energy of ZnO (Muthulingam et al., 2016).

The research team studied the fabrication of CDs/N-ZnO and the photocatalytic effect of this nanocomposite in degrading malachite green (MG) dye in water, by using UV, visible and daylight sources (Muthulingam et al., 2016). The preparation of CDs used 50 mg of carbon black pigment as the carbon precursor, which is added into a mixture of 13 mL sulphuric acid (H_2SO_4) and 6.5 mL nitric acid (HNO_3). The mixture was sonicated at room temperature for several minutes for a better dispersion. Then, the reaction temperature was raised and maintained at 240 ºC for 2 hours before letting it cooled down naturally to room temperature. To isolate the CDs, reaction mixture was neutralized with 1 M sodium hydroxide (NaOH) solution at room temperature where the excess salts were separated by dialysis for 2 days. Eventually, the final CDs obtained have an average particle size of 2.5 nm.

N-doped ZnO was prepared separately from the CDs, where 1.25 g of zinc acetate dihydrate was first dissolved completely in 125 mL of double distilled water. Approximately pH 10 was kept by adding aqueous ammonia solution (nitrogen source) into the solution. After filtering the resultant clear solution, it was mixed with double distilled water (50 mL) and maintain at a temperature of 60 ºC by using a constant temperature bath for 26 hours. Eventually, white crystals of N-ZnO photocatalyst were obtained after being washed with distilled water and ethanol for several times and dried.

To combine the acquired CDs with N-ZnO, 10 μL of CDs solution was mixed with 50 mg of N-ZnO crystals by dispersing in 25 mL of ethanol and stirred for 30 minutes at room temperature. After filtration, washed with ethanol and dried, the final product of CDs/N-ZnO photocatalyst was obtained. Next, to test the activity of CDs/N-ZnO, a suspension containing 5 mg of photocatalyst and 100 mL of aqueous MG dye solution was placed in a glass beaker and agitated in the dark for 30 minutes to establish a control experiment for the absorption-desorption equilibrium.

CDs/N-ZnO possessed a spherical shape under the high magnification SEM images. Moreover, the absorption range of CDs/N-ZnO was extended from UV region to visible light region, with a lower band gap from 3.21 eV to 3.1 eV. This proved that the addition of CDs improved the light absorption range of the photocatalyst.

Furthermore, the photocatalytic result showed that CDs/N-ZnO photocatalyst was able to achieve a degradation efficiency of 100% on MG dye after 30 minutes of daylight irradiation. Furthermore, the CDs/N-ZnO photocatalyst also showed enhanced photocatalytic performance in both UV and visible light sources, where 100% MG dye degradation was achieved within 30 minutes irrespective of the light sources as displayed in Figure 2.7.

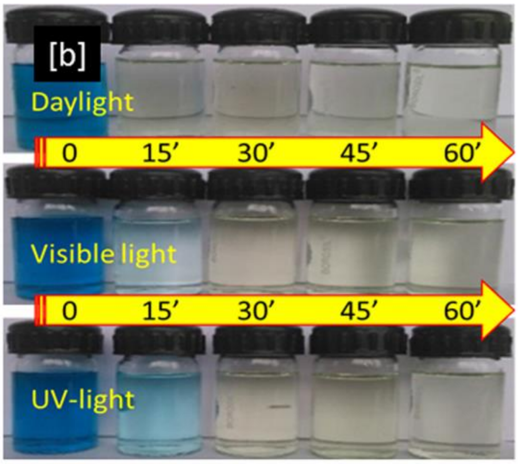

Figure 2.7: CDs/N-ZnO Photocatalyst Degraded The Entire MG Dye Within 30 Minutes of Light Irradiation (Muthulingam et al., 2016).

2.5.3 Nitrogen-Doped Carbon Dots Sensitized Bismuth Tungstate Photocatalyst (N-CDs/Bi_2WO_6)

Zhang et al. (2018) synthesized N-CDs/Bi_2WO_6 and further investigated the photodegradation property of this nanocomposite on tetracycline (TC) from antibiotics in pharmaceutical wastewater under visible light irradiation.

Bismuth tungstate (Bi_2WO_6) is a semiconductor-based photocatalyst that has been developed for its visible light absorption feature caused by its suitable band gap. Bi_2WO_6 also have relatively high photostability, nontoxicity to the environment, superior band composition and unique crystal structure that benefit its photocatalytic property (Zhang et al., 2018). However, similar to most semiconductor-based photocatalyst, pure Bi_2WO_6 faces challenges for its quick photogenerated electron-hole recombination, difficulty in electron migration and poor efficiency in harvesting visible light.

Traditionally, to overcome these problems, ion doping and coupling with various semiconductors were used to improve the photocatalytic activity of Bi_2WO_6. Unfortunately, these methods involve large-sized materials that are unable to construct the perfect interfaces where surface defects can be found on the interfaces of the hybrid structures. This causes the electron-hole pairs to easily recombine on the surface defects and thus reduces the photocatalytic performance. For this reason, small-sized CDs are preferred for their uniform size distribution as well as the excellent electron transfer and reservoir properties (Zhang et al., 2018).

N-CDs/Bi_2WO_6 was fabricated via a facile hydrothermal method. N-CDs were first synthesized by mixing 5 mmol ammonium citrate in 10 mL deionized water with 335 μL ethylenediamine (EDA), where the mixture was stirred for 30 minutes before being transferred into a 25 mL Teflon-lined autoclave. The solution was heat treated at 200 ºC for 5 hours. Then, the reactor was cooled down to room temperature. N-CDs solution was obtained after being subjected to dialysis for 24 hours.

Next, the combination of N-CDs and Bi_2WO_6 was also performed through the facile hydrothermal method. Solution A was prepared by dissolving 1 mmol $Bi(NO_3)_3{\cdot}5H_2O$ in a 20 mL aqueous solution with 1 mmol of nitric acid to come out with a clear solution; solution B was prepared by dissolving 0.5 mmol $Na_2WO_4{\cdot}2H_2O$ in certain amount (0, 1, 3, 5 and 8 mL) of N-CDs aqueous solution, and further added 20 mL of deionized water. Solution B was added dropwise into solution A and continuously stirred for 2 hours. The suspension obtained was placed in a 50 mL autoclave and heat treated at 160 ºC for another 20 hours. After cooled, the samples were washed with distilled water and dried in oven at 60 ºC overnight. The obtained N-CDs/Bi_2WO_6 photocatalysts were named according to the amount of N-CDs added in solution B, where the addition of 0, 1, 3, 5 and 8 mL of N-CDs were names as pure Bi_2WO_6, N-CDs/Bi_2WO_6-1, N-CDs/Bi_2WO_6-3, N-CDs/Bi_2WO_6-5 and N-CDs/Bi_2WO_6-8 respectively (Zhang et al., 2018).

Under SEM and TEM, N-CDs/Bi_2WO_6 appeared as a sphere-like structure with an average particle size of 2-5 μm. Besides, the SEM image also showed that the entire sphere-like structures of N-CDs/Bi_2WO_6 were mainly constructed by numerous nanosheets intercrossing each other and aggregated together (Zhang et al., 2018). The unique structure of nanocomposite contributed to the higher surface area and thus higher number of active sites for photocatalysis reaction.

Among the prepared samples, N-CDs/Bi_2WO_6-5 showed the highest photocatalytic efficiency, where the TC degradation achieved 97% under visible light irradiation for 25 minutes, while pure Bi_2WO_6 only able to achieve 77.9% TC degradation under the similar light irradiation. The degradation efficiency of N-CDs/Bi_2WO_6-5 was much higher than pure

Bi_2WO_6, indicating that N-CDs efficiently enhanced the photocatalytic activity of Bi_2WO_6 (Zhang et al., 2018).

2.5.4 Carbon Dots Doped with Cadmium Sulphide Microspheres (CDs/CdS)

Cadmium sulphide (CdS) is an important group II-VI semiconductor, which has been investigated for its photocatalytic property (Liu, Yu and Zhang, 2013). Having a band gap of 2.4 eV, CdS is suitable to absorb solar spectrum for energy conversion. Unfortunately, CdS is prone to photocorrosion due to the self-oxidizing property of S^{2-} ion in CdS by the photogenerated holes during the photocatalytic reaction (Fan et al., 2016). Hence other materials used to combine with CdS must be able to suppress photocorrosion effectively.

In this particular research, CDs were synthesized through the electrochemical exfoliation of graphite. The electrochemical exfoliation process was operated in 0.1 M sodium ethoxide (C_2H_5ONa) solution via cyclic voltammetry scanning in 0 - 10 V at 0.5 V/s (Liu, Yu and Zhang, 2013). After some time, the colourless electrolyte solution was found to change its colour into yellowish and eventually a dark brown solution was obtained. CDs were separated by centrifugation and dialysis where the final yellow aqueous solution was obtained (Liu, Yu and Zhang, 2013).

A mixture containing 1 mmol of $Cd(NO_3)_2{\cdot}4H_2O$. 3 mmol of thiourea and 0.6 mmol of glutathione were stirred vigorously for 1 hour to achieve homogeneity. It was then put in a 50 mL autoclave and heated at 200 ºC for 3.5 hours. After centrifugation and dried at 80 ºC for 12 hours, CdS sediments were obtained and added with certain amount of CDs solution (Liu, Yu and Zhang, 2013).

To test the photocatalytic property of CDs/CdS on rhodamine B (RhB), 30 mg of pure CdS and CDs/CdS photocatalysts were added into 30 mL of 1×10^{-5} mol/L RhB solution and exposed to a 300 W tungsten halide lamp for photocatalysis to occur. After visible light irradiation for 1 hour, the degradation efficiency of pure CdS and 1% CDs/CdS on RhB was found to be around 50% and 90% respectively, proving that the addition of CDs strongly improved the photocatalytic activity.

2.5.5 Carbon Dots with Paramagnetic Iron Oxide (CDs/Fe_3O_4)

In common wastewater treatment, photodetoxification of toxic in water requires an additional separation step to separate the photocatalysts from detoxified water to be recycled and reused. Hence, photocatalyst that can be easily separated is highly desirable for recycling and reuse. Iron oxide possesses a magnetic characteristic which has the advantage of being collected easily by an external magnetic field, thus being chosen to be the photocatalyst used to combine with CDs in this particular research (Wang et al., 2014).

The fabrication of CDs/Fe_3O_4 was conducted through the one-pot solvothermal method by simply mixing the iron precursor, ferrocene with hydrogen peroxide (H_2O_2) dissolved in acetone at 200 ºC (Wang et al., 2014). This step was done to decompose the ferrocene into iron and cyclopentadiene. The carbon source was then obtained from the rupture of C-H bonds in cyclopentadiene, forming carbon-based free radicals that were further aggregated to form larger CDs under high temperature and pressure in the reactor (Wang et al., 2014). Meanwhile, H_2O_2 decomposed into O_2 molecules that oxidized the Fe atoms to form Fe_3O_4. Under such high temperature and pressure of the reactor, the CDs and Fe_3O_4 formed will bind together to form CDs/Fe_3O_4 photocatalyst.

TEM image showed that the shapes of CDs/Fe_3O_4 photocatalysts were nearly uniform in a flower-like nanoparticle with an average diameter of 100 nm. The flower-like structure indicated the clustering of Fe_3O_4 atoms at the core while CDs assembled at their surfaces, as illustrated in Figure 2.8.

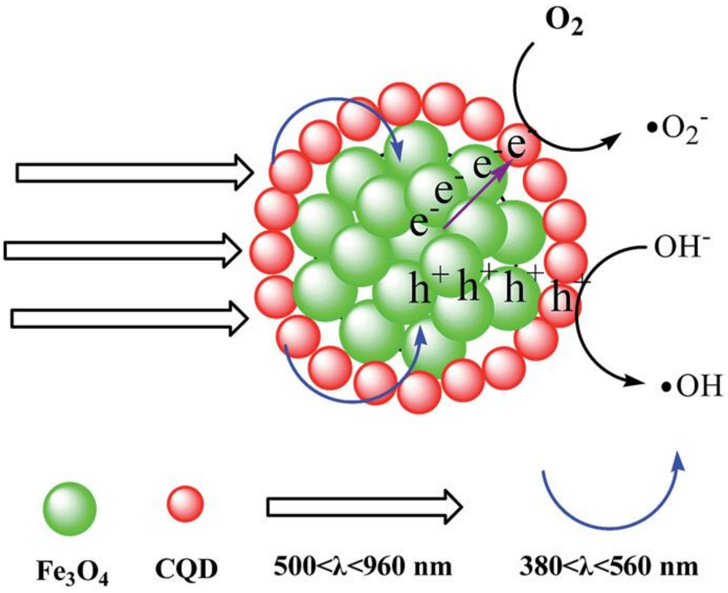

Figure 2.8: The Proposed Catalytic Mechanism of CDs/Fe_3O_4 under Visible Light (Wang et al., 2014).

Photocatalytic activity of CDs/Fe_3O_4 was tested to degrade methylene blue (MB) dye under visible light irradiation. 3 mL of 0.001 M MB solution was added with 1 mg of CDs/Fe_3O_4, revealing that photodegradation of MB dye achieved 94.4% efficiency under the exposure of 75 W Xenon lamp for 30 minutes (Wang et al., 2014). Besides, CDs/Fe_3O_4 can be easily recovered by using an external magnetic field to be reuse.

The nanocomposites synthesis methods and the photocatalytic result for various CDs hybrids mentioned above are summarized in Table 2.6.

Table 2.6: Summary of the Synthesis Methods and Photocatalytic Activity for Various CDs Photocatalyst Nanocomposites.

Nanocomposite	**CDs Precursor**	**Synthesis Technique**	**Toxic Component**	**Light Source**	**Exposure Duration**	**Photocatalytic Degradation Efficiency**	**Reference**
Pb-CDs-TiO2	Ascorbic acid	Microwave-assisted method	RBX, CRB and CNB dye	Visible light	50 min	RBX – 100% CNB – 99% CRB – 96%	(Mehta et al., 2018)
CDs/N-doped-ZnO	Carbon black pigment	Hydrothermal	MG dye	Daylight	30 min	100%	(Muthulingam et al., 2016)
N-CDs/Bi_2WO_6	Ammonium citrate	Hydrothermal	TC	Visible light	25 min	97%	(Zhang et al., 2018)
CDs/CdS	Sodium ethoxide	Electrochemical exfoliation	RhB dye	Visible light	1 hour	90%	(Liu, Yu and Zhang, 2013)
CDs/Fe_3O_4	Ferrocene	Solvothermal	MB dye	Visible light	30 min	94.4%	(Wang et al., 2014)

2.6 Photocatalytic Membrane

According to Shi et al. (2019), typical photocatalysts exist in suspended powder form such as nanosheets, nanotubes, nanorods, nanowires and nanoparticles. The powder form photocatalysts are superior in terms of their specific surface area which leads to the excellent photocatalytic performance in photocatalytic reactor (Fischer et al., 2015). These nanosized photocatalysts must be recovered from the treated water for recycling purpose as well as to avoid any secondary pollution caused by the nanosized photocatalysts. However, the recovery of nanosized photocatalysts from treated water is typically complicated and varying depending on the property of different photocatalysts. Some of the separation methods of photocatalysts from detoxified water are costly and infeasible to be carried out in large scale water treatment.

Since membrane technology has been widely used in water purification, photocatalytic membrane can be used where the photocatalysts are fixed on the membrane without losing the photocatalysts in the treated water. This technology effectively solves the trouble to separate the nanosized photocatalysts from treated water.

Besides, photocatalytic membrane has various other advantages which include its low space consumption and small installation size. By degrading the pollutants in the feed solution, photocatalytic membrane is able to prevent the formation of cake at the membrane surface, which thus reduces membrane fouling issues (Shi et al., 2019). Meanwhile, physical separation such as the entrapment of solid particles through filtration is achievable by passing the polluted water through the photocatalytic membrane (Kuvarega and Mamba, 2016). By utilising a membrane as photocatalysts support, the recycling of photocatalyst nanoparticles, photodegradation of pollutants as well as the filtration for pollutants can be integrated into a single photocatalytic membrane device (Fischer et al., 2015).

Nevertheless, photocatalytic membrane typically has lower photocatalytic activity than powdered photocatalysts as the surface area of photocatalysts largely reduced after the attachment of particles on the membrane surface (Fischer et al., 2015). Despite the lower photocatalytic performance, photocatalytic membrane is still preferable over nanosized photocatalysts owing to its small installation space, high efficiency in separation, ease of operation and relatively lower cost in a long term.

2.6.1 Porous Membrane

Typically, there are three major types of filtration models that are commonly used for photocatalysis, which are the microfiltration (MF), ultrafiltration (UF) and nanofiltration (NF) (Kuvarega and Mamba, 2016). These filtration systems are characterized mainly by the pore sizes of membranes. The pore sizes decide the selectivity of membrane, which enable them to trap specific type of contaminants while allowing particles with sizes smaller than the pore to pass through. Table 2.7 shows the particle size captured and the common contaminants that are filtered by 3 different membrane types according to the pore sizes of membranes.

Table 2.7: Characteristics of Various Types of Membranes (Kuvarega and Mamba, 2016).

Filtration Model	**Particle Size Captured**	**Typical Contaminant**
Microfiltration (MF)	0.1-10 μm	▪ Suspended solid ▪ Bacteria ▪ Protozoa
Ultrafiltration (UF)	0.001-0.1 μm	▪ Proteins ▪ Polysaccharides ▪ Colloids
Nanofiltration (NF)	0.0001-0.001 μm	▪ Virus ▪ Multivalent ions ▪ Natural organic matter

2.6.2 Polymeric Membranes

There are two major materials that are commonly used in the fabrication of membranes, which are polymeric membrane and ceramic membrane. Among these, polymeric membrane gained popularity in wastewater purification owing to its lower cost and higher permeability of the porous membrane

(Kuvarega and Mamba, 2016). Throughout the years, various polymeric membrane fabrication techniques have been developed according to the desired membrane structure and the type of polymer used. The popular techniques used to synthesize polymeric membranes include phase inversion, stretching, interfacial polymerization, track-etching and electrospinning (Lalia et al., 2013). Among these techniques, phase inversion method that was first developed by Loeb and Sourirajan back in 1960s remained as the most commonly used method due to its excellent asymmetric porous membrane structure (Zhu et al., 2017).

According to Lalia et al. (2013), phase inversion is basically a demixing process where a homogeneous polymeric solution changes from liquid state to solid state. The process of phase inversion involves the interchanging between solvent and non-solvent, which causes the polymeric solution to transform its phase for the formation of solid membrane (Al-Malek et al., 2012). Lalia et al. (2013) listed four ways to achieve the transformation of polymeric solution to solid membrane, which includes the immersion precipitation, vapour-induced phase separation, thermally-induced phase separation and evaporation-induced phase separation. Among these, the immersion precipitation is most commonly used and it is described as the immersion of a polymeric solution in a non-solvent coagulation bath where the exchange of solvent (polymeric solution) and non-solvent (coagulation bath) occurs (Lalia et al., 2013). Due to the interchange between solvent and non-solvent, phase transition occurs and thus leading to the formation of solid membrane (Al-Malek et al., 2012).

The morphology of polymeric membrane can be easily modified by changing the composition of the casting solution such as varying the polymer concentration, additive concentration and the type of solvent used. By controlling the composition of casting solution, the exchange rate between solvent and non-solvent can be altered as it is the kinetic factor that ultimately regulates the morphology of membrane. The flexibility in modifying the membrane morphology depending on the desired membrane structure makes phase inversion a rather versatile membrane fabricating technique (Zhu et al., 2017).

Next, the popular polymers that have been used in membrane fabrication include polyamide (PA), polytetrafluoroethylene (PTFE), polyethersulfone (PES), polysulfone (PSF), polyvinylidene fluoride (PVDF), polyacrylonitrile (PAN) and polyethylene terephthalate (PET) (Kuvarega and Mamba, 2016). The molecular formulas and molecular structure of these polymeric membranes are tabulated in Table 2.8.

Table 2.8: Molecular Structures of Various Polymeric Membranes (Bet-Moushoul et al., 2016).

Polymer	**Acronym**	**Molecular Structure**
Polyamide	PA	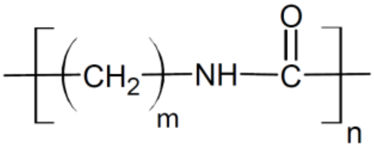
Polytetrafluoroethylene	PTFE	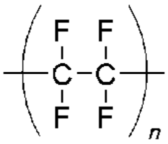
Polyethersulfone	PES	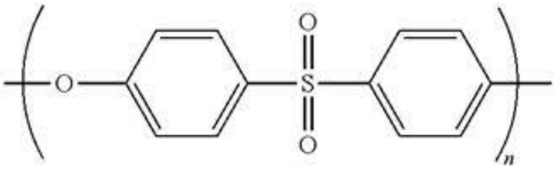
Polysulfone	PSF	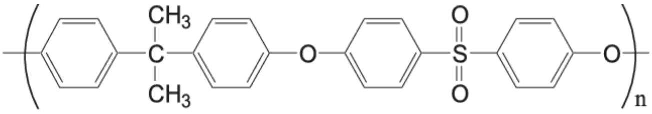
Polyvinylidene fluoride	PVDF	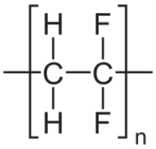
Polyacrylonitrile	PAN	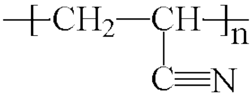 $-[CH_2-\underset{C\equiv N}{\underset{\mid}{CH}}-]_n$
Polyethylene terephthalate	PET	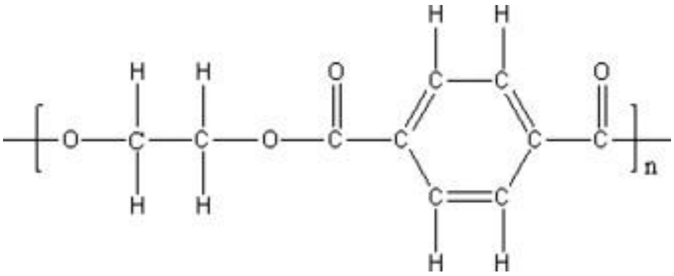

According to Shockravi et al. (2017) , PSF and PES membranes have been used extensively among the other polymeric membranes due to their excellent mechanical properties, high chemical resistance properties, high thermal and hydrolytic stability. The slight difference between PSF and PES polymer is that PES exhibits greater hydrophilicity than PSF, which is preferable to enhance the permeability and antifouling property of membrane (Shockravi et al., 2017). However, Sun and Chen (2016) stated that PES membranes have inherent hydrophobic characteristics due to the lack of oxygen containing functional groups and thus leading to the low membrane flux and inefficient antifouling properties. The hydrophilicity of membrane can be significantly improved by the incorporation of additives.

Additive in membrane casting solution plays a vital role in adjusting and improving the properties of membrane as it contributes to the formation of membrane pores and introduces the hydrophilic character to the membrane (Abdel-Karim et al., 2017). One of the popular additives that have been used extensively in membrane fabrication is polyvinylpyrrolidone (PVP) due to its nontoxicity, chemical stability and excellent solubility of various polar solvents (Junaidi et al., 2019). PVP is a highly hydrophilic polymer without the presence of ionic charged group which possesses excellent hydrophilicity, making it an outstanding pore forming reagent (Junaidi et al., 2019). By varying the PVP concentration in casting solution, the morphology of membrane can be easily modified to enhance the performance of membrane (Abdel-Karim et al., 2017).

2.6.3 Different Types of Photocatalytic Membrane

Generally, the incorporation of hybrid photocatalyst into a membrane can be either deposited on the surface of membrane or simply dispersed in the polymer solution before the casting of membrane. Based on the location of nanoparticles on the membrane, the types of photocatalytic membranes can be categorized into 4 major categories, which are the conventional nanocomposites, thin-film nanocomposites, thin-film nanocomposites with nanocomposite substrates and surface-located nanocomposites. Figure 2.9 shows the location of photocatalyst nanoparticles in different photocatalytic membranes. As mentioned, the surface located nanocomposite membrane is preferable for photocatalytic membrane as this design allows all the photocatalyst nanoparticles to be exposed to direct light irradiation and well contact with the pollutant molecules (Fischer et al., 2015).

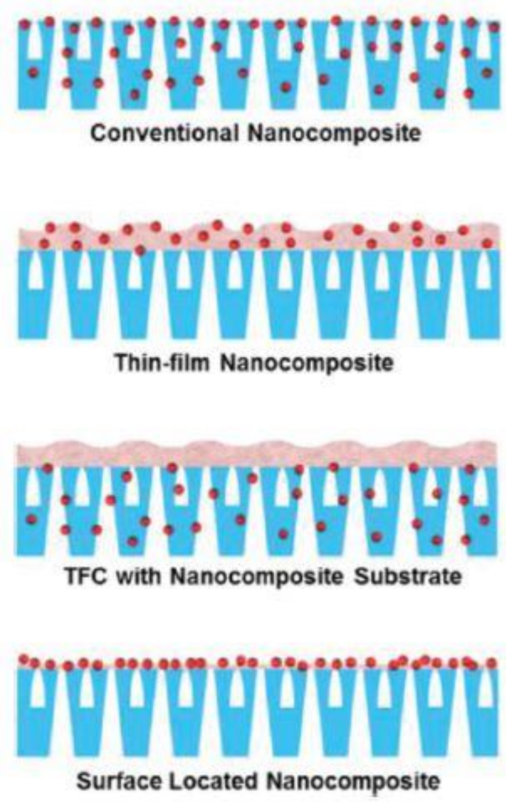

Figure 2.9: Types of Photocatalytic Membranes Based on the Location of Nanoparticles in the Membranes (Yin and Deng, 2015).

2.7 Fabrication of Photocatalytic Membranes

According to Kuvarega and Mamba (2016), several common techniques were developed and have been practised to fabricate photocatalytic membranes. The photocatalytic membrane fabrication methods for polymeric and ceramic photocatalytic membranes are illustrated in Figure 2.10, where the fabrication of surface located nanoparticles membranes typically use the ex-situ methods, while in-situ methods are used for the fabrication of membranes with entrapped nanoparticles. Since the desired photocatalytic membrane is to incorporate the photocatalyst nanoparticles on membrane surface, the detailed description of techniques used to fabricate surface located photocatalytic membrane will be discussed.

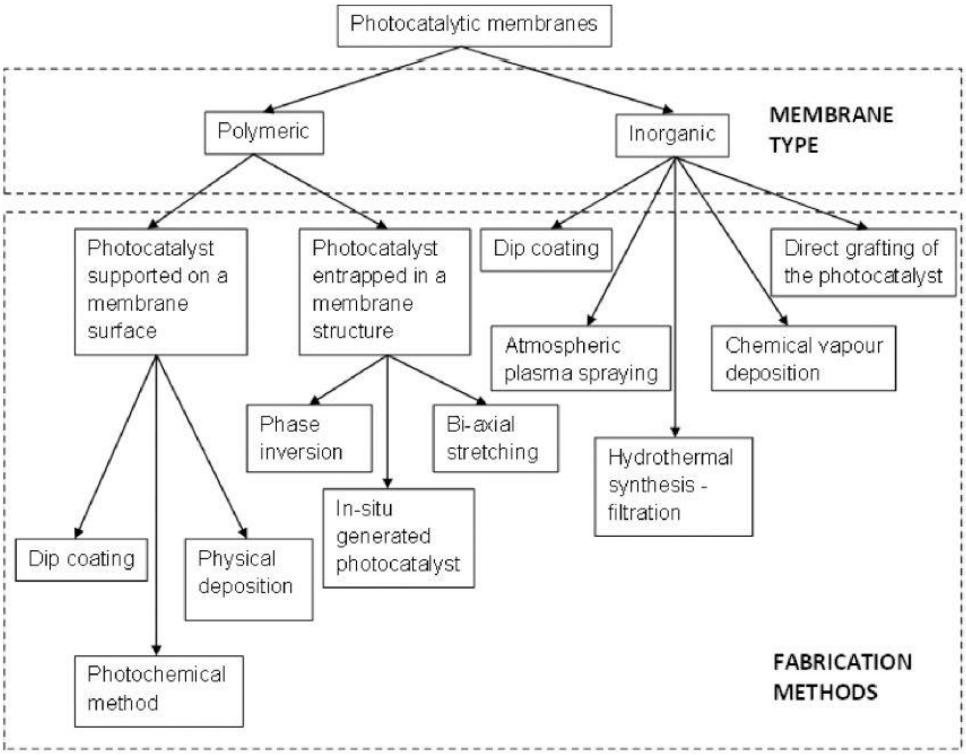

Figure 2.10: Techniques for the Fabrication of Photocatalytic Membranes (Kuvarega and Mamba, 2016).

2.7.1 Dip-coating

Dip-coating is a facile method used to incorporate photocatalytic nanoparticles onto the surface of membrane by simply dipping a clean bare membrane into a sol-gel photocatalyst slurry solution. The photocatalytic nanoparticles will self-assemble and attach to the membrane surface by bonding with the oxygen atoms from the carbonyl, carboxyl and hydroxyl functional groups located on the surface of membrane, as shown in Figure 2.11 (Kuvarega and Mamba, 2016).

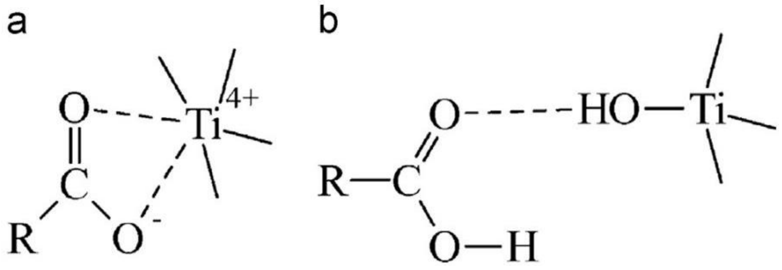

Figure 2.11: Interactions of TiO_2 Photocatalytic Nanoparticles with (a) Carboxyl Groups and (b) Hydrogen Bonding between the Hydroxyl Group from TiO_2 and the Carbonyl Group from Membrane Surface (Leong et al., 2014).

By introducing photocatalytic nanoparticles to the surface of membrane, fouling of membrane is found to be reduced due to the better hydrophilicity of membrane. However, the major limitation of dip-coating method is the weak bonding between photocatalyst nanoparticles and membrane surface. Leaching of nanoparticles tends to occur under high pressure or continuous operation (Kuvarega and Mamba, 2016).

2.7.2 Chemical Grafting

Chemical grafting has the similar bonding mechanism between photocatalyst nanoparticles and membrane surface as the dip-coating technique, which depends on the carboxyl and hydroxyl groups on the membrane surface. The only different between these two techniques is that chemical grafting involves the aid of chemical monomer which further induces more functional groups to the membrane surface, thus resulting in a stronger bond between the photocatalyst nanoparticles and membrane surface (Kuvarega and Mamba, 2016).

According to the chemical grafting technique conducted by You et al. (2012), PVDF membrane was first treated with argon plasma to generate free radicals onto the membrane surface. Appropriate amount of polyacrylic acid (PAA) was used as monomers and was mixed with ethylene glycol (cross-linker) and small amount of potassium persulfate (initiator). Next, the plasma treated PVDF membrane was first dipped into the polymerization solution for several minutes, then dipped into TiO_2 slurry for 30 minutes and irradiated with UV light for 15 minutes. The methodology and mechanism of plasma-induced chemical grafting technique conducted by You et al. (2012) is illustrated in Figure 2.12.

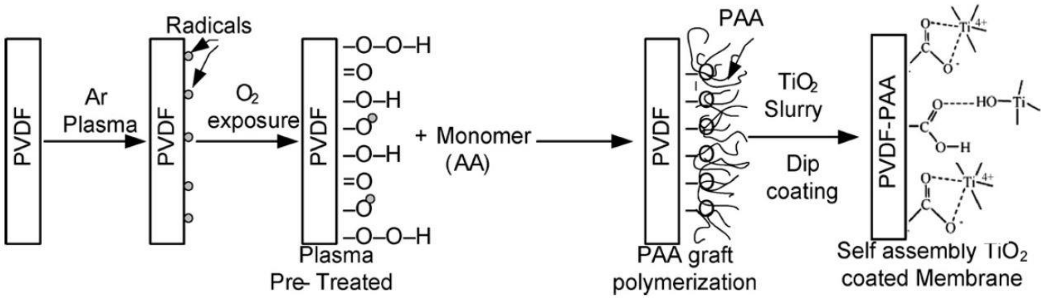

Figure 2.12: Plasma-induced Chemical Grafting of PAA and the Self-assembling TiO_2 on PVDF Membrane Surface (You et al., 2012).

Madaeni, Zinadini and Vatanpour (2011) stated that the exposure of chemically grafted photocatalytic membranes to UV light is able to improve the flux and permeability of membranes. The exposure of TiO_2 nanoparticles to UV light activates the photocatalysis reaction of TiO_2, where electrons are transferred from the capacity band to the conduction band to generate electrons and holes pairs on TiO_2 surface (Madaeni, Zinadini and Vatanpour, 2011). OH radicals and O_2^- radicals are then generated by the reaction between photo-generated electrons and the oxygen molecules from water. These generated radicals act as strong oxidizing reagents which disintegrate any contaminants around the membrane surface, thus leading to lesser membrane fouling and better membrane flux performance.

2.7.3 Physical Deposition

Physical deposition is another technique used to incorporate photocatalyst nanoparticles on membrane surface. By filtering the photocatalyst suspension across a bare membrane support, the nanosized photocatalysts are physically coated onto the surface of membrane. This indicates that the photocatalyst nanoparticles form a cake layer on the membrane surface, where the thickness of photocatalyst cake is determined by the transmembrane pressure and operating period (Kuvarega and Mamba, 2016).

Similar to the dip-coating and chemical grafting methods, physical deposition also gives high water flux as the deposited photocatalysts reduce the membrane fouling issue. However, the limitation of physical deposition is the leaching of nanoparticles from the membrane surface which is mainly due to the weak bonds between the first layer photocatalysts and the subsequent layers of photocatalysts (Kuvarega and Mamba, 2016).

Table 2.9 summarizes the methods used to fabricate surface-located nanoparticles membrane as well as the nanoparticles entrapped membrane.

Table 2.9: Summary of Techniques Used to Fabricate Photocatalyst Membrane (Kuvarega and Mamba, 2016).

Membrane Fabrication Technique		Description
Nanoparticles on Membranes Surfaces	Dip coating	Dipping of a membrane into a sol-gel photocatalyst precursor slurry solution, accompanied by further drying and pressing.
	Chemical grafting	Immobilizing photocatalyst monomers onto a membrane surface by photo-irradiation with an initiator.
	Physical deposition	Use pressure-driven filtration of photocatalyst suspension through the membrane where photocatalyst cake is accumulated on the surface of membrane

Table 2.9 (Continue)

Membrane Fabrication Technique		Description
Nanoparticles Entrapped in Membranes	Phase inversion	Most common method used to fabricate nanoparticle-entrapped membranes, where a homogeneous solution is formed by mixing photocatalyst with a polymer-doped solution, where the solution is then casted on a glass plate and dried to form the thin membrane.
	Bi-axial stretching	Physically stretch the membranes to induce significant membrane pores deformation to increase the porosity.
	In-situ generated photocatalyst	Formation of mixed matrix membranes by introducing photocatalyst nanoparticles during the membrane fabrication.

2.8 Factors Affecting the Performance of Photocatalytic Membrane

The amount of photocatalyst nanomaterials loading greatly affects the photocatalytic activity of photocatalytic membrane. Kuvarega and Mamba (2016) stated that the amount of photocatalysts that is incorporated to the membrane must be sufficient in order to achieve high photocatalytic efficiency according to the water flux of membrane. This is because when the photocatalysts amount is too low and high water flux is passing through the membrane, there will be a lack of photocatalytic active sites for attachment of all toxic compounds, hence reducing the performance of photocatalytic membrane. However, in the case when photocatalyst loading is too high, the saturated coat of nanoparticles tends to clog membrane surface pores which further reduces the membrane flux (Leong et al., 2014).

Furthermore, light intensity and duration of light source irradiation also greatly influence the photocatalytic activity (Kuvarega and Mamba, 2016). Depending on the absorption wavelength of photocatalysts, the wavelength and intensity light source should be adjusted to be efficiently utilized by the photocatalysts. In terms of irradiation time, a general rule of thumb is the longer the duration of irradiation, the higher the amount of toxic components being degraded.

Aside from the factors mentioned, some of the minor factors affecting the performance of photocatalytic membrane are the degree of particle dispersion in photocatalysts, orientation of nanoscale composite, pore size, porosity, polarity, hydrophilicity and other mechanical properties of membrane (Kuvarega and Mamba, 2016).

CHAPTER 3

METHODOLOGY AND WORK PLAN

3.1 Introduction

This section describes the procedures and methodologies of the research work. They are categorized into several parts. The first part describes the steps taken to synthesize hybrid photocatalysts and photocatalytic membranes, as well as the preparation of water containing paracetamol as pollutant sample. The second part of this section outlines the analytical instruments used for characterization of the synthesized hybrid photocatalysts and photocatalytic membrane. Last but not least, the methodology to carry out photocatalytic degradation of paracetamol and pure water flux tests will be explained. Figure 3.1 highlights the overall work plan for this research.

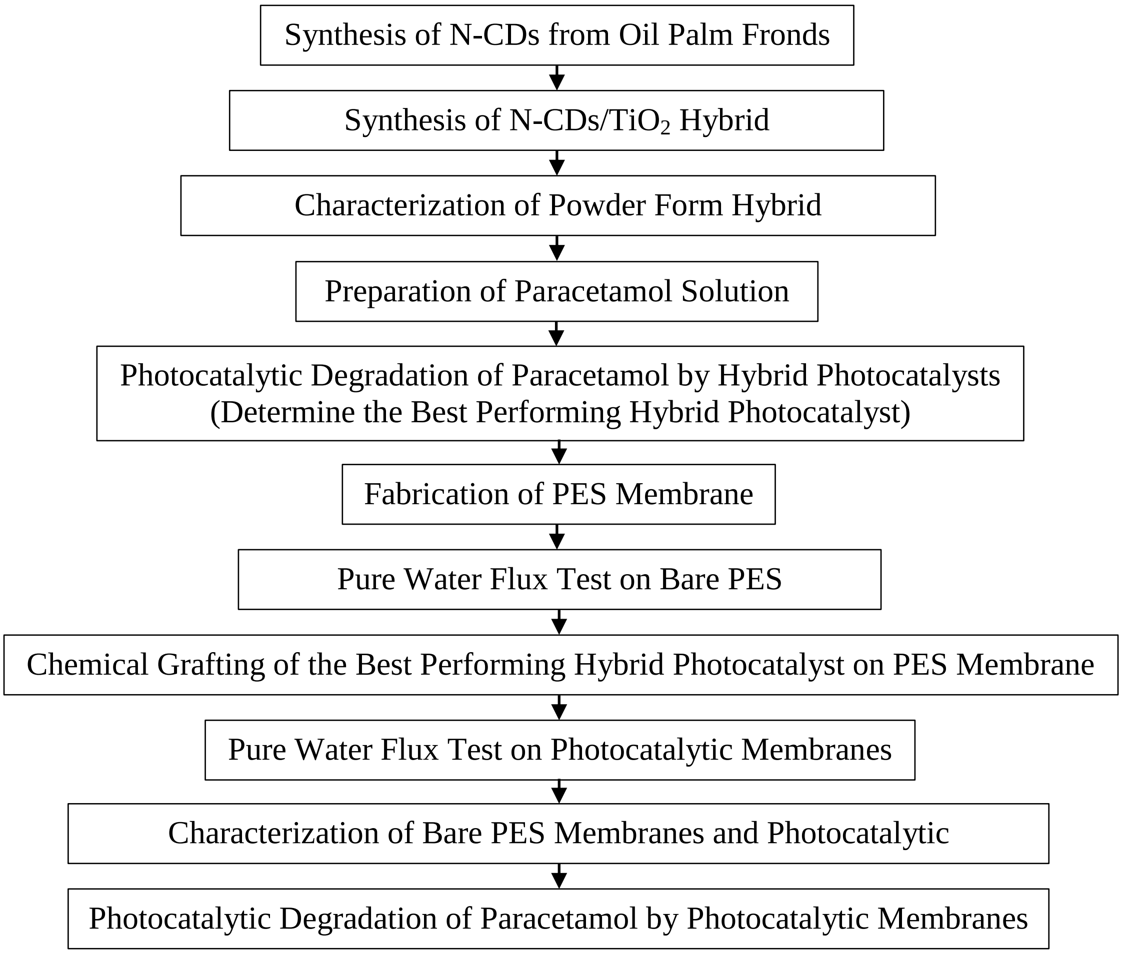

Figure 3.1: Overview of Work Plan.

3.2 Materials

Oil palm frond (OPF), distilled water, deionised water, ethylenediamine (EDA), titanium tetraisopropoxide (TTIP), isopropanol (IPA), polyethersulfone (PES) resin, *N*-methyl-2-pyrrolidone (NMP), *N*-acetyle-4-aminophenol, polyvinylpyrrolidone (PVP), polyacrylic acid (PAA), ethylene glycol (EG) and potassium persulfate (PP).

3.3 Preparation of Photocatalysts, Membranes and Model Pollutant

3.3.1 Synthesis of N-CDs from Oil Palm Fronds (OPF)

The procedure to synthesize N-CDs from OPF in this section was referring to a previous work conducted by Abdullah et al. (2019). Instead of using EFB CMC as in the work done by Abdullah et al. (2019) as mentioned in Section 2.4.2, OPFs were used as the biomass source in this study.

Firstly, raw OPFs were washed several times by using tap water and finally with distilled water to remove any impurities attached on the surface of the OPFs. The moisture was removed by drying the sample in oven at 80 ºC for a day until a constant weight of sample was obtained. Next, the dried samples were crushed into smaller pieces and sieved to obtain the uniform particle size of <300 µm, as shown in Figure 3.2.

Figure 3.2: Crushed OPFs.

Then, 6.0 g of sieved OPF sample was dispersed in 200 mL deionised water and further mixed with 23.3 wt% of EDA. The mixture was sonicated for 10 minutes before being transferred into a Teflon-lined autoclave, sealed and heated for 6 hours at 180 ºC in an oven. It was then further cooled to room temperature. The final N-CDs solution was obtained by centrifugation and filtration with 0.22 µm membrane to remove the bigger particles.

The final N-CDs solution displayed a fairly dark brown and nearly black colour as shown in Figure 3.3 (a). In order to observe the fluorescent property of CDs, sample N-CDs solution was first diluted with deionized water as the concentration of N-CDs solution produced was too concentrated for light to penetrate through the solution. The diluted N-CDs solution displayed a light yellowish brown colour as shown in Figure 3.3 (b). Under 395 nm UV light irradiation, N-CDs solution emitted bright yellowish-green fluorescent property as shown in Figure 3.4, which proved the presence of CDs.

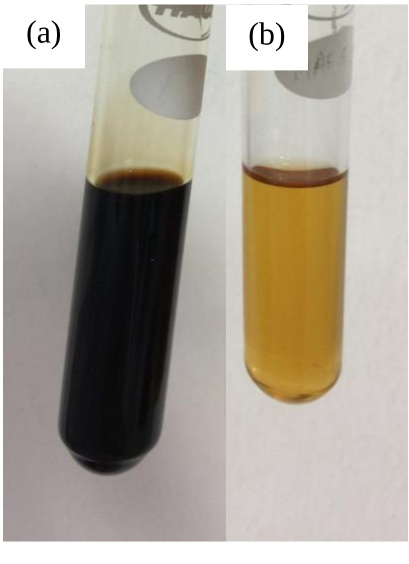

Figure 3.3: (a) Dark Brown Solution of Synthesized N-CDs Solution and (b) Light Yellowish Brown Solution of Diluted N-CDs Solution under Environment Lighting.

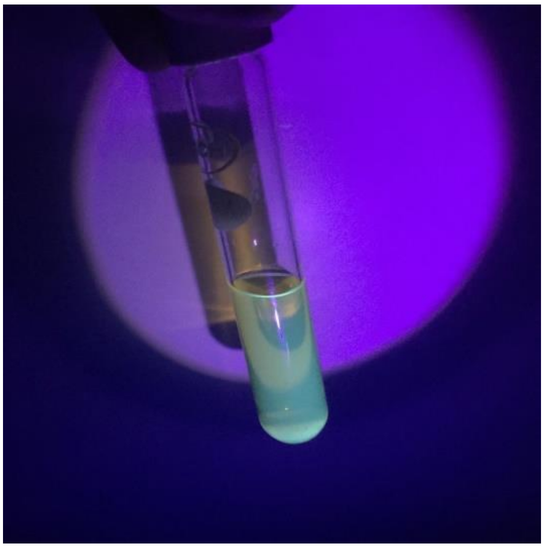

Figure 3.4: Synthesized N-CDs Solution Emitting Bright Fluorescent Yellowish-Green Colour under 395 nm UV Light Irradiation.

3.3.2 Synthesis of Pure TiO_2 and N-CDs Incorporated TiO_2

The method used to incorporate N-CDs to photocatalyst TiO_2 was referring to the study conducted by Mehta et al. (2018) and Vaiano et al. (2015). The procedure to synthesize the ex-situ hybrid photocatalysts was described as below.

Firstly, 5 mL of TTIP was added dropwise into a mixture of 10 mL deionised water and 50 mL IPA. The suspension was stirred continuously at room temperature for 2 hours before being transferred into a Teflon-lined autoclave, sealed and heated at 180 ºC for 12 hours. After that, the synthesized TiO_2 was washed with distilled water via centrifugation and further dried overnight in an oven at 80 ºC.

Next, hybrid photocatalyst can be obtained by first dispersing 1.0 g of TiO_2 in a mixture of 40 mL deionised water and 20 mL ethanol. The suspension was stirred for 5 minutes before adding a certain amount of N-CDs solution dropwise. The stirring was continued for 2.5 hours and transferred into a Teflon-lined autoclave, sealed and heated at 180 ºC for 4 hours. Finally, the as-synthesized hybrid photocatalyst was obtained after being washed several times with distilled water through centrifugation and further dried overnight at 80 ºC. Based on the amount of N-CDs solution added (0, 1, 2, 3, and 4 mL), naming of samples are tabulated in Table 3.1.

Table 3.1: Naming of the Synthesized TiO_2 and Hybrid Photocatalysts.

Sample Name	**Amount of N-CDs Solution Added (mL)**	**Description**
Pure TiO_2	0	Pure titanium dioxide photocatalyst
1HPC	1	1 mL N-CDs hybrid photocatalyst
2HPC	2	2 mL N-CDs hybrid photocatalyst
3HPC	3	3 mL N-CDs hybrid photocatalyst
4HPC	4	4 mL N-CDs hybrid photocatalyst

The synthesized TiO_2 existed in white powder form, as shown in Figure 3.5 (a). After the incorporation of N-CDs, the hybrid photocatalysts presented as light brown powder as displayed in Figure 3.5 (b), indicating that N-CDs successfully bounded to TiO_2 nanoparticles. Note that the intensity of brown colour increased as the amount of N-CDs solution incorporated increased, showing that higher amount of N-CDs had been incorporated on the TiO_2 nanoparticles.

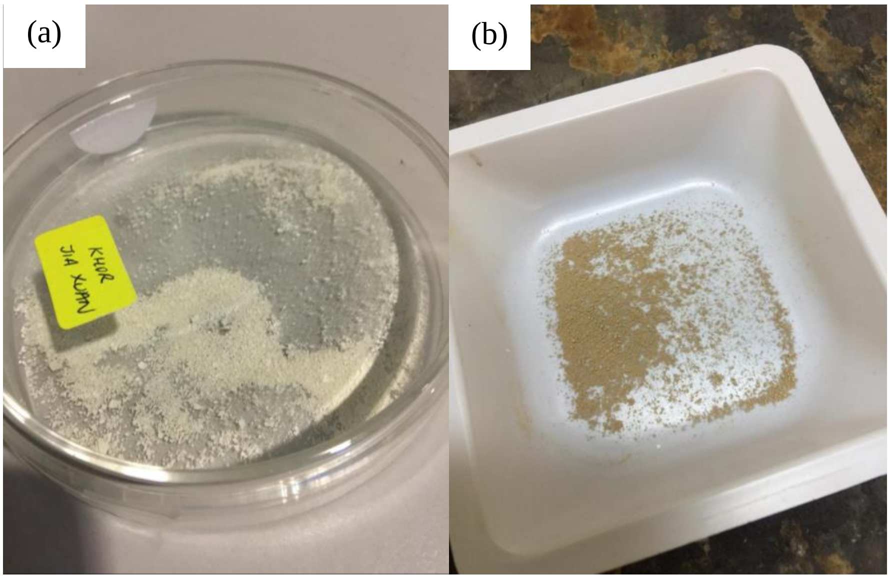

Figure 3.5: (a) White Powdered TiO_2 and (b) Brown Powdered Hybrid Photocatalyst.

3.3.3 Fabrication of PES Membrane

The synthesis of PES membrane via phase inversion method was referred to the study reported by Kassim Shaari et al. (2017). Initially, 17 wt% PES resin and a certain amount of PVP was dissolved in NMP solvent and stirred at 60 ºC and 350 rpm for 24 hours until a viscous homogeneous solution was formed. The solution was then left for 24 hours to remove the air bubbles formed. Then, the polymer solution was casted on a clean and smooth glass plate by using a casting knife with the blade height set to 200 µm. The film was left in ambient temperature for 30 seconds and then immediately immersed in water as coagulant bath for 24 hours. Figure 3.6 shows the schematic diagram of the microporous membrane preparation, while Table 3.2 summarizes the names of the synthesized bare PES membranes according to the amount of PVP added into membrane casting solution.

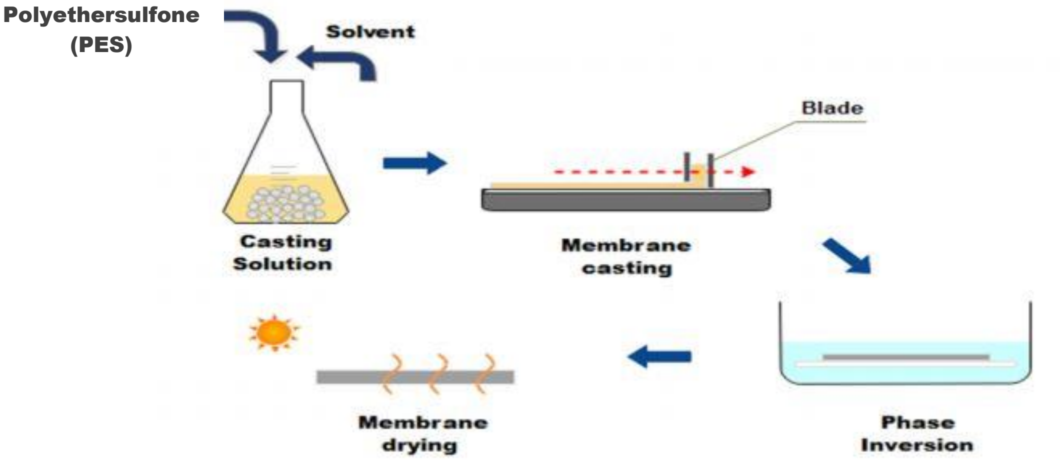

Figure 3.6: Preparation of PES Membrane via Phase Inversion Method (Kassim Shaari et al., 2017).

Table 3.2: Naming of the Synthesized PES Membrane.

Bare Membrane	Amount of PVP Added (wt%)	Description
0.5PESBM	0.5	0.5 wt% PES bare membrane
1.0PESBM	1.0	1.0 wt% PES bare membrane

3.3.4 Chemical Grafting of Hybrid Photocatalyst to PES Membrane Surface

The method used to immobilize hybrid photocatalyst to membrane surface was referring to the chemical grafting technique conducted by Madaeni, Zinadini and Vatanpour (2011), Qian et al. (2016) and You et al. (2012). Prior to the incorporation of hybrid photocatalyst to PES membrane, photocatalytic degradation test was performed on the powdered hybrid photocatalysts to determine the best performing hybrid photocatalyst. Pure water flux test was also conducted on bare PES membrane samples to select the best performing membrane. Therefore, the best performing hybrid photocatalyst (3HPC) and bare PES membrane (1.0PESBM) were used in this section.

Firstly, 50 mL of distilled water was mixed with 20 wt% PAA monomer. The polymerization solution was added with EG as the cross-linker at 1:6.5 molar ratio of EG to PAA, as well as 1 wt% of PP. The solution was continuously stirred at room temperature for 15 minutes to achieve homogeneous solution. Bare PES membrane was then dipped into the polymerization solution for 5 minutes, and then carefully placed on a clean glass plate where the air bubbles and excess solution were gently squeezed out by using a glass rod. This step was important to ensure that PAA was evenly coated on the membrane surface. Next, grafted membrane was sandwiched between two sealed glass plates and dried in an oven with a temperature of 70 ºC for 4 hours. Meanwhile, certain amount of hybrid photocatalyst was dispersed in 50 mL of distilled water and the suspension was sonicated for 15 minutes so that the nanoparticles were well-dispersed in distilled water. The dried PAA grafted membrane was then dipped in hybrid photocatalyst suspension for 30 minutes to allow the self-assembly of nanoparticles on membrane surface, as shown in Figure 3.7.

Figure 3.7: PAA Grafted Membrane Dipped in Hybrid Photocatalyst Suspension.

After 30 minutes of photocatalyst coating, the photocatalytic membrane was irradiated with 36 W UV lamp for 20 minutes. Lastly, the photocatalytic membrane was soaked in 100 mL distilled water for 30 minutes to eliminate the weakly bounded nanoparticles. The weight of the PES membrane was measured before and after chemical grafting with hybrid photocatalyst to determine the mass gain and grafting yield. Based on the concentration of hybrid photocatalyst suspension, the names of photocatalytic membranes are tabulated in Table 3.3.

Table 3.3: Naming of the Synthesized Photocatalytic Membranes.

Photocatalytic Membrane	**Amount of Hybrid Photocatalyst in Suspension (wt%)**	**Description**
0.1PESPCM	0.1	0.1 wt% PES photocatalytic membrane
0.2PESPCM	0.2	0.2 wt% PES photocatalytic membrane
0.3PESPCM	0.3	0.3 wt% PES photocatalytic membrane

The observation of the synthesized photocatalytic membranes was presented in Figure 3.8. As observed, hybrid photocatalyst nanoparticles successfully deposited on white PES membrane surface as the brown depositions were observed. Besides, the intensity of brown colour increased as the hybrid photocatalyst nanoparticles loading increased.

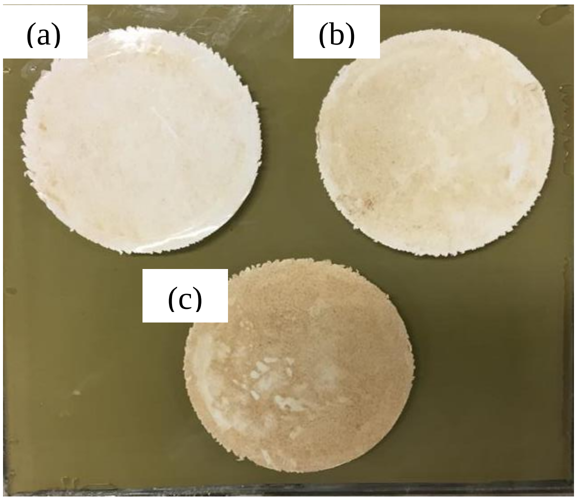

Figure 3.8: Pictures of (a) 0.1PESPCM, (b) 0.2PESPCM and (c) 0.3PESPCM.

3.3.5 Preparation of Paracetamol Solution

Paracetamol solution as model pollutant was prepared in two different concentrations, which were 10 ppm for the photocatalysis of powdered hybrid photocatalysts, and 4 ppm for the photocatalysis of photocatalytic membrane. The use of lower paracetamol concentration for photocatalysis by photocatalytic membrane was mainly due to the lower loading of photocatalyst nanoparticles on membrane surface.

To prepare the paracetamol solution, powder form *N*-acetyle-4-aminophenol (chemical name of paracetamol) was dissolved in distilled water in a 1 L volumetric flask. Table 3.4 tabulates the composition of the paracetamol solutions. The resultant suspensions were analysed with UV-visible spectrophotometer to identify the maximum absorption wavelength of paracetamol.

Table 3.4: Composition of Paracetamol Solutions.

Paracetamol Concentration (ppm)	**Mass of Powder Paracetamol (g)**	**Volume of Distilled Water (L)**
4 ppm	0.004	1
10 ppm	0.01	1

3.4 Characterization

In this study, characterization was performed in two sections. The first characterization was carried out on photocatalytic nanoparticles by using FTIR, XRD, SEM-EDX and zeta potential analysis, while the second characterization will be on the membranes by using FTIR and SEM. Characterization is essential to predict the effect of the varying parameters on the photocatalytic activity and performance of photocatalytic membrane in degrading pharmaceutical waste. This section describes the analytical instruments and methods used for characterization.

3.4.1 X-ray Diffraction (XRD)

Crystallite structure, crystallite size and phases of pure TiO_2 and hybrid photocatalyst samples were determined by using XRD analysis. Prior to XRD analysis, powdered TiO_2 and hybrid photocatalyst samples were grinded into smaller particle sizes by using mortar and pestle as shown in Figure 3.9.

Figure 3.9: Grinding of Synthesized TiO_2 by Using Mortar and Pestle.

Next, the crushed powdered samples were compacted in sample holders for XRD analysis. The XRD analysis was performed with Cu Kα radiation with wavelength λ = 1.54 Å and operated at 40.0 kV and 30.0 mA with a scanning rate of 2°/min. The crystal sizes of photocatalysts were determined by using the Scherrer equation (Praveen et al., 2014).

$$D = \frac{K\lambda}{\beta cos\theta} \tag{3.1}$$

where

D = crystallite size

K = Scherrer's constant (0.89)

λ = wavelength of target

β = peak width

θ = angle between the beam and the normal to the reflecting plane

3.4.2 Fourier Transforms Infrared Spectrometer (FTIR)

FTIR is an instrument used to identify the functional groups and characterizing covalent bonding information. It measures the range of wavelengths in infrared region that are absorbed by the samples to identify the molecular composition and structure (Davis and Mauer, 2010).

FTIR spectrums of the photocatalytic nanoparticles and membrane samples were obtained from FTIR spectrometer ranged from 4000 to 400 cm^{-1}. Dried hybrid photocatalysts and photocatalytic membranes were placed on the clean sample slot, where the FTIR detector was then tighten until it was well contacted with the samples for the radiation of infrared light and analysis by FTIR spectrometer.

3.4.3 Scanning Electron Microscopy with Energy Dispersive X-ray Spectroscopy (SEM-EDX)

Electron microscope focuses a beam of highly energetic electrons on the surface of sample and provides detailed high resolution images by detecting the secondary or backscattered electron signal. SEM examines the morphology and crystallographic of sample, while the compositional information of sample can be identified with the use of EDX (Mutalib et al., 2017).

The surface morphology and cross-sectional analysis of both photocatalytic nanoparticles and photocatalytic membranes were performed by SEM operating at 15.0 kV. For SEM analysis on membrane cross-sections, the sample membranes were first cut into smaller pieces and dipped in liquid nitrogen for 30 s to be fractured cryogenically in order to obtain the clean cut of cross-section images (Zangeneh et al., 2019). Since all samples were non-conducting materials, they are first mounted on aluminium stubs for support and were coated with palladium under vacuum condition to conduct electricity.

3.4.4 Zeta Potential Analysis

Malvern Zetasizer NanoZS 90 was used to analyse the zeta potential of paracetamol and the synthesized powdered photocatalysts. 0.005 g of powdered paracetamol, 1HPC, 2HPC, 3HPC and 4HPC were mixed with 50 mL distilled water and were sonicated to achieve well-dispersed suspension. These suspensions were then placed in a cuvette to be analysed by the zetasizer to identify the surface charges of particles in neutral environment (pH 7). Besides, the mean particle size of pure TiO_2 can also be determined via zetasizer. In order to achieve high accuracy of result, three readings were taken for each sample to obtain the mean data.

3.4.5 UV-Visible Spectrophotometer

The concentrations of samples were analysed by using UV-visible spectrophotometer, where ultraviolet and visible light were radiated on the samples and the absorption by the compounds were measured, indicating the concentration of samples. The wavelength of the prepared paracetamol solution was first determined by running the prepared paracetamol solution under UV-visible spectrophotometer from 200 nm to 500 nm, under the UV region. After the wavelength of paracetamol was determined, the photocatalytic activity of the synthesized photocatalysts can be analysed by running the photodegraded paracetamol sample solution extracted at different irradiation time under the wavelength of paracetamol by using UV-visible spectrophotometer. Since the wavelength of paracetamol solution is within the UV region, quartz cuvette was used to hold the samples.

3.4.6 Membrane Grafting Yield

Upon the immobilization of photocatalyst nanoparticles on the membrane surface, the mass gain on membrane was calculated by Equation 3.2, while the grafting yield was computed by using Equation 3.3 (Qian et al., 2016).

$$M\ (\%) = \frac{m_f - m_i}{m_i} \tag{3.2}$$

where

M = mass gain, %

m_i = mass of membrane before grafting, g

m_f = mass of grafted and dried membrane, g

$$G\ (\%) = \frac{m_f - m_i}{m_c} \tag{3.3}$$

where

G = grafting yield, %

m_i = mass of membrane before grafting, g
m_f = mass of grafted and dried membrane, g
m_c= mass of photocatalysts added to dipping solution, g

3.5 Photocatalytic Activity Study

3.5.1 Photocatalytic Degradation by Hybrid Photocatalysts

The first photocatalytic test was carried out in suspension form. 0.05 g of the hybrid photocatalysts was added into 50 mL of 10 ppm paracetamol solution, while a constant stirring was fixed at 450 rpm for each photocatalytic test conducted to ensure that the type of photocatalysts used was the only manipulating variable. Prior to the photodegradation test, the maximum absorption wavelength of paracetamol was identified as 243 nm by scanning the prepared paracetamol solution with UV-visible spectrophotometer. Besides, the mixture of paracetamol and photocatalytic nanoparticles were stirred continuously in dark for 30 minutes to ensure complete adsorption of paracetamol molecules to the surface of photocatalysts before switching on the light. The photocatalysis was conducted for 60 minutes, where 4 mL of paracetamol solution was extracted every 15 minutes to be analyzed by UV-visible spectrophotometer.

3.5.2 Photocatalytic Degradation by Photocatalytic Membranes

A bare PES membrane and the prepared photocatalytic membranes were cut into circles with an area of 14.6 cm^2. The membranes were then placed on top of a mesh, and then soaked in 50 mL of 4 ppm paracetamol solution, where a magnetic stirrer was placed under the mesh in order to stir the paracetamol solution at constant speed of 250 rpm. Similar to the photocatalytic test conducted on powdered photocatalysts, membranes were also soaked in paracetamol solution in dark with constant stirring (below mesh) for 30 minutes before being irradiated with 100 W LED lamp. The photocatalysis was carried out for 180 minutes where 4 mL of samples were extracted at 30 minutes interval for the analysis under UV-visible spectrophotometer. The setup of photocatalytic degradation by membranes was shown in Figure 3.10.

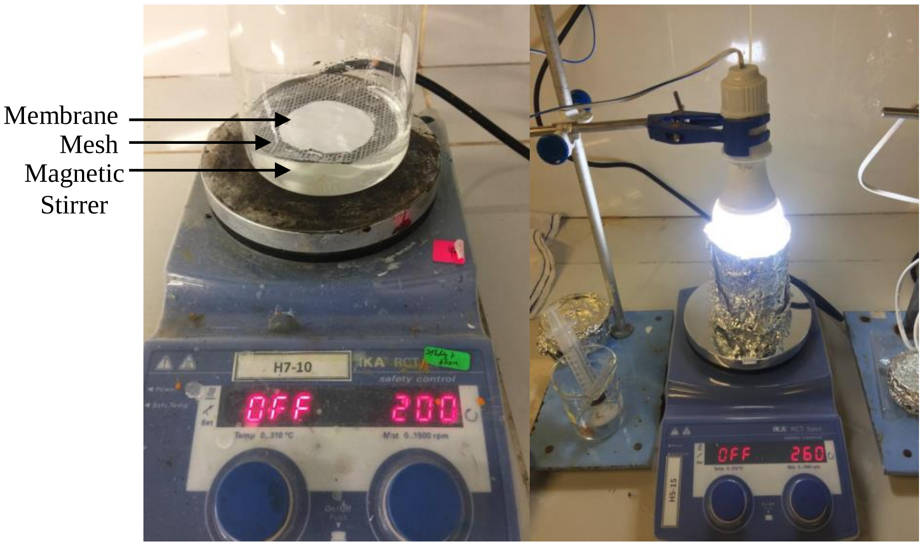

Figure 3.10: Setup of Photocatalytic Degradation of Paracetamol by using Bare PES Membrane and Photocatalytic Membranes.

To analyse the photocatalytic activity of each prepared powdered photocatalyst and the synthesized membranes, the initial and final concentration of paracetamol obtained as the peak absorption via UV-visible spectrophotometer were used to determine the percentage removal of paracetamol by using Equation 3.4 (Hoseini et al., 2017).

$$\%\, Removal = \frac{Abs_i - Abs_f}{Abs_i} \times 100\% \tag{3.4}$$

where

Abs_i = initial absorption of paracetamol solution

Abs_f = final absorption of paracetamol solution

Furthermore, by applying the photodegradation kinetics, the rate constant for each photocatalytic degradation of paracetamol can be obtained by plotting a linear graph of Equation 3.5, where rate constant is the gradient of linear curve (Qian et al., 2016).

$$ln\frac{C_o}{C} = kt \tag{3.5}$$

where

C_o = initial paracetamol concentration

C = final paracetamol concentration

k = rate constant

t = irradiation time

3.6 Pure Water Flux and Permeability

Lastly, pure water flux (PWF) test was also conducted on PES membranes with different PVP amount to obtain the membrane with higher permeability for further treatment with chemical grafting. PWF test as also carried out after chemical grafting of the hybrid photocatalyst on PES membrane surface to study the effect of photocatalyst incorporation on membrane permeability.

Prior to the flux test of membranes, dead-end filtration was carried out under the transmembrane pressure of 4 bar for 15 minutes for compaction of membranes. After compaction, dead-end filtration cell with the transmembrane pressure of 2 bar and 25 ºC was used to determine the PWF across the membranes, where the flux test was conducted for 15 minutes and the mass of permeate was measured and recorded at every 30 seconds interval. Equation 3.6 was applied to calculate the flux, while the permeability of membrane was calculated by applying Equation 3.7 (Madaeni, Zinadini and Vatanpour, 2011).

$$J = \frac{V}{A\,\Delta t}; V = \frac{m}{\rho} \tag{3.6}$$

where

J = pure water flux, L/m^{2}h

V = volume of permeated water, L

A = membrane area, 0.00146 m^2

Δt = permeation time, h

m = mass of permeate, kg

ρ = density of water, 997 kg/m^3

$$Permeability = \frac{J}{TMP} \tag{3.7}$$

where

J = pure water flux, L/m^{2}h

TMP = transmembrane pressure, 2 bar

CHAPTER 4

RESULTS AND DISCUSSIONS

4.1 Characterization of Powder Form Photocatalysts

4.1.1 X-Ray Diffraction (XRD) Analysis

The synthesized TiO_2 and hybrid photocatalyst nanoparticles were characterized by using XRD analysis to identify the crystallographic phase, crystal structure and the average crystallite sizes of sample particles. The effects of the addition of N-CDs on the crystallization of TiO_2 can be studied through XRD analysis. Figure 4.1 shows the XRD patterns of the pure TiO_2 and hybrid photocatalysts. The XRD patterns of all the photocatalysts revealed rather broad peaks, indicating the small crystallite sizes of powdered samples. According to the XRD patterns, pure TiO_2 displayed the intense diffraction peaks at 25.32°, 36.32°, 37.99°, 48.00°, 54.55°, 62.65°, 63.94°, 70.24°, 75.23° and 78.22° which were referring to the (101), (103), (004), (200), (105), (204), (118), (220), (215) and (301) planes respectively. The XRD pattern was in good agreement with the anatase phase TiO_2 diffraction peaks as reported by Bagheri, Shameli and Abd Hamid (2013). Similarly, the XRD patterns of hybrid photocatalysts showed strong diffraction peaks similar to the diffraction peak positions as the pure anatase TiO_2. The major peak of graphitic carbon about 25° was overlapping with the strongest peak of the pure TiO_2 at 25.32° as shown in the XRD pattern of the hybrid photocatalysts. This indicated that the addition of N-CDs did not alter the crystal structure of TiO_2 but well-fitted with the structure of the anatase TiO_2 (Ahmadi et al., 2017).

The crystallite sizes of the TiO_2 and hybrid photocatalysts were estimated by Scherrer's formula (Equation 3.1) and the calculations were attached in Appendix A. Based on the diffraction peaks, the average crystallite sizes of TiO_2, 1HPC, 2HPC, 3HPC and 4HPC calculated were 20.56 nm, 9.13 nm, 13.35 nm, 16.32 nm and 9.87 nm respectively. Although the crystallite sizes of hybrid photocatalysts portrayed no trend due to the uneven particle sizes distribution of nanoparticles, all the hybrid photocatalysts have smaller crystallite sizes than the pure TiO_2 due to the effect of attachment of N-CDs to TiO_2 surface which reduced the agglomeration of the TiO_2 molecules (Ahmadi et al., 2017). The relatively smaller crystallite sizes of hybrid photocatalysts indicated that the N-CDs doped TiO_2 photocatalysts had high surface areas and abundant active sites, thus could be able to increase the overall photocatalytic activity.

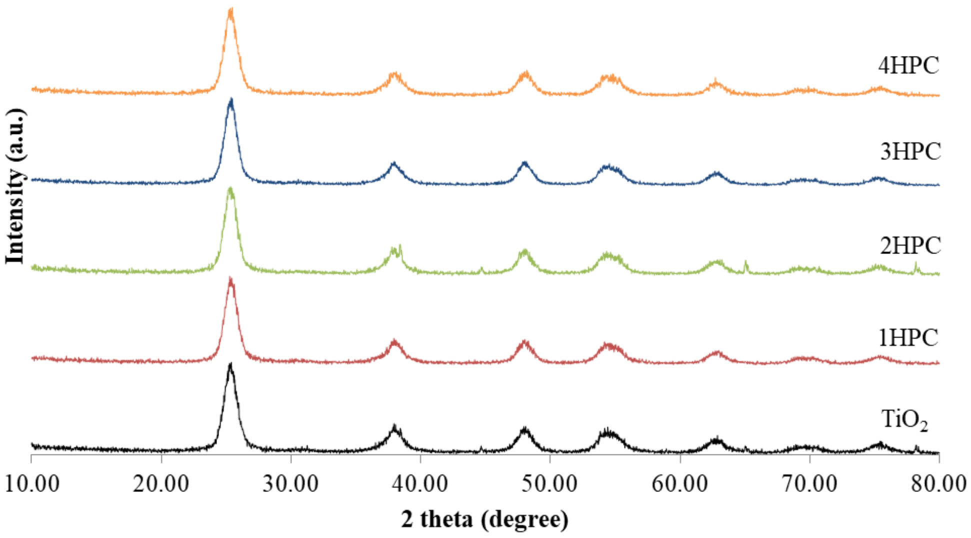

Figure 4.1: XRD Patterns of Powdered TiO_2, 1HPC, 2HPC, 3HPC and 4HPC.

4.1.2 Fourier-Transform Infrared (FTIR) Spectroscopy Analysis

FTIR analysis was carried out to identify the functional groups on the synthesized powdered photocatalysts, which included pure TiO_2, 1HPC, 2HPC, 3HPC and 4HPC. The FTIR spectrums of the powdered photocatalysts in the wavenumber range of 400 – 4000 cm^{-1} are shown in Figure 4.2.

Generally, the FTIR spectrums of the hybrid photocatalysts showed the similar peak regions as pure TiO_2. First of all, broad peaks between 1000 cm^{-1} and 400 cm^{-1} were assigned to the stretching of Ti-O and the bending vibration of Ti-O-Ti bonds in anatase titania lattice (Liu et al., 2019). Strong peaks at this region strongly affirmed the presence of Ti-O bonds, proving the formation of TiO_2.

The FTIR spectrums revealed weak and very broad peaks from 3600 cm^{-1} to 3000 cm^{-1}, which were associated to the significant hydroxyl (-OH) groups that were found on the surface of TiO_2. The result was similar to the study done by Ahmadi et al. (2017) who reported that the broad band from 3600 cm^{-1} to 3000 cm^{-1} was contributed by the O-H stretching of hydroxyl group, suggesting the presence of moisture on the surface which was described by the stretching vibrations of Ti-O-H. Besides, notice that hybrid photocatalysts showed relatively stronger O-H peaks than pure TiO_2, where the peak intensity increased with the increasing loading of N-CDs. This can be explained by the abundant hydroxyl groups attached on the surface of CDs, contributing to the higher amount of hydroxyl groups in the hybrid photocatalysts (Cong and Zhao, 2017).

Furthermore, the peaks in the range of 1750 cm^{-1} and 1500 cm^{-1} was corresponded to C=O stretching (Yan et al., 2019). For pure TiO_2, weak peak of C=O stretching was observed at 1637.02 cm^{-1}. It was a result from the interaction between O atoms and C atoms ascribed to the residual organic species from TTIP and IPA which were not completely removed by the washing with distilled water after the formation of TiO_2 (Praveen et al., 2014). As for the hybrid photocatalysts, it can be observed that the peaks became deeper with the increasing loading of N-CDs. This revealed that the stretching of C=O band for hybrid photocatalysts mainly contributed by the CDs molecules, justifying the attachment of N-CDs nanoparticles onto TiO_2 (Yan et al., 2019).

Differ from the pure TiO_2, weak bands were observed at the wavenumber of 2921 cm^{-1} and 2952 cm^{-1} for the hybrid photocatalysts. These bands were related to the vibration of C-H stretch, which indicated the presence of CDs in the N-CDs doped TiO_2 (Sim et al., 2019).

In conclusion, the FTIR spectrums strongly suggested the presence of hydroxyl groups, C=O bonds and Ti-O bonds on pure TiO_2 and the hybrid photocatalysts. Stronger O-H peaks and C=O peaks, as well as the presence of weak bands of C-H stretch on the hybrid photocatalysts justified the existence of CDs on the hybrid photocatalysts.

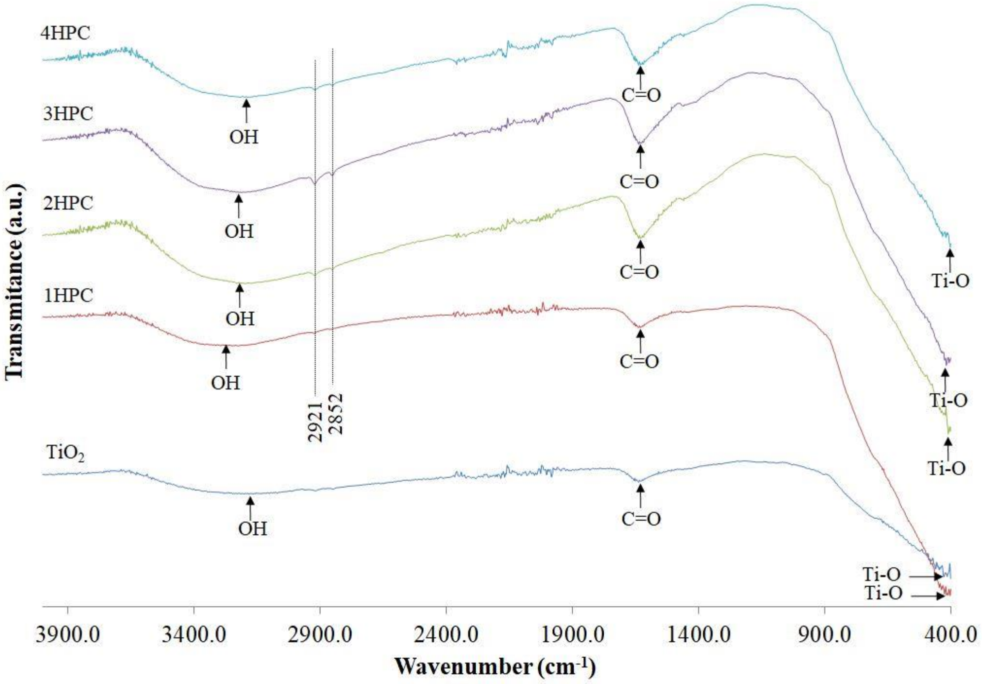

Figure 4.2: FTIR Spectrums of Pure TiO_2 and Hybrid Photocatalysts.

4.1.3 Zeta Potential Analysis

Zeta potential analysis was conducted to study the surface charges on paracetamol and the synthesized powdered photocatalysts in neutral environment (pH 7) by dissolving the powdered samples into distilled water. Besides, particle size analysis was also conducted via zetasizer to determine the mean particle size for pure TiO_2. The results obtained from zeta potential analyses for all the synthesized photocatalysts are tabulated in Table 4.1.

Based on Table 4.1, the zeta potential of pure TiO_2 was -31.2 ± 3.0 mV, indicating that TiO_2 was negatively charged in neutral environment. This finding was similar to the study by Gnanaprakasam, Sivakumar and Thirumarimurugan (2015) which clearly stated that the surface of metal oxide photocatalyst predominantly exists in negative charged. The negativity of TiO_2 showed that the adsorption of cationic molecules was easier than the adsorption of anionic molecules in neutral environment, which indicated that the photocatalytic activity of TiO_2 on cationic molecules was relatively higher than that of anionic molecules.

The zeta potential of 1HPC was -42.2 ± 1.7 mV, indicating the addition of N-CDs greatly increased the electronegativity of the TiO_2.

Moreover, the negative zeta potential of the hybrid photocatalysts increased with the increment of N-CDs loading. This might be contributed by the presence of negatively-charged functional groups on CDs, such as carboxyl group (COO^-) and hydroxyl group (OH^-) (Sang et al., 2014). Hence, the addition of CDs increased the negativity of the photocatalyst which was expected to further enhance the adsorption of cationic molecules.

As the zero point of TiO_2 is 6.3, the surface of TiO_2 is positively charged in acidic media and negatively charged in alkaline media (Jallouli et al., 2017). Besides, Kanakaraju, Glass and Oelgemöller (2014) reported that paracetamol was negatively charged in high pH condition. Thus, the adsorption of paracetamol by TiO_2 was disappointing at high pH condition due to the repulsion between the negatively charged TiO_2 and paracetamol (Kanakaraju, Glass and Oelgemöller, 2014).

According to Table 4.1, the surface potential of paracetamol was neither positive nor negative (0.1 ± 0.1 mV) in neutral environment, indicating that paracetamol had neutral surface charge. This result was in good agreement with the study conducted by Jallouli (2014) who reported that paracetamol exists as nonionic form in neutral media. Thus, the water solubility of paracetamol is minimum and its adsorption onto TiO_2 surface is maximum in neutral media (Jallouli et al., 2017). Due to the neutrality of paracetamol, Bernal et al., (2017) stated that the adsorption of paracetamol by TiO_2 photocatalyst is most favourable at slight basic or near neutrality condition (pH 7).

Next, particle size analysis via zetasizer was only conducted on pure TiO_2 as the particle sizes of N-CDs and hybrid photocatalysts were not suitable to be analyzed by using zetasizer due to their fluorescent properties which potentially disrupt the fluorescent emission by detectors (Geibler et al., 2015). From the measurement, the average particle size of the pure TiO_2 was 795.9 ± 7.2 nm, justifying the photocatalyst was in nanosize. The result of particle size analysis of the pure TiO_2 was tabulated in Table B-1 attached in Appendix B.

Table 4.1: Zeta Potential Analysis Results of Powdered Photocatalysts and Paracetamol.

Sample	**Zeta Potential (mV)**	**Average Zeta Potential (mV)**	**Standard Deviation**
Pure TiO_2	-31.0 -34.3 -28.3	-31.2	3.0
1HPC	-43.8 -42.2 -40.5	-42.2	1.7
2HPC	-42.3 -44.9 -44.6	-43.9	1.4
3HPC	-48.1 -43.8 -45.3	-45.7	2.2
4HPC	-47.3 -46.8 -44.5	-46.2	1.5
Paracetamol	-0.1 -0.1 -0.0	-0.1	0.1

4.1.4 Scanning Electron Microscopy (SEM) Analysis

As the topographies and morphologies of all the hybrid nanoparticles are quite similar, only one hybrid photocatalyst sample is discussed in this section. The surface topographies and morphologies of the TiO_2 and 3HPC nanoparticles were observed by using SEM analysis. The SEM images of the pure TiO_2 and 3HPC at magnifications of ×3,500 and ×10,000 are presented in Figure 4.3.

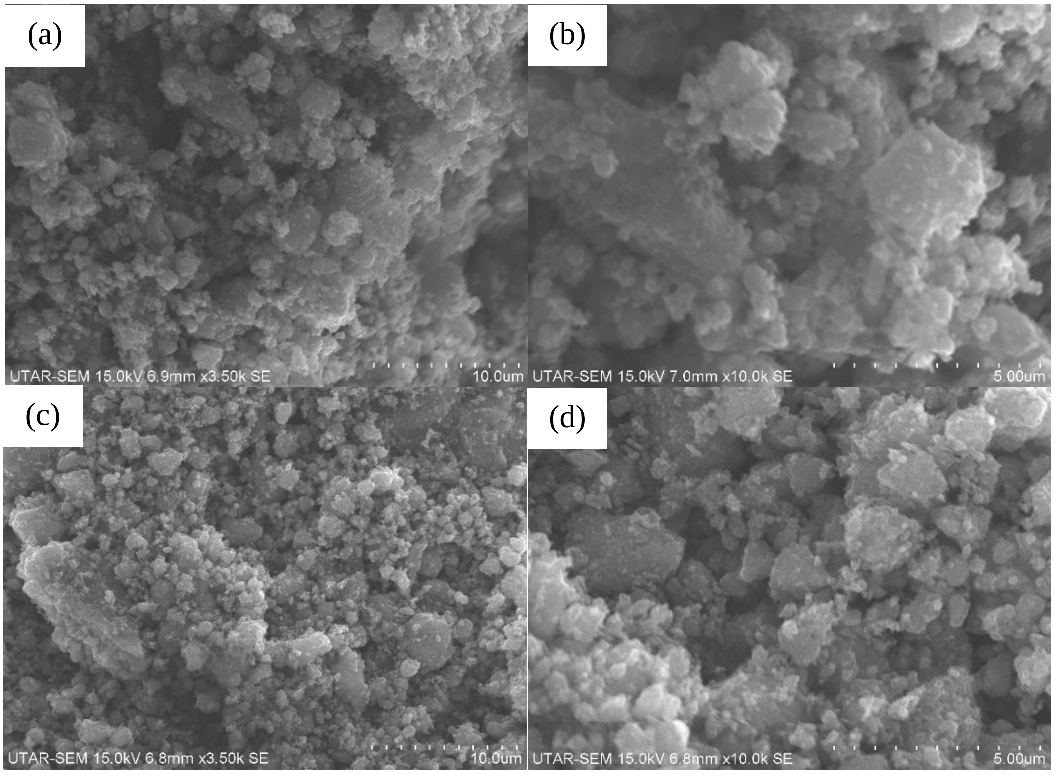

Figure 4.3: SEM Images of (a) TiO_2 at Magnification ×3,500, (b) TiO_2 at Magnification ×10,000, (c) 3HPC at Magnification ×3,500 and (d) 3HPC at Magnification ×10,000.

Based on Figure 4.3, the synthesized TiO_2 and 3HPC particles exhibited rough and uneven surface morphologies which were in agreement with the study conducted by Praveen et al. (2014). The shapes of the particles were observed to be in angular shape and the growth of the nanoparticles was said to be in high density.

The SEM images of TiO_2 and 3HPC revealed the non-uniform distribution of particles as some of the particles can be found in cluster while the others were found as single particles. The agglomeration of TiO_2 particles was expected and usually inevitable as it was largely affected by a variety of factors which mainly attributed to the surface chemistry and the synthesis conditions of TiO_2 (Praveen et al., 2014). However, it can be clearly seen that 3HPC had lesser agglomeration compared to the pure TiO_2 as the overall agglomerated particle size of TiO_2 was reduced. This finding was in good agreement with the study by Ahmadi et al. (2017) where the incorporation of

N-CDs hindered the nucleation of the TiO_2, hence resulted in smaller particle size, as discussed in XRD analysis (Section 4.1.1).

In conclusion, the SEM images of the synthesized photocatalysts displayed the high density nanosized grains in non-uniform distribution due to the agglomeration of TiO_2 particles. The incorporation of N-CDs to TiO_2 exhibited smaller agglomerated particle sizes which indicated the ability of N-CDs to reduce the agglomeration of TiO_2 particles.

4.1.5 Energy Dispersive X-Ray (EDX) Spectroscopy Analysis

EDX analysis was performed on the synthesized TiO_2 and 3HPC to identify the elemental composition of the photocatalysts. The major elements that were examined included carbon, nitrogen, oxygen and titanium which made up the overall composition of the synthesized photocatalysts. Table 4.2 summarizes the elemental composition of pure TiO_2 and 3HPC, while Figure 4.4 illustrates the EDX spectrums.

To justify the presence of TiO_2 compound, weight percentage of oxygen and titanium were not suitable for comparison as oxygen has a much lower molecular weight than titanium (O: 15.999 g/mol; Ti: 47.867 g/mol). Instead, the atomic percent of the oxygen and titanium were compared and it is found that the atomic percentage of oxygen (51.75 at%) was approximately 2 times of that of titanium (26.61 at%) for pure TiO_2 powder, strongly justified the atomic ratio of 1:2 for Ti:O. Furthermore, the atomic ratio of Ti:O was approximately 1:3.4 for 3HPC, indicating the presence of additional oxygen elements other than those that can be obtained from TiO_2 compound itself. These extra oxygen elements were attributed from the various aqueous-soluble functional groups that were attached on the surface of CDs such as carbonyl groups (C=O) and hydroxyl groups (-OH), which potentially improved the hydrophilicity of the synthesized 3HPC (Cong and Zhao, 2017).

The presence of carbon in pure TiO_2 powder (12.76 at%) may be originated from the residual organic species of the hydrothermal synthesis by using TTIP and IPA. These carbon residues were not properly removed from the washing of TiO_2 with distilled water, and thus attached on the surface of TiO_2 (Praveen et al., 2014). Surprisingly, small amount of nitrogen was also found on the surface of TiO_2 (8.88 at%). The possible explanation for the presence of nitrogen on pure TiO_2 might be due to the interaction between oxygen with nitrogen from the ambient air.

Based on Table 4.2, the amount of carbon in 3HPC greatly increased to 27.16 at%, proving the attachment of CDs on TiO_2. Despite the great increase in carbon weight percent, the amount of nitrogen on 3HPC only increased slightly, from 8.88 at% in pure TiO_2 to 12.65 wt% in 3HPC. This indicated that only a very small amount of nitrogen from EDA was successfully attached to CDs.

In brief, the result of EDX analysis confirmed the presence of TiO_2. The attachment of N-CDs on TiO_2 for 3HPC as well as the elements from functional groups attached on the surface of CDs had been verified in the EDX result.

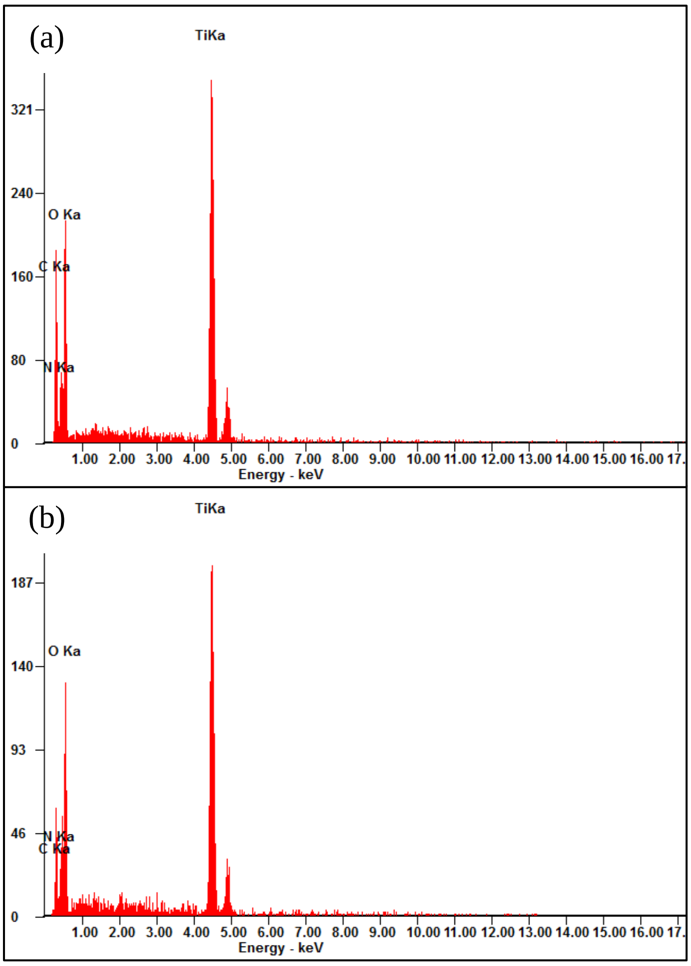

Figure 4.4: EDX Spectrums of (a) Pure TiO_2 and (b) 3HPC.

Table 4.2: Summary Result of EDX Analysis.

Element	TiO_2 atomic percent, at%	3HPC atomic percent, at%
C	12.76	27.16
N	08.88	12.65
O	51.75	46.53
Ti	26.61	13.66

4.2 Performance of Powdered Photocatalysts

4.2.1 Photocatalytic Activity under Visible Light

To study the photodegradation ability of the synthesized photocatalysts, photocatalysis of 10 ppm paracetamol were conducted by constant stirring under the light emission of a 100 W LED lamp. The UV-visible spectrophotometer results were recorded and the detailed calculations of paracetamol removal percentage were attached in Appendix C. Besides, reaction rate constant can be determined by applying photodegradation kinetics, where a graph of $\ln(C_o/C) = kt$ for the photocatalysts was plotted as shown in Figure 4.5 and the detailed calculations of $\ln(C_o/C)$ were attached in Appendix D. Table 4.3 summarizes the photocatalytic performances and rate constants of the photocatalysts.

As observed from Figure 4.5, 3HPC exhibited the highest photocatalytic performance with an excellent degradation result of 67.31% paracetamol removal after merely 60 minutes of irradiation period. In contrast, insignificant paracetamol removal of 3.14% was observed by using pure TiO_2 nanoparticles under visible light irradiation. The poor performance of pure TiO_2 nanoparticles under visible light mainly attributed to its high band gap at 3.2 eV where its optical absorption is more favourable to be activated by lower wavelength in the UV region (Mehta et al., 2018). The incorporation of CDs to TiO_2 lowers the band gap energy below 3.0 eV, thus the activation of optical absorption for hybrid photocatalysts was able to be achieved at higher wavelength of visible light region (Sharma et al., 2019).

Besides, the addition of CDs to pure TiO_2 nanoparticles reduced the unavoidable agglomeration of TiO_2 particles as proven in the crystallite size estimation in XRD analysis and from the SEM images of powdered photocatalysts. This induced that the integration of CDs to TiO_2 highly increased the surface area of photocatalysts for a higher exposure to visible light as well as more active sites for the adsorption of paracetamol.

The effect of different loading of CDs (1 mL, 2 mL, 3 mL and 4 mL) incorporated to TiO_2 on the performance of photocatalytic activity was studied. Theoretically, higher amount of CDs incorporated TiO_2 possesses greater photocatalytic performance as CDs increase the capability of optical absorption of visible light wavelength in TiO_2 lattice (Hoseini et al., 2017). This was justified by the increasing trend of photodegradation performance from 53.96% (0.0128 min^{-1}) of 1HPC to 67.31% (0.0187 min^{-1}) of 3HPC. However, the photodegradation performance dived to 36.45% beyond that with a low rate constant of 0.0073 min^{-1}. This might be due to the high amount of CDs adhering to TiO_2 blocking the visible light from reaching to TiO_2 and reduced the light-exposed surface area of TiO_2. Therefore, it can be concluded that photodegradation performance highly depended on the optical absorption capability and the light-exposed surface area of TiO_2 (Hoseini et al., 2017). The increment of CDs loading resulted in two conflicting outcomes, where higher CDs content improved the optical absorption capability but reduced the light-exposed surface area of TiO_2. Hence, the photodegradation ability of hybrid photocatalysts was determined by the dominant factor. As discussed, the best performing hybrid photocatalysts was 3HPC and thus it was selected as the photocatalyst to be grafted on bare PES membrane in the later section.

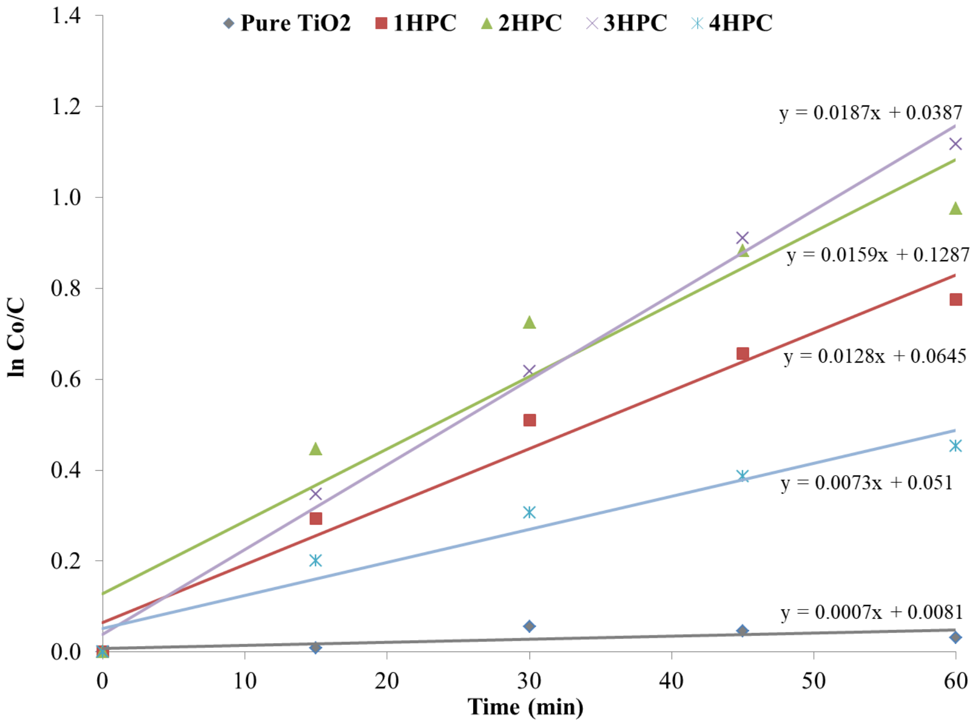

Figure 4.5: Photocatalytic Kinetics of Pure TiO_2 and Hybrid Photocatalysts on Degrading 10 ppm Paracetamol under Visible Light Irradiation by 100 W LED Lamp.

Table 4.3: Photodegradation Performances and Rate Constant of Pure TiO_2 and Hybrid Photocatalysts.

Sample	**Paracetamol Photodegradation at 60 min (%)**	**Rate Constant (min^{-1})**
Pure TiO_2	3.14	0.0007
1HPC	53.96	0.0128
2HPC	62.30	0.0159
3HPC	67.31	0.0187
4HPC	36.45	0.0073

4.3 Characterization of Membrane

4.3.1 Fourier-Transform Infrared (FTIR) Spectroscopy Analysis

FTIR analysis was carried out to identify the functional groups and interactions between PES polymer and the synthesized photocatalysts on the synthesized 1.0PESBM and photocatalytic membranes. Figure 4.6 illustrates the FTIR spectrums obtained for the membrane samples between the wavenumber of 400 – 3400 cm^{-1}. Based on Figure 4.6, the 1.0PESBM spectrum obtained was in agreement with the PES membrane peaks from the study by Rajis et al. (2019). The FTIR spectrums showed similar prominent peaks at the range 1577 cm^{-1} to 554 cm^{-1}, and a relatively weaker peak at 3097 cm^{-1}. Besides, all the photocatalytic membranes showed the similar signature peaks as 1.0PESBM, indicating that the polymer structure of PES membrane was not disrupted by the incorporation of 3HPC nanoparticles (Kuvarega et al., 2018).

Strong peaks at 1577 cm^{-1} and 1484 cm^{-1} revealed the C=C bond of aromatic ring (Geng et al., 2017). The peaks at 1237 cm^{-1} and 1104 cm^{-1} were associated with the C-O-C bond and C-O bond from ether group respectively (Hosseini et al., 2018). Meanwhile, O=S=O bond from the PES polymer as well as from potassium persulfate in the chemical grafting process was shown at 1148 cm^{-1}. Hydroxyl group can be observed at 3097 cm^{-1}. Peaks at 1405 cm^{-1}, 1320 cm^{-1} and 700 cm^{-1} indicated the out of phase stretch of CH_3, SO_2 and C-S-C bonds respectively (Kuvarega et al., 2018). According to Kuvarega et al. (2018), peaks at 1297 cm^{-1} and 1011 cm^{-1} were attributed by the C-O-C in and out of phase stretch from aryl ether groups, while peaks at 871 cm^{-1} and 834 cm^{-1} were contributed by the para-substituted adjacent H shifting from aromatic group. C-H bond in aromatic ring was represented by the peak at 717 cm^{-1}. Lastly, 554 cm^{-1} represented the scissors deformation of SO_2 (Kuvarega et al., 2018).

However, major TiO_2 peaks were absent in the FTIR spectrums of photocatalytic membranes mainly due to the rather small amount of photocatalyst nanoparticles (0.05 g, 0.10 g and 0.15g) that were incorporated to the membrane surface. Besides, as PAA was used as the monomer to increase the carboxylic acid group (COOH) on the surface of membrane for better attachment of photocatalytic nanoparticles, the carboxyl group at 1700 cm^{-1} shall be observed as presented by the study conducted by Qian et al. (2016). Unfortunately, COOH bond at 1700 cm^{-1} was not observed in the FTIR spectrums for photocatalytic membranes obtained. This may be due to the lack of the step to pre-treat the bare membrane with plasma as suggested by Qian et al. (2016). This is because the pre-treatment with plasma is able to induce necessary functional groups to the surface of bare membrane as well as generating highly active alkyl radicals which would react with O_2 and H_2O molecules from ambient air to generate stable carboxylic group (Qian et al., 2016). Hence, the absence of plasma pre-treatment on bare PES membrane resulted in the absence of carboxyl band in FTIR spectrums.

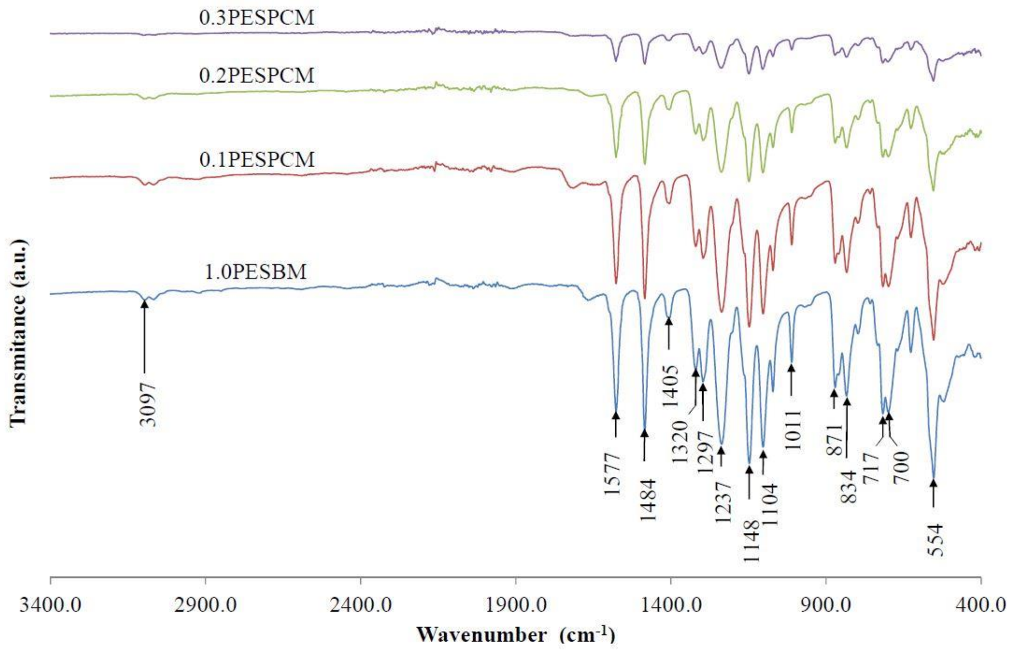

Figure 4.6: FTIR Spectrums of 1.0PESBM, 0.1PESPCM, 0.2PESPCM and 0.3PESPCM.

4.3.2 Scanning Electron Microscopy (SEM) Analysis

In order to visualize the surface morphology, surface topography and geometry of pore, as well as to estimate the pore size distribution and porosity, SEM analysis was carried out on all the fabricated membranes. Figure 4.7 displayed the cross sectional SEM images of 0.5PESBM and 1.0PESBM at magnification of ×500 and ×2,000. The SEM images displayed the highly porous finger-like macrovoids throughout the membrane cross section. This structure is highly favourable as higher flux of membrane will be able to be achieved due to the high porosity and low tortuosity of pores, which enable more fluid flow across membrane easily. The highly porous finger-like macrovoids structure was mainly due to the use of low polymer concentration

(17 wt%) which contributed to the low viscosity of casting solution and thus resulting in the rapid phase inversion process with instantaneous phase separation to form the finger-like macrovoids structure (Geng et al., 2017). Besides, the highly porous structure was also attributed by the use of NMP solvent which has high solubility parameter and thus able to dissolve PES polymer for rapid precipitation during phase inversion.

Furthermore, the Loeb-Sourirajan asymmetric membrane structure was observed in both 0.5PESBM and 1.0PESBM as presented in Figure 4.7 (b) and Figure 4.7 (d) respectively, which showed an ultrathin selective skin at the top and microporous support at the bottom region. This structure showed that the synthesized PES membrane was able to achieve high separation via the smaller surface pore size without compromising the membrane permeability since the resistance of the transport of permeate is negligible due to the highly porous support (Jiang, 2016).

In addition, the pore size of 1.0PESBM was significantly larger than that of 0.5PESBM as shown in Figure 4.7. This result revealed that the pore size and porosity of membrane increased when concentration of PVP in casting solution increased. This is because PVP is a pore-forming reagent due to its excellent hydrophilicity and water solubility (Junaidi et al., 2019). High PVP concentration led to the greater exchange rate between solvent and non-solvent during phase inversion process, thus increased the porosity and membrane pore size (Sun and Chen, 2016). Besides, owing to the instantaneous demixing mechanism of PVP, the increase in PVP concentration also led to the formation of macrovoids in the membrane matrix (Sun and Chen, 2016). Hence, the 1.0PESBM with higher PVP concentration exhibited a greater pore size of membrane.

Moreover, the plane view (magnification: ×100) and cross sectional SEM images (magnification: ×500) of photocatalytic membranes were presented in Figure 4.8 and Figure 4.9 respectively. The surface topography of PES membrane and photocatalytic membranes were compared in Figure 4.8. 1.0PESBM displayed a smooth and even surface topography. In contrast, the photocatalytic membranes displayed rather rough surfaces with abundance of nanoparticles, indicating the successful immobilization of 3HPC nanoparticles on the surface of PES membrane. As observed, 3HPC nanoparticles were evenly distributed throughout the surface of membrane, indicating that PAA was also evenly deposited on the membrane surface. Since the synthesized nanoparticles consisted of non-uniform particle size as discussed in SEM analysis of powdered photocatalyst reported in Section 4.1.4, the non-uniform particle size distribution can also be observed on the surface SEM images of composite membranes. As the amount of nanoparticles increased, aggregation of nanoparticles was observed on the surface of 0.2PESPCM and 0.3PESPCM, thus forming a highly dense and continuous surface layer (Qian et al., 2016).

Lastly, the cross-sections of photocatalytic membranes as shown in Figure 4.9 revealed that the 3HPC nanoparticles were well-adhered on the surfaces of membranes only but not within the pores. Small amount of nanoparticles were found in the membrane matrix due to the fall-out of nanoparticles from the membrane surface to the cross section of membrane during the breaking process by using liquid nitrogen.

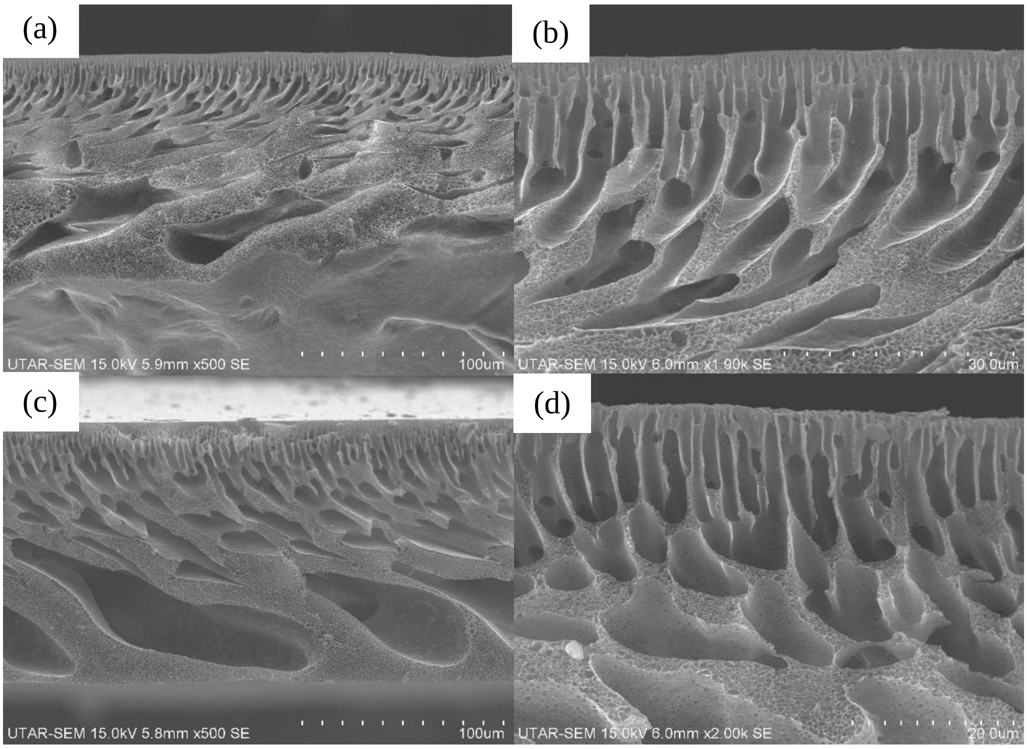

Figure 4.7: Cross Sectional SEM Images of (a) 0.5PESBM at Magnification ×500, (b) 0.5PESBM at Magnification ×2,000, (c) 1.0PESBM at Magnification ×500 and (d) 1.0PESBM at Magnification ×2,000.

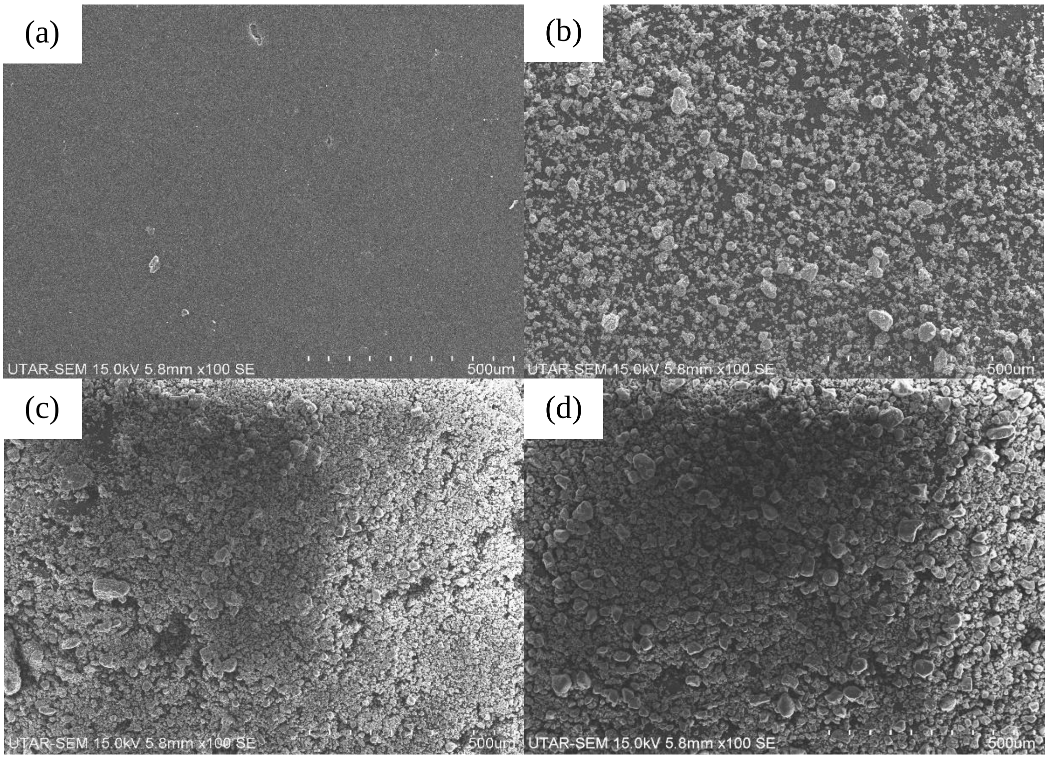

Figure 4.8: Surface SEM Images of (a) 1.0PESBM, (b) 0.1PESPCM, (c) 0.2PESPCM and (d) 0.3PESPCM at Magnification ×100.

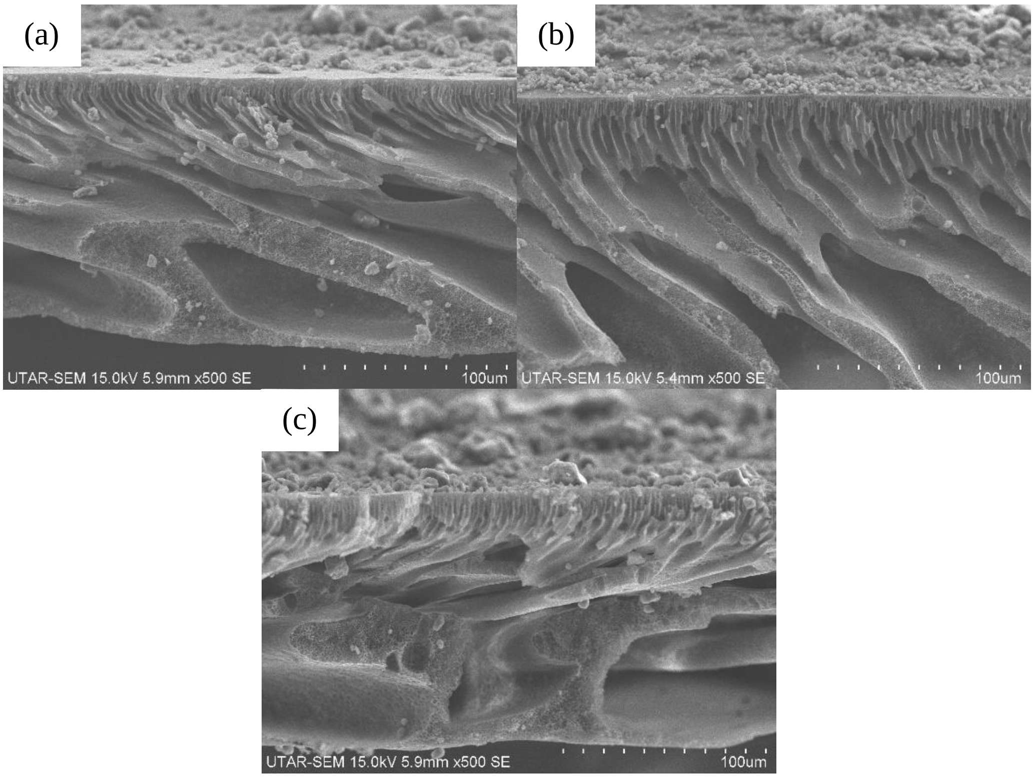

Figure 4.9: Cross Sectional SEM Images of (a) 0.1PESPCM, (b) 0.2PESPCM and (c) 0.3PESPCM at Magnification ×500.

4.3.3 Mass Gain and Grafting Yield

The best performing photocatalytic nanoparticles (3HPC) were grafted on 1.0PESBM with loading of 0.05 g, 0.10 g and 0.15 g. Prior to the photodegradation of paracetamol by using photocatalytic membranes, the mass gain (*M*) and grafting yield (*G*) of these photocatalytic membranes were calculated by using Equation 3.2 and Equation 3.3 respectively, and the detailed calculations were attached in Appendix E. Table 4.4 summarizes the results of mass gain and grafting yield calculations for the prepared photocatalytic membranes.

Table 4.4: Mass Gain and Grafting Yield of the Photocatalytic Membranes.

Samples	**Mass Gain, *M* (%)**	**Grafting Yield, *G* (%)**
0.1PESPCM	23.21	26.00
0.2PESPCM	25.86	15.00
0.3PESPCM	40.00	14.67

Based on Table 4.4, the mass gain calculated for the membranes increased as the 3HPC loading increased, indicating that the higher the photocatalytic nanoparticles concentration in the dipping solution, the higher the amount of nanoparticles that were successfully adhered to the membrane surface. This result was in good agreement with the findings by SEM analysis reported in Section 4.3.2.

However, despite the increasing photocatalytic nanoparticles concentration in the dipping solution, the grafting yield of photocatalytic membranes decreased. This scenario might be explained as the nanoparticles reached the saturation point, given that the surface area of bare membrane (14.6 cm^2) and the amount of PAA attached to the membrane were the same for all the three grafting samples.

4.4 Performance of Membrane

4.4.1 Membrane Pure Water Flux and Permeability

The permeability of the pure PES membranes and photocatalytic membranes were determined by conducting pure water flux (PWF) analysis using dead-end filtration cell at transmembrane pressure (TMP) of 2 bar and surrounding temperature of 25 ºC. The detailed calculations of PWF and permeability were attached in Appendix F. Figure 4.10 displays the average permeability of pure PES membranes, while Figure 4.11 presents the average permeability of the photocatalytic membranes.

As observed in Figure 4.10, as the PVP loading increased from 0.5 wt% to 1.0 wt%, the permeability of 1.0PESBM (135.21 ± 9.96 L/m^{2}h·bar) was twice of the 0.5PESBM (66.89 ± 12.40 L/m^{2}h·bar). The increasing trend of permeability was in good agreement with the study conducted by Junaidi et al. (2019). Hosseini et al. (2018) listed three factors that affect permeability of membrane to be the pore size, porosity and the hydrophilicity of membrane. The additive PVP plays a vital role in affecting the permeability of membrane as the concentration of PVP in casting solution directly influenced the pore size, porosity and hydrophilicity of membrane (Junaidi et al., 2019).

As discussed in the SEM analysis of the pure PES membranes in Section 4.3.2, the pore size and porosity of membrane increased with the increment of PVP concentration in casting solution. Owing to the higher porosity of 1.0PESBM, the resistance to transport of permeate across membrane thickness was lower, thus resulted in the higher membrane permeability.

Besides, high PVP concentration also greatly improved the hydrophilicity of PES membrane as reported by Abdel-Karim et al. (2017). Due to the lack of oxygen functional groups, PES membrane tends to be less hydrophilic compared to other polymeric membranes. However, the PES membrane’s hydrophilicity was greatly improved with the use of PVP additive as PVP is a highly hydrophilic polymer. Thus, the hydrophilicity of PVP in membrane matrix significantly increased the interaction between membrane pore walls and water molecules, which further increased the membrane permeability (Xu et al., 2019). Since 1.0PESBM possessed better permeability, it was chosen as the membrane used to incorporate photocatalyst nanoparticles.

The average permeability of the photocatalytic membranes were shown in Figure 4.11, where the average permeability of 0.1PESPCM, 0.2PESPCM and 0.3PESPCM were 0.87 ± 0.03 L/m^{2}h·bar, 0.73 ± 0.03 L/m^{2}h·bar and 0.65

± 0.03 L/m^{2}h·bar respectively. This indicated that the permeability dropped as the amount of 3HPC deposited on membrane surface increased. This behavior was similar to the findings by You et al. (2012) who reported that the flux of photocatalytic membrane decreased with the increment of TiO_2 loading despite the increasing hydrophilicity. The possible explanation for this phenomenon was that the surface pores were plugged by increasing amount of deposited nanoparticles (You et al., 2012). Similarly, Rahimpour et al. (2012) also reported that the PWF of the composite membrane reduced with the increasing deposition of TiO_2 due to the plugging of membrane pores by the deposited TiO_2. However, the differences in permeability of the photocatalytic membranes with different photocatalytic nanoparticles loading were small (<0.15 L/m^{2}h·bar), thus the effect of increasing photocatalytic nanoparticles loading was relatively insignificant to the reduction of permeability.

On the contrary, notice that permeability of membrane dropped over 99% after grafting of photocatalytic nanoparticles (from 135.21 L/m^{2}h·bar to ≤0.87 L/m^{2}h·bar). The drastic plunge of permeability was possibly influenced by the formation of PAA gel network on membrane surface from PAA grafting process. The PAA gel network was capable to alter the membrane morphology where the porosity and pore size were reduced, which further hindered the water permeation (Madaeni, Zinadini and Vatanpour, 2011). However, this finding was in disagreement with the study conducted by Qian et al. (2016), which suggested that the permeability of nanoparticles-incorporated membranes shall not be reduced due to the presence of a variety of water-soluble functional groups found on PAA and CDs such as hydroxyl group and carboxyl group. These water-soluble functional groups greatly increased the hydrophilicity of photocatalytic membranes and thus facilitated the water transport across membrane. This suggested that the effect of reduction in surface pore size due to the formation of PAA gel network was dominant over the presence of hydrophilic functional groups, which resulted in an overall plunge of permeability. As a solution to enhance the poor permeability for photocatalytic membranes, Madaeni, Zinadini and Vatanpour (2011) suggested to lower the ratio of cross-linker (EG) to monomer (PAA) to increase the amount of free -COOH groups so that higher hydrophilicity of membrane can be achieved. Besides, You et al. (2012) recommended that a thin layer of PAA should be grafted to minimize the alteration of membrane morphology.

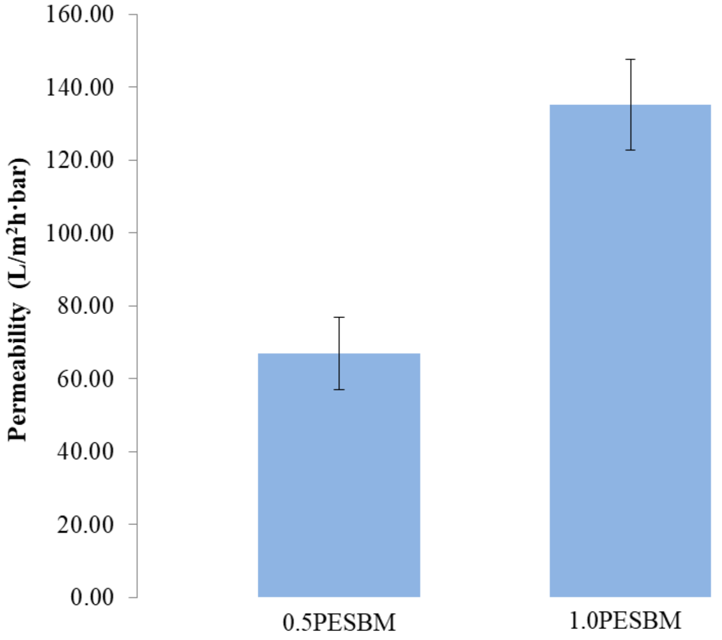

Figure 4.10: Permeability of Pure PES Membranes.

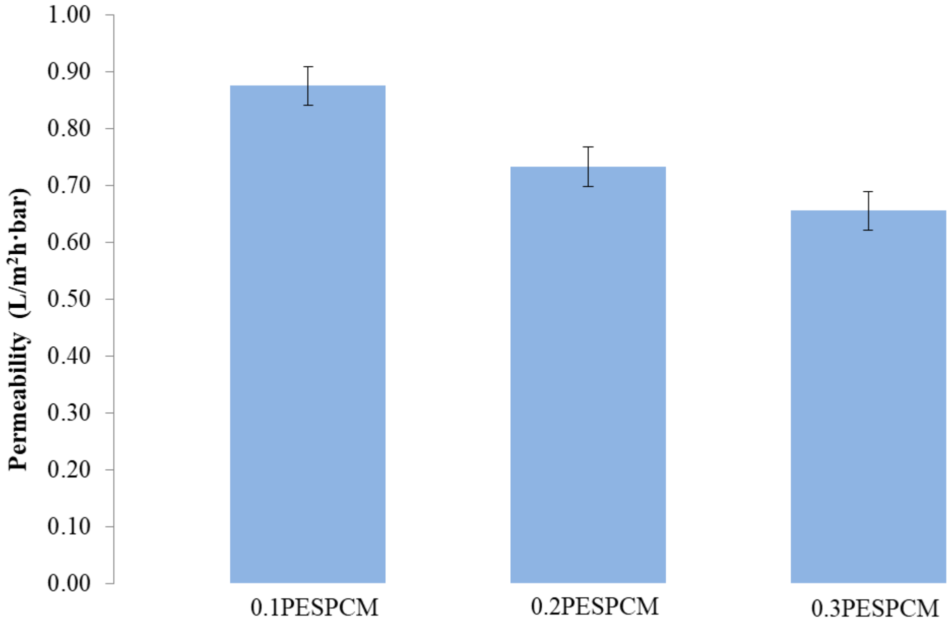

Figure 4.11: Permeability of Photocatalytic Membranes.

4.4.2 Photocatalytic Activity under Visible Light

The photodegradation of 4 ppm paracetamol was tested on 1.0PESBM and the photocatalytic membranes under visible light irradiation by using 100 W LED lamp. The UV-visible spectrophotometer results were recorded and the paracetamol removal percentage was calculated by using Equation 3.4 and detailed calculations were attached in Appendix C. Figure 4.12 illustrates the graph of $\ln(C_o/C) = kt$ for 1.0PESBM and the photocatalytic membranes based on the calculations attached in Appendix D. Meanwhile, Table 4.5 summarizes the photocatalytic performances and rate constants of 1.0PESBM and the photocatalytic membranes. Note that the photocatalyst particles remained visible on the PES membrane surface after the adsorption and photodegradation test was conducted for a total of 210 minutes, indicating that the photocatalyst nanoparticles were well-deposited on the membrane surface.

1.0PESBM was used as a controlled variable for the photodegradation of paracetamol. As presented in Figure 4.12, 1.0PESBM showed negligible contribution for paracetamol removal. The extremely small percent of bare PES paracetamol removal of 0.98% with a rate constant of 0.00004 min^{-1} might due to the small measurement deviation by UV-visible spectrophotometer and thus 1.0PESBM was assumed to have no photodegradation capability on paracetamol. This proved that the removal of paracetamol by using hybrid membranes was predominantly attributed to the grafted photocatalyst nanoparticles (3HPC).

Theoretically, high amount of 3HPC loaded to the surface of PES membrane gives a better photodegradation performance as reported by You et al. (2012). This theory was justified as the paracetamol removal percentages of photocatalytic membranes increased with the increment of photocatalyst nanoparticles loading, where the highest removal percent achieved 41.62% for 0.3PESPCM.

Notice that the photocatalytic capabilities of photocatalytic membranes were much lower than the photocatalytic capabilities of powdered photocatalysts, as the best performing powdered photocatalyst (3HPC) was able to achieve photocatalytic rate of 0.0187 min^{-1}, while the best performing photocatalyic membrane (0.3PESPCM) only achieved 0.0028 min^{-1}

photocatalytic rate. The major factor that caused the drop of photocatalytic performance was due to the lower photocatalyst load in photocatalytic membrane. As calculated in Appendix E, the actual masses of 3HPC that were deposited on 0.1PESPCM, 0.2PESPCM and 0.3PESPCM were merely 0.013 g, 0.015 g and 0.022 g respectively. These loadings were much lower than the 0.05 g powdered photocatalysts used for the degradation of paracetamol. In addition, mass transfer limitation as well as the reduced surface area of photocatalysts also largely contributed to the reduction in photocatalytic performances of photocatalytic membranes. This is because approximately half of the exposed surface area was attached to the membrane surface, thus the covered surface of photocatalysts was ineffective for photocatalysis to occur. Despite the lower photocatalytic performance of photocatalytic membrane, the photocatalytic membrane was able to degrade paracetamol efficiently considering that fact that the actual concentration of paracetamol in environmental water sources is extremely low (approximately 0.07 μg/L or 7×10^{-5} ppm) (Al-Odaini et al., 2010).

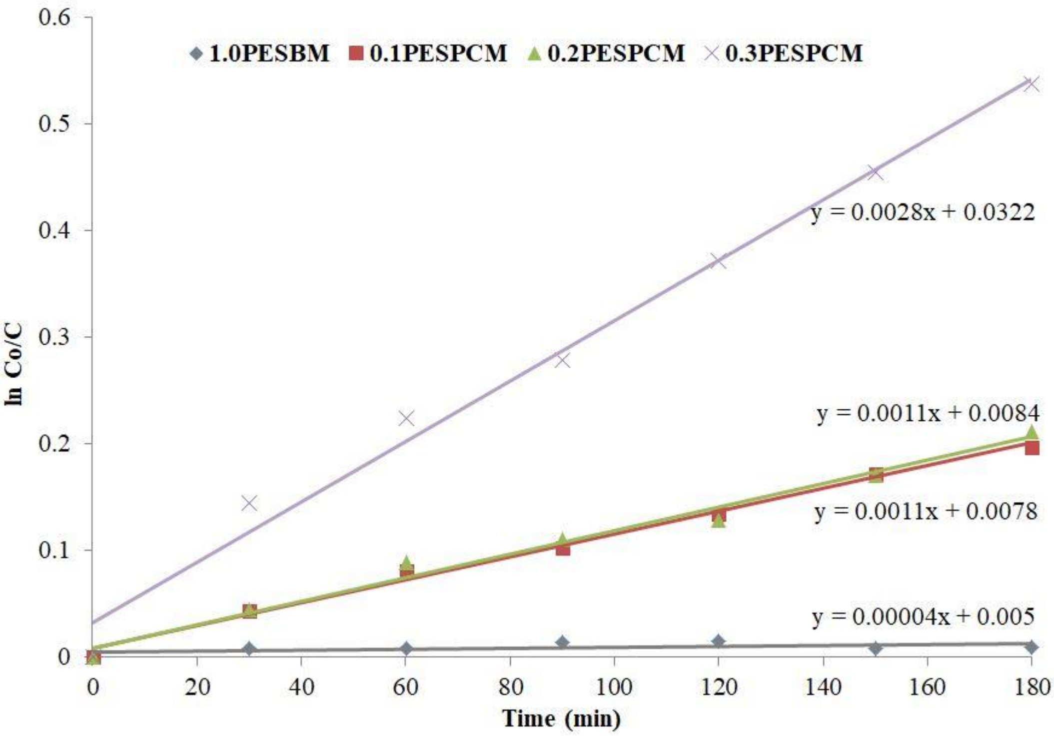

Figure 4.12: Photocatalytic Kinetics of 1.0PESBM and the Photocatalytic Membranes on Degrading 4 ppm Paracetamol under Visible Light Irradiation by 100 W LED Lamp.

Table 4.5: Photodegradation Performances and Rate Constant of 1.0PESBM and the Photocatalytic Membranes.

Sample	**Paracetamol Photodegradation at 180 min (%)**	**Rate Constant (min^{-1})**
1.0PESBM	0.98	0.00004
0.1PESPCM	17.84	0.0011
0.2PESPCM	19.08	0.0011
0.3PESPCM	41.62	0.0028

CHAPTER 5

CONCLUSIONS AND RECOMMENDATIONS

5.1 Conclusions

In conclusion, all the objectives of this research were achieved. The hybrid N-CDs/TiO_2 photocatalysts were synthesized and characterized. The photocatalytic membranes were successfully fabricated and the performances of membranes in terms of photocatalytic degradation of paracetamol and permeability were tested.

In terms of the characterization of hybrid photocatalysts, the XRD profiles justified the formation of anatase phase TiO_2. The incorporation of N-CDs to TiO_2 was proven to reduce the aggregation of TiO_2 nanoparticles as the crystallite sizes of hybrid photocatalysts were smaller than that of pure TiO_2. The reduction in particles sizes of hybrid photocatalysts was also proven by the SEM images obtained where the synthesized photocatalysts revealed rough and uneven surface morphology. Meanwhile, EDX analysis justified the formation of hybrid photocatalyst, where atomic percent of carbon and nitrogen were increased in hybrid photocatalyst. This indicated the successful incorporation of N-CDs on TiO_2. The FTIR spectrums of powdered photocatalysts showed that the water soluble hydroxyl functional group (-OH) increased with the increment of N-CDs incorporated to TiO_2, indicating that the hydrophilicity of hybrid photocatalsts increased as well. Furthermore, the electronegativities of TiO_2 and hybrid photocatalysts were determined by conducting the zeta potential analysis. The adsorption of paracetamol compounds on the hybrid photocatalyts was best in neutral media as the increment of pH would alter the surface charge of paracetamol to negative value, thus leading to the repulsion between paracetamol of the negatively charged photocatalyst.

From the photocatalytic degradation of paracetamol study, hybrid photocatalysts had successfully lowered the band gap energy of pure TiO_2 to visible light region, where 3HPC exhibited the best photocatalytic activity with a rate constant of 0.0187 min^{-1}. From 1 mL to 3 mL of N-CDs loading, the incorporation of N-CDs to TiO_2 had enhanced the photocatalytic performance by improving the optical absorption capability of the photocatalyst. However, high loading of N-CDs beyond 3 mL revealed a drop of performance as the high loading of N-CDs blocked the TiO_2 from the irradiating light which further hindered the photocatalyst's performance.

The fabricated photocatalytic membranes were characterized by using SEM analysis, where the cross sections images indicated the synthesized PES membranes were in asymmetric structure. Based on the cross sectional views, PES membrane with higher PVP concentration (1 wt%) showed the larger pore size than 0.5 wt%, justifying that high PVP concentration increased the instantaneous demixing between solvent and non-solvent during phase inversion process, thus leading to greater membrane pore size and porosity. Meanwhile, SEM images of photocatalytic membranes revealed the successful attachment of 3HPC nanoparticles on the surface of membranes. This was also justified by the increase in mass gain with the increment of 3HPC loading.

The permeability of 1.0PESBM (135.21 $\text{L/m}^2\text{h·bar}$) was about twice of the 0.5PESBM (66.89 $\text{L/m}^2\text{h·bar}$) mainly due to its higher hydrophilicity and greater membrane pore size. In contrast, the permeability of the photocatalytic membranes plunged over 99% after chemical grafting with PAA monomer. The morphology of PES membrane was said to be altered by the PAA gel network which hindered the transport of permeate across membrane.

Last but not least, the photocatalytic degradation of paracetamol by photocatalytic membranes were carried out where 3.0PESPCM was found to be the best performing photocatalytic membrane with a rate constant of 0.0028 min^{-1}. Despite the lower photocatalytic performance of 3.0PESPCM compared to that of powdered 3HPC, photodegradation of paracetamol by using photocatalytic membrane was considered as a feasible method as the actual concentration of paracetamol in the environment water sources is very low. This study showed that the fabricated N-CDs/TiO_2 incorporated photocatalytic membrane has great potential in degrading paracetamol compound in wastewater.

5.2 Recommendations for future work

Although the hybrid N-CDs/TiO_2 photocatalyst and photocatalytic membrane in this study showed excellent photocatalytic degradation of paracetamol under visible light irradiation, the permeability of photocatalytic membrane was underwhelming due to the pore size reduction by the grafting of PAA monomer. Therefore, it is recommended to reduce the ratio of EG:PAA in order to induce more –COOH groups to the membrane surface. This will increase the hydrophilicity of membrane and thus leading to higher membrane permeability. Moreover, a thinner layer of PAA can be grafted on the membrane surface so that the negative effects of PAA on the morphology of membrane can be minimized (You et al., 2012).

Furthermore, prior to chemical grafting of PAA monomer, it is recommended to pre-treat the bare membrane with plasma treatment to induce necessary highly alkyl radicals which will react with O_2 and H_2O from ambient air to form stable carboxylic groups for better attachment of photocatalyst nanoparticles (Qian et al., 2016; You et al., 2012). Lastly, since the hybrid N-CDs/TiO_2 photocatalyst showed outstanding photocatalytic performance on degradation of paracetamol under visible light, it is recommended to investigate the photodegradation performance of this hybrid photocatalyst on other pharmaceutical wastes. Also, the potential of these photocatalytic membranes in crossflow filtration system should be further investigated.

REFERENCES

Abdel-Karim, A., Gad-Allah, T.A., El-Kalliny, A.S., Ahmed, S.I.A., Souaya, E.R., Badawy, M.I. and Ulbricht, M., 2017. Fabrication of modified polyethersulfone membranes for wastewater treatment by submerged membrane bioreactor. *Separation and Purification Technology*, 175, pp.36–46.

Abdullah, M., Abidin, Z.Z., Sobri, S., Rashid, S., Mahdi, M.A., Ibrahim, N.A. and Yahaya, M., 2019. Fabrication, characterization and response surface method optimization for quantum efficiency of fluorescent nitrogen-doped carbon dots from carboxymethylcellulose derived from empty fruit bunch of oil palms. *Chinese Journal of Chemical Engineering*.

Abdullah, N. and Sulaiman, F., 2013. The Oil Palm Wastes in Malaysia. *Biomass Now - Sustainable Growth and Use*, p.13.

Ahmadi, M., Ramezani Motlagh, H., Jaafarzadeh, N., Mostoufi, A., Saeedi, R., Barzegar, G. and Jorfi, S., 2017. Enhanced photocatalytic degradation of tetracycline and real pharmaceutical wastewater using MWCNT/TiO2 nano-composite. *Journal of Environmental Management*, 186, pp.55–63.

Al-Kaf, A., Naji, K.M., Yusuf, Q., Abdullah, M. and Edrees, W., 2017. Occurrence of Paracetamol in Aquatic Environments and Transformation by Microorganisms: A Review. *Chronicles of Pharmaceutical Science*, pp.341–355.

Al-Malek, S.A., Abu Seman, M.N., Johnson, D. and Hilal, N., 2012. Formation and characterization of polyethersulfone membranes using different concentrations of polyvinylpyrrolidone. *Desalination*, 288, pp.31–39.

Al-Odaini, N.A., Zakaria, M.P., Yaziz, M.I. and Surif, S., 2010. Multi-residue analytical method for human pharmaceuticals and synthetic hormones in river water and sewage effluents by solid-phase extraction and liquid chromatography–tandem mass spectrometry. *Journal of Chromatography A*, 1217(44), pp.6791–6806.

Argurio, P., Fontananova, E., Molinari, R. and Drioli, E., 2018. Photocatalytic membranes in photocatalytic membrane reactors. *Processes*, 6(9).

Athanasekou, C.P., Romanos, G.E., Katsaros, F.K., Kordatos, K., Likodimos, V. and Falaras, P., 2012. Very efficient composite titania membranes in hybrid ultrafiltration/photocatalysis water treatment processes. *Journal of Membrane Science*, 392–393, pp.192–203.

Bagheri, S., Shameli, K. and Abd Hamid, S.B., 2013. Synthesis and characterization of anatase titanium dioxide nanoparticles using egg white solution via Sol-Gel method. *Journal of Chemistry*, 2013.

Bernal, V., Erto, A., Giraldo, L. and Moreno-Piraján, J.C., 2017. Effect of solution pH on the adsorption of paracetamol on chemically modified activated carbons. *Molecules*, 22(7), pp.1–14.

Bet-Moushoul, E., Mansourpanah, Y., Farhadi, K. and Tabatabaei, M., 2016. TiO2 nanocomposite based polymeric membranes: A review on performance improvement for various applications in chemical engineering processes. *Chemical Engineering Journal*, 283, pp.29–46.

Chu, K.-W., Lee, S.L., Chang, C.-J. and Liu, L., 2019. Recent Progress of Carbon Dot Precursors and Photocatalysis Applications. *Polymers*, 11(4), p.689.

Cong, S. and Zhao, Z.G., 2017. Carbon Quantum Dots: A Component of Efficient Visible Light Catalysts. *Visible-Light Photocatalysis of Carbon-Based Materials*, pp.47–66.

Dalgic, G., Turkdogan, I., Yetilmezsoy, K. and Kocak, E., 2017. Treatment of real paracetamol wastewater by fenton process. *Chemical Industry and Chemical Engineering Quarterly*, 23(2), pp.177–186.

Davis, R. and Mauer, L., 2010. Fourier transform infrared (FT-IR) spectroscopy: a rapid tool for detection and analysis of foodborne pathogenic bacteria. *Current Research, Technology and Education Topics in Applied Microbiology and Microbial Biotechnology. A. Méndez-Vilas (Ed.)*, (1), pp.1582–1594.

Dungani, R., Aditiawati, P., Aprilia, S., Yuniarti, K., Karliati, T., Suwandhi, I. and Sumardi, I., 2018. Biomaterial from Oil Palm Waste: Properties, Characterization and Applications. In: *Palm Oil*. InTech.

Fan, Q., Huang, Y., Zhang, C., Liu, J., Piao, L., Yu, Y., Zuo, S. and Li, B., 2016. Superior nanoporous graphitic carbon nitride photocatalyst coupled with CdS quantum dots for photodegradation of RhB. *Catalysis Today*, 264, pp.250–256.

Fischer, K., Grimm, M., Meyers, J., Dietrich, C., Gläser, R. and Schulze, A., 2015. Photoactive microfiltration membranes via directed synthesis of TiO 2 nanoparticles on the polymer surface for removal of drugs from water. *Journal of Membrane Science*, 478, pp.49–57.

Gedda, G., Lee, C.Y., Lin, Y.C. and Wu, H.F., 2016. Green synthesis of carbon dots from prawn shells for highly selective and sensitive detection of copper ions. *Sensors and Actuators, B: Chemical*, 224, pp.396–403.

Geibler, D., Gollwitzer, C., Sikora, A., Minelli, C., Krumrey, M. and Resch-Genger, U., 2015. Effect of fluorescent staining on size measurements of polymeric nanoparticles using DLS and SAXS. *Analytical Methods*, 7(23), pp.9785–9790.

Geng, Z., Yang, X., Boo, C., Zhu, S., Lu, Y., Fan, W., Huo, M., Elimelech, M. and Yang, X., 2017. Self-cleaning anti-fouling hybrid ultrafiltration membranes via side chain grafting of poly(aryl ether sulfone) and titanium dioxide. *Journal of Membrane Science*, 529, pp.1–10.

Gnanaprakasam, A., Sivakumar, V.M. and Thirumarimurugan, M., 2015. Influencing Parameters in the Photocatalytic Degradation of Organic Effluent via Nanometal Oxide Catalyst: A Review. *Indian Journal of Materials Science*, pp.1–16.

Hoseini, S.N., Pirzaman, A.K., Aroon, M.A. and Pirbazari, A.E., 2017. Photocatalytic degradation of 2,4-dichlorophenol by Co-doped TiO2 (Co/TiO2) nanoparticles and Co/TiO2 containing mixed matrix membranes. *Journal of Water Process Engineering*, 17, pp.124–134.

Hosseini, S.S., Fakharian Torbati, S., Alaei Shahmirzadi, M.A. and Tavangar, T., 2018. Fabrication, characterization, and performance evaluation of polyethersulfone/TiO2 nanocomposite ultrafiltration membranes for produced water treatment. *Polymers for Advanced Technologies*, 29(10), pp.2619–2631.

Huo, P., Guan, J., Zhou, M., Ma, C., Liu, X., Yan, Y. and Yuan, S., 2017. Carbon quantum dots modified CdSe loaded reduced graphene oxide for enhancing photocatalytic activity. *Journal of Industrial and Engineering Chemistry*, 50, pp.147–154.

Jallouli, N., Elghniji, K., Trabelsi, H. and Ksibi, M., 2017. Photocatalytic degradation of paracetamol on TiO2 nanoparticles and TiO2/cellulosic fiber under UV and sunlight irradiation. *Arabian Journal of Chemistry*, 10, pp.S3640–S3645.

Jamaludin, N., Andul, S. and Tan, T., 2018. Extraction of Carbon Dots from Empty Fruit Bunch Biochar via an Acid- Free Hydrothermal Method, pp.15–16.

Jelinek, R., 2017. Carbon quantum dots. *Carbon quantum dots. Springer International Publishing, Cham*, pp.29-46.

Jhonsi, M.A., 2018. Carbon quantum dots for bioimaging. *State of the Art in Nano-bioimaging. IntechOpen, London*, pp.35-53.

Jiang, L.Y., 2016. *Asymmetric Membrane*. *Encyclopedia of Membranes*.

Junaidi, N.F.D., Othman, N.H., Shahruddin, M.Z., Alias, N.H., Lau, W.J. and Ismail, A.F., 2019. Effect of graphene oxide (GO) and polyvinylpyrollidone (PVP) additives on the hydrophilicity of composite polyethersulfone (PES) membrane. *Malaysia Journal of Fundamental and Applied Sciences*, 15(3), pp.361–366.

Kanakaraju, D., Glass, B.D. and Oelgemöller, M., 2014. Titanium dioxide photocatalysis for pharmaceutical wastewater treatment. *Environmental Chemistry Letters*, 12(1), pp.27–47.

Kassim Shaari, N.Z., Abd Rahman, N., Sulaiman, N.A. and Mohd Tajuddin, R., 2017. Thin Film Composite Membranes: Mechanical and Antifouling Properties. *MATEC Web of Conferences*, 103.

Kavitha, T. and Kumar, S., 2018. Turning date palm fronds into biocompatible mesoporous fluorescent carbon dots. *Scientific Reports*, 8(1), p.16269.

Khalil, H.P.S.A., Jawaid, M., Hassan, A., Paridah, M.T. and Zaidon, A., 2012. Oil palm biomass fibers and recent advancement in oil palm biomass fibers based hybrid biocomposites.

Khan, M.M., Adil, S.F. and Al-Mayouf, A., 2015. Metal oxides as photocatalysts. *Journal of Saudi Chemical Society*, 19(5), pp.462–464.

Krysmann, M.J., Kelarakis, A. and Giannelis, E.P., 2012. Photoluminescent carbogenic nanoparticles directly derived from crude biomass. *Green Chemistry*, 14(11), pp.3141–3145.

Kuvarega, A.T., Khumalo, N., Dlamini, D. and Mamba, B.B., 2018. Polysulfone/N,Pd co-doped TiO2 composite membranes for photocatalytic dye degradation. *Separation and Purification Technology*, 191, pp.122–133.

Kuvarega, A.T. and Mamba, B.B., 2016. Photocatalytic Membranes for Efficient Water Treatment. *Semiconductor Photocatalysis - Materials, Mechanisms and Applications*.

Lalia, B.S., Kochkodan, V., Hashaikeh, R. and Hilal, N., 2013. A review on membrane fabrication: Structure, properties and performance relationship. *Desalination*, 326, pp.77–95.

Leong, S., Razmjou, A., Wang, K., Hapgood, K., Zhang, X. and Wang, H., 2014. TiO2 based photocatalytic membranes: A review. *Journal of Membrane Science*, 472, pp.167–184.

Li, H., He, X., Kang, Z., Huang, H., Liu, Y., Liu, J., Lian, S., Tsang, C.H.A., Yang, X. and Lee, S.T., 2010. Water-soluble fluorescent carbon quantum dots and photocatalyst design. *Angewandte Chemie - International Edition*, 49(26), pp.4430–4434.

Lin, Y.-F., Tung, K.-L., Tzeng, Y.-S., Chen, J.-H. and Chang, K.-S., 2012. Rapid atmospheric plasma spray coating preparation and photocatalytic activity of macroporous titania nanocrystalline membranes. *Journal of Membrane Science*, 389, pp.83–90.

Liu, S., Tian, J., Wang, L., Zhang, Y., Qin, X., Luo, Y., Asiri, A.M., Al-Youbi, A.O. and Sun, X., 2012. Hydrothermal Treatment of Grass: A Low-Cost, Green Route to Nitrogen-Doped, Carbon-Rich, Photoluminescent Polymer Nanodots as an Effective Fluorescent Sensing Platform for Label-Free Detection of Cu(II) Ions. *Advanced Materials*, 24(15), pp.2037–2041.

Liu, T., Sun, S., Zhou, L., Li, P., Su, Z. and Wei, G., 2019. Polyurethane-supported graphene oxide foam functionalized with carbon dots and TiO2 Particles for photocatalytic degradation of dyes. *Applied Sciences (Switzerland)*, 9(2).

Liu, Y., Xiao, N., Gong, N., Wang, H., Shi, X., Gu, W. and Ye, L., 2014. One-step microwave-assisted polyol synthesis of green luminescent carbon dots as optical nanoprobes. *Carbon*, *68*, pp.258-264.

Liu, Y., Yu, Y.X. and Zhang, W. De, 2013. Carbon quantum dots-doped CdS microspheres with enhanced photocatalytic performance. *Journal of Alloys and Compounds*, 569, pp.102–110.

Madaeni, S.S., Zinadini, S. and Vatanpour, V., 2011. A new approach to improve antifouling property of PVDF membrane using in situ polymerization of PAA functionalized TiO2 nanoparticles. *Journal of Membrane Science*, 380(1–2), pp.155–162.

Mehta, A., Mishra, A., Kainth, S. and Basu, S., 2018. Carbon quantum dots/TiO2 nanocomposite for sensing of toxic metals and photodetoxification of dyes with kill waste by waste concept. *Materials and Design*, 155, pp.485–493.

Meng, W., Bai, X., Wang, B., Liu, Z., Lu, S. and Yang, B., 2019. Biomass-Derived Carbon Dots and Their Applications. *Energy & Environmental Materials*, 2(3), pp.172–192.

Mubarak, N.M., Sahu, J.N., Abdullah, E.C. and Jayakumar, N.S., 2016. Plam oil empty fruit bunch based magnetic biochar composite comparison for synthesis by microwave-assisted and conventional heating. *Journal of Analytical and Applied Pyrolysis*, 120, pp.521–528.

Mutalib, M.A., Rahman, M.A., Othman, M.H.D., Ismail, A.F. and Jaafar, J., 2017. Scanning electron microscopy (SEM) and energy-dispersive X-ray (EDX) spectroscopy. In *Membrane Characterization* (pp. 161-179). Elsevier.

Muthulingam, Bin Bae, K., Khan, R., Lee, I.-H. and Uthirakumar, P., 2016. Dramatic Daylight Induced Photocatalytic Performance of Carbon Quantum Dots Decorated N-doped ZnO with Suppressed Photocorrosion. *Physical Chemistry Chemical Physics*.

Oza, G., Oza, K., Pandey, S., Shinde, S., Mewada, A., Thakur, M., Sharon, M. and Sharon, M., 2015. A green route towards highly photoluminescent and cytocompatible carbon dot synthesis and its separation using sucrose density gradient centrifugation. *Journal of Fluorescence*, 25(1), pp.9–14.

Praveen, P., Viruthagiri, G., Mugundan, S. and Shanmugam, N., 2014. Structural, optical and morphological analyses of pristine titanium di-oxide nanoparticles - Synthesized via sol-gel route. *Spectrochimica Acta - Part A: Molecular and Biomolecular Spectroscopy*, 117, pp.622–629.

Purbia, R. and Paria, S., 2016. A simple turn on fluorescent sensor for the selective detection of thiamine using coconut water derived luminescent carbon dots. *Biosensors and Bioelectronics*, 79, pp.467–475.

Qian, Y., Chi, L., Zhou, W., Yu, Z., Zhang, Z., Zhang, Z. and Jiang, Z., 2016. Fabrication of TiO 2 -modified polytetrafluoroethylene ultrafiltration membranes via plasma-enhanced surface graft pretreatment. *Applied Surface Science*, 360, pp.749–757.

Rahimpour, A., Jahanshahi, M., Mollahosseini, A. and Rajaeian, B., 2012. Structural and performance properties of UV-assisted TiO 2 deposited nano-composite PVDF/SPES membranes. *Desalination*, 285, pp.31–38.

Rajis, Z., Azmi, N.F.A.N., Makhtar, S.N.N.M., Norddin, M.N.A.M. and Mustafa, A., 2019. Preparation, Characterization and Performances of Photocatalytic TiO2-Ag2O/PESf Membrane for Methylene Blue Removal. *Journal of Applied Membrane Science & Technology*, 23(2), pp.83–97.

Sahu, S., Behera, B., Maiti, T.K. and Mohapatra, S., 2012. Simple one-step synthesis of highly luminescent carbon dots from orange juice: Application as excellent bio-imaging agents. *Chemical Communications*, 48(70), pp.8835–8837.

Sang, Y., Zhao, Z., Tian, J., Hao, P., Jiang, H., Liu, H. and Claverie, J.P., 2014. Enhanced photocatalytic property of educed graphene oxide/TiO 2 nanobelt surface heterostructures constructed by an in situ photochemical reduction method. *Small*, 10(18), pp.3775–3782.

Saranya, R. and Nithyanandhi, M., 2017. Removal of Paracetamol from Pharmaceutical Wastewater by Integrated MBR. *Journal of Chemical and Pharmaceutical Sciences*, pp.114–118.

Sharma, S., Dutta, V., Singh, P., Raizada, P., Rahmani-Sani, A., Hosseini-Bandegharaei, A. and Thakur, V.K., 2019. Carbon quantum dot supported semiconductor photocatalysts for efficient degradation of organic pollutants in water: A review. *Journal of Cleaner Production*, 228, pp.755–769.

Shi, Y., Huang, J., Zeng, G., Cheng, W. and Hu, J., 2019. Photocatalytic membrane in water purification: is it stepping closer to be driven by visible light? *Journal of Membrane Science*, 584, pp.364–392.

Shockravi, A., Vatanpour, V., Najjar, Z., Bahadori, S. and Javadi, A., 2017. A new high performance polyamide as an effective additive for modification of antifouling properties and morphology of asymmetric PES blend ultrafiltration membranes. *Microporous and Mesoporous Materials*, 246, pp.24–36.

Sim, L.C., Yet, L.J., Leong, K.H., Chinb, Y.H. and Saravanan, P., 2019. One Pot Synthesis of Pineapple Juice Derived - Carbon Quantum Dots and TiO 2 Composite for Solar Light Active Photocatalysis. 8(2), pp.9–16.

Singh, I., Arora, R., Dhiman, H. and Pahwa, R., 2018. Carbon Quantum Dots : Synthesis , Characterization and Biomedical Applications Karbon Kuantum Noktaları : Sentez , Karakterizasyon ve Biyomedikal. 15(2), pp.219–230.

Song, P., Zhang, L., Long, H., Meng, M., Liu, T., Yin, Y. and Xi, R., 2017. A multianalyte fluorescent carbon dots sensing system constructed based on specific recognition of Fe(III) ions. *RSC Advances*, 7(46), pp.28637–28646.

Sun, Y., Zhou, B., Lin, Y., Wang, W., Fernando, K.A.S., Pathak, P., Meziani, M.J., Harruff, B.A., Wang, X., Wang, H., Luo, P.G., Yang, H., Kose, M.E., Chen, B., Veca, L.M., Xie, S. and Carolina, S., 2006. Quantum-Sized Carbon Dots for Bright and Colorful Photoluminescence. pp.7756–7757.

Sun, Z. and Chen, F., 2016. Hydrophilicity and antifouling property of membrane materials from cellulose acetate/polyethersulfone in DMAc. *International Journal of Biological Macromolecules*, 91, pp.143–150.

Tyagi, A., Tripathi, K.M., Singh, N., Choudhary, S. and Gupta, R.K., 2016. Green synthesis of carbon quantum dots from lemon peel waste: Applications in sensing and photocatalysis. *RSC Advances*, 6(76), pp.72423–72432.

Vaiano, V., Sacco, O., Sannino, D. and Ciambelli, P., 2015. Photocatalytic removal of spiramycin from wastewater under visible light with N-doped TiO2 photocatalysts. *Chemical Engineering Journal*, 261, pp.3–8.

Wang, H., Wei, Z., Matsui, H. and Zhou, S., 2014. Fe3O4/carbon quantum dots hybrid nanoflowers for highly active and recyclable visible-light driven photocatalyst. *Journal of Materials Chemistry A*, 2(38), pp.15740–15745.

Wang, J., Liu, G., Leung, K.C., Loffroy, R., Lu, P., J, Y.X. and Wang, Y.X.J., 2015. Opportunities and Challenges of Fluorescent Carbon Dots in Translational Optical Imaging.

Wang, N., Wang, Y., Guo, T., Yang, T., Chen, M. and Wang, J., 2016. Green preparation of carbon dots with papaya as carbon source for effective fluorescent sensing of Iron (III) and Escherichia coli. *Biosensors and Bioelectronics*, 85, pp.68–75.

Wang, Y. and Hu, A., 2014. Carbon quantum dots: synthesis, properties and applications. *Journal of Materials Chemistry C: Materials for optical and electronic devices*, 2, pp.6921–6939.

Wen, X., Yu, P., Toh, Y.-R., Ma, X. and Tang, J., 2014. On the upconversion fluorescence in carbon nanodots and graphene quantum dots. *Chem. Commun.*, 50(36), pp.4703–4706.

Xu, F., Wei, M., Zhang, X., Song, Y., Zhou, W. and Wang, Y., 2019. How Pore Hydrophilicity Influences Water Permeability? *Research*, 2019, pp.1–10.

Xu, X., Ray, R., Gu, Y., Ploehn, H.J., Gearheart, L., Raker, K. and Scrivens, W.A., 2004. Electrophoretic analysis and purification of fluorescent single-walled carbon nanotube fragments. *Journal of the American Chemical Society*, 126(40), pp.12736–12737.

Xue, M., Zhan, Z., Zou, M., Zhang, L. and Zhao, S., 2016. Green synthesis of stable and biocompatible fluorescent carbon dots from peanut shells for multicolor living cell imaging. *New Journal of Chemistry*, 40(2), pp.1698–1703.

Yan, Y., Kuang, W., Shi, L., Ye, X., Yang, Y., Xie, X., Shi, Q. and Tan, S., 2019. Carbon quantum dot-decorated TiO2 for fast and sustainable antibacterial properties under visible-light. *Journal of Alloys and Compounds*, 777, pp.234–243.

Yin, J. and Deng, B., 2015. Polymer-matrix nanocomposite membranes for water treatment. *Journal of Membrane Science*, 479, pp.256–275.

You, S.J., Semblante, G.U., Lu, S.C., Damodar, R.A. and Wei, T.C., 2012. Evaluation of the antifouling and photocatalytic properties of poly(vinylidene fluoride) plasma-grafted poly(acrylic acid) membrane with self-assembled TiO 2. *Journal of Hazardous Materials*, 237–238, pp.10–19.

Yu, C., Xuan, T., Chen, Y., Zhao, Z., Sun, Z. and Li, H., 2015. A facile, green synthesis of highly fluorescent carbon nanoparticles from oatmeal for cell imaging. *Journal of Materials Chemistry C*, 3(37), pp.9514–9518.

Zangeneh, H., Zinatizadeh, A.A., Zinadini, S., Feyzi, M. and Bahnemann, D.W., 2019. Preparation ultrafine L-Methionine (C,N,S triple doped)-TiO2-ZnO nanoparticles and their photocatalytic performance for fouling alleviation in PES nanocomposite membrane. *Composites Part B: Engineering*, 176, p.107158.

Zhang, J., Yuan, X., Jiang, L., Wu, Z., Chen, X., Wang, H., Wang, H. and Zeng, G., 2018. Highly efficient photocatalysis toward tetracycline of nitrogen doped carbon quantum dots sensitized bismuth tungstate based on interfacial charge transfer. *Journal of Colloid and Interface Science*, 511, pp.296–306.

Zhang, Q., Wang, H., Fan, X., Lv, F., Chen, S. and Quan, X., 2016. Fabrication of TiO2 nanofiber membranes by a simple dip-coating technique for water treatment. *Surface and Coatings Technology*, 298, pp.45–52.

Zhao, D.L. and Chung, T.-S., 2018. Applications of carbon quantum dots (CQDs) in membrane technologies: A review. *Water Research*, 147, pp.43–49.

Zhu, J., Zhang, Q., Zheng, J., Hou, S., Zhang, S. and Li, S., 2017. Correlation of the polymer hydrophilicity and membrane fabrication process on the properties of asymmetric membranes in a vapor-induced phase-inversion process. *Journal of Applied Polymer Science*, 134(15), pp.1–11.

Zhu, S. and Wang, D., 2017. Photocatalysis: Basic Principles, Diverse Forms of Implementations and Emerging Scientific Opportunities. *Advanced Energy Materials*, 7(23), p.1700841.

APPENDICES

APPENDIX A: Crystallite Size Calculation of TiO_2 and Hybrid Photocatalysts Based on XRD Analysis

Scherrer's Equation:

$$D = \frac{K\lambda}{\beta cos\theta} \tag{3.1}$$

where

D = crystallite size

K = Scherrer's constant, 0.89

λ = wavelength of target, 1.54 Å

β = Full Width of Half Maximum (FWHM)

θ = angle between the beam and the normal to the reflecting plane

Sample Calculation for TiO_2 at peak 1:

$$D = \frac{0.89 \times 0.154\ nm}{0.0209\cos(12.66)}$$

$$= 6.73\ nm$$

Table A-1: Calculations of Average Crystallite Sizes of TiO_2 and Hybrid Photocatalysts Based on XRD Analysis.

Sample	**2θ (º)**	**θ (º)**	**Cos θ (º)**	**FWHM (º)**	**FWHM (rad)**	**Crystallite Size, D (nm)**	**Average Crystallite Size (nm)**
TiO_2	25.32	12.66	0.9757	1.1967	0.0209	6.73	20.56
	36.32	18.16	0.9502	0.5200	0.0091	15.90	
	37.99	19.00	0.9455	1.4200	0.0248	5.85	
	48.00	24.00	0.9136	1.3367	0.0233	6.43	
	54.55	27.27	0.8888	2.0100	0.0351	4.40	
	62.65	31.33	0.8542	1.4200	0.0248	6.48	
	63.94	31.97	0.8483	0.0800	0.0014	115.76	
	70.24	35.12	0.8179	1.1000	0.0192	8.73	
	75.23	37.62	0.7921	1.3800	0.0241	7.19	
	78.22	39.11	0.7759	0.3600	0.0063	28.12	
1HPC	25.36	12.68	0.9756	1.1847	0.0207	6.80	9.13
	36.62	18.31	0.9494	0.7600	0.0133	10.89	
	37.99	19.00	0.9455	1.2600	0.0220	6.59	
	48.00	24.00	0.9135	1.3900	0.0243	6.19	
	54.58	27.29	0.8887	2.0333	0.0355	4.35	
	62.70	31.35	0.8540	1.3600	0.0237	6.76	
	69.04	34.52	0.8239	1.0000	0.0175	9.53	
	70.08	35.04	0.8188	1.1600	0.0202	8.27	
	75.25	37.63	0.7920	1.4200	0.0248	6.99	
	76.30	38.15	0.7864	0.4000	0.0070	24.97	

Table A-1 (Continued)

Sample	2θ (º)	θ (º)	Cos θ (º)	FWHM (º)	FWHM (rad)	Crystallite Size, D (nm)	Average Crystallite Size (nm)
2HPC	25.33	12.66	0.9757	1.1779	0.0206	6.84	13.35
	36.24	18.12	0.9504	0.6000	0.0105	13.78	
	38.00	19.00	0.9455	1.4233	0.0248	5.84	
	46.60	23.30	0.9184	0.2800	0.0049	30.55	
	54.57	27.28	0.8888	2.0667	0.0361	4.28	
	62.69	31.35	0.8541	1.4600	0.0255	6.30	
	65.05	32.52	0.8432	0.5500	0.0096	16.94	
	68.98	34.49	0.8242	1.0800	0.0188	8.83	
	70.46	35.23	0.8168	0.5600	0.0098	17.17	
	78.22	39.11	0.7759	0.4400	0.0077	23.01	
3HPC	25.33	12.67	0.9757	1.1584	0.0202	6.95	16.32
	36.90	18.45	0.9486	0.7200	0.0126	11.50	
	37.97	18.99	0.9456	1.3000	0.0227	6.39	
	48.02	24.01	0.9135	1.2900	0.0225	6.66	
	54.55	27.28	0.8888	1.9800	0.0346	4.46	
	62.71	31.36	0.8540	1.4600	0.0255	6.30	
	63.98	31.99	0.8481	0.1600	0.0028	57.89	
	68.58	34.29	0.8262	0.2000	0.0035	47.54	
	70.22	35.11	0.8180	1.0800	0.0188	8.89	
	75.27	37.64	0.7919	1.5000	0.0262	6.61	

Table A-1 (Continued)

Sample	**2θ (º)**	**θ (º)**	**Cos θ (º)**	**FWHM (º)**	**FWHM (rad)**	**Crystallite Size, D (nm)**	**Average Crystallite Size (nm)**
4HPC	25.33	12.67	0.9757	1.1800	0.0206	6.82	9.87
	37.02	18.51	0.9483	0.8800	0.0154	9.41	
	37.99	19.00	0.9455	1.3700	0.0239	6.06	
	48.02	24.01	0.9135	1.3800	0.0241	6.23	
	54.58	27.29	0.8887	1.9600	0.0342	4.51	
	62.73	31.37	0.8539	1.4200	0.0248	6.48	
	68.96	34.48	0.8243	0.9600	0.0168	9.93	
	69.94	34.97	0.8195	1.2400	0.0216	7.73	
	75.29	37.65	0.7918	1.7000	0.0297	5.84	
	76.38	38.19	0.7860	0.2800	0.0049	35.70	

APPENDIX B: Particle Size of Pure TiO_2 Obtained from Zetasizer

Table B-1: Mean Particle Sizes of TiO_2 Obtained from Zeta Analysis.

Sample	**Particle Size (nm)**	**Mean Particle Size (nm)**	**Standard Deviation**
Pure TiO_2	795.6 788.9 803.3	795.9	7.2

APPENDIX C: Calculations of Paracetamol Removal Percent by Hybrid Photocatalyst and Photocatalytic Membranes under Visible Light Irradiation

Paracetamol removal percent can be calculated by using Equation 3.4:

$$\%\,Removal = \frac{Abs_i - Abs_f}{Abs_i} \times 100\% \tag{3.4}$$

where

Abs_i = initial absorption of paracetamol solution

Abs_f = final absorption of paracetamol solution

Sample Calculation for 1HPC:

Abs_i at 0 min = 0.6953

Abs_f at 60 min = 0.3201

$$\begin{aligned}\%\,Removal_{60\,min} &= \frac{Abs_i - Abs_f}{Abs_i} \times 100\% \\ &= \frac{0.6953 - 0.3201}{0.6953} \times 100\% \\ &= 53.96\%\end{aligned}$$

Therefore, 1HPC achieved 53.96% paracetamol removal after 60 minutes of photodegradation under visible light irradiation. Table C-1 summarizes the calculations of paracetamol removal percentage of powdered photocatalysts.

Sample Calculation for 0.1PESPCM:

Abs_i at 0 min = 0.7561

Abs_f at 180 min = 0.6212

$$\%\,Removal_{180\,min} = \frac{Abs_i - Abs_f}{Abs_i} \times 100\%$$

$$= \frac{0.7561 - 0.6212}{0.7561} \times 100\%$$

$$= 17.84\%$$

Therefore, 0.1PESPCM achieved 17.84% paracetamol removal after 180 minutes of photodegradation under visible light irradiation. Table C-2 summarizes the calculations of paracetamol removal percentage of photocatlytic membranes.

Table C-1: Paracetamol Removal Percentage by Hybrid Photocatalysts based on UV-Visible Spectrophotometer Absorption.

Sample	**Abs at 0 min**	**Abs at 60 min**	**Paracetamol Removal (%)**
TiO_2	0.6370	0.6170	3.14
1HPC	0.6953	0.3201	53.96
2HPC	0.7323	0.2761	62.30
3HPC	0.7653	0.2502	67.31
4HPC	0.7660	0.4868	36.45

Table C-2: Paracetamol Removal Percentage by Photocatalytic Membranes based on UV-Visible Spectrophotometer Absorption.

Sample	**Abs at 0 min**	**Abs at 180 min**	**Paracetamol Removal (%)**
1.0PESBM	1.1391	1.1279	0.98
0.1PESPCM	0.7561	0.6212	17.84
0.2PESPCM	1.1296	0.9141	19.08
0.3PESPCM	0.7913	0.4620	41.62

APPENDIX D: Photocatalytic Rate Constant Calculation by Applying Photodegradation Kinetics

Rate constant can be obtained by Photodegradation Kinetics.

$$\ln\frac{C_o}{C} = kt \tag{3.5}$$

where

C_o = initial paracetamol concentration

C = final paracetamol concentration

k = rate constant

t = irradiation time

Sample Calculation for 1HPC:

C_o at 0 min = 0.6953

C at 15 min = 0.5182

C at 30 min = 0.4174

C at 45 min = 0.3606

C at 60 min = 0.3201

$$ln\frac{C_o}{C_{15min}} = ln\frac{0.6953}{0.5182} = 0.2940$$

$$ln\frac{C_o}{C_{30min}} = ln\frac{0.6953}{0.4174} = 0.5103$$

$$ln\frac{C_o}{C_{45min}} = ln\frac{0.6953}{0.3606} = 0.6566$$

$$ln\frac{C_o}{C_{60min}} = ln\frac{0.6953}{0.3201} = 0.7757$$

Table D-1 summarizes the computation results of $\ln\frac{C_o}{C}$ for powdered photocatalysts.

Sample Calculation for 1.0PESPCM:

C_o at 0 min = 0.7561

C at 30 min = 0.7239

C at 60 min = 0.6975

C at 90 min = 0.6821

C at 120 min = 0.6609

C at 150 min = 0.6365

C at 180 min = 0.6212

$$ln\frac{C_o}{C_{30min}} = ln\frac{0.7561}{0.7239} = 0.0435$$

$$ln\frac{C_o}{C_{60min}} = ln\frac{0.7561}{0.6975} = 0.0807$$

$$ln\frac{C_o}{C_{90min}} = ln\frac{0.7561}{0.6821} = 0.1030$$

$$ln\frac{C_o}{C_{120min}} = ln\frac{0.7561}{0.6609} = 0.1346$$

$$ln\frac{C_o}{C_{150min}} = ln\frac{0.7561}{0.6365} = 0.1722$$

$$ln\frac{C_o}{C_{180min}} = ln\frac{0.7561}{0.6212} = 0.1965$$

Table D-2 summarizes the computation results of $\ln\frac{C_o}{C}$ for photocatalytic membranes.

Table D-1: Calculations of ln C_o/C by Powdered Photocatalytic Nanoparticles based on UV-Visible Spectrophotometer Absorption.

Photodegradation Time (min)	**UV-Visible Spectrophotometer Absorption**					**ln C_o/C**				
	TiO_2	**1HPC**	**2HPC**	**3HPC**	**4HPC**	**TiO_2**	**1HPC**	**2HPC**	**3HPC**	**4HPC**
0	0.6370	0.6953	0.7323	0.7653	0.7660	0	0	0	0	0
15	0.6320	0.5182	0.4682	0.5407	0.6264	0.0079	0.2940	0.4473	0.3474	0.2012
30	0.6020	0.4174	0.3549	0.4130	0.5642	0.0565	0.5103	0.7244	0.6168	0.3058
45	0.6080	0.3606	0.3030	0.3081	0.5206	0.0466	0.6566	0.8825	0.9098	0.3862
60	0.6170	0.3201	0.2761	0.2502	0.4868	0.0319	0.7757	0.9754	1.1180	0.4533

Table D-2: Calculations of ln C_o/C by Photocatalytic Composite Membranes based on UV-Visible Spectrophotometer Absorption.

Photodegradation Time (min)	**UV-Visible Spectrophotometer Absorption**				**ln C_o/C**			
	Bare PES	**0.1PESPCM**	**0.2PESPCM**	**0.3PESPCM**	**Bare PES**	**0.1PESPCM**	**0.2PESPCM**	**0.3PESPCM**
0	1.1391	0.7561	1.1296	0.7913	0	0	0	0
30	1.1300	0.7239	1.0801	0.6847	0.0080	0.0435	0.0448	0.1447
60	1.1299	0.6975	1.0340	0.6325	0.0081	0.0807	0.0884	0.2240
90	1.1235	0.6821	1.0117	0.5988	0.0138	0.1030	0.1102	0.2787
120	1.1227	0.6609	0.9936	0.5455	0.0145	0.1346	0.1283	0.3720
150	1.1300	0.6365	0.9521	0.5020	0.0080	0.1722	0.1709	0.4551
180	1.1279	0.6212	0.9141	0.4620	0.0099	0.1965	0.2117	0.5381

APPENDIX E: Calculations of Mass Gain and Grafting Yield

Mass gain (M) and grafting yield (G) upon the incorporation of photocatalysts nanoparticles onto bare PES membrane surface can be calculated by Equation 3.2 and Equation 3.3 respectively.

$$M\ (\%) = \frac{m_f - m_i}{m_i} \tag{3.2}$$

where

M = mass gain, %

m_i = mass of membrane before grafting, g

m_f = mass of grafted and dried membrane, g

$$G\ (\%) = \frac{m_f - m_i}{m_c} \tag{3.3}$$

where

G = grafting yield, %

m_i = mass of membrane before grafting, g

m_f = mass of grafted and dried membrane, g

m_c= mass of photocatalysts added to dipping solution, g

Sample Calculations for 0.1PESPCM:

m_i = 0.056 g

m_f = 0.069 g

m_c = 0.050 g

$$\begin{aligned} Mass\ gain, M\ (\%) &= \frac{m_f - m_i}{m_i} \\ &= \frac{0.069\ g - 0.056\ g}{0.056\ g} \\ &= 0.2321 \\ &= 23.21\% \end{aligned}$$

$$Grafting\ Yield, G\ (\%) = \frac{m_f - m_i}{m_c}$$

$$= \frac{0.069\ g - 0.056\ g}{0.05\ g}$$

$$= 0.26$$

$$= 26\%$$

Table E-1: Calculations of Mass Gain, *M* and Grafting Yield, *G* of Photocatalytic Membranes.

Sample	**m_c (g)**	**m_i (g)**	**m_f (g)**	**$m_f - m_i$ (g)**	**M (%)**	**G (%)**
0.1PESPCM	0.05	0.056	0.069	0.013	23.21	26.00
0.2PESPCM	0.10	0.058	0.073	0.015	25.86	15.00
0.3PESPCM	0.15	0.055	0.077	0.022	40.00	14.7

APPENDIX F: Calculations of Pure Water Flux (PWF) and Permeability

PWF of membrane can be calculated by applying Equation 3.6:

$$J = \frac{V}{A\,\Delta t} \tag{3.6}$$

where

J = pure water flux, L/m^{2}h

V = volume of permeated water, L

A = membrane area, 0.00146 m^2

Δt = permeation time, h

m = mass of permeate, kg

ρ = density of water, 997 kg/m^3

Permeability of membrane can be calculated by using Equation 3.7:

$$Permeability = \frac{J}{TMP} \tag{3.7}$$

where

J = pure water flux, L/m^{2}h

TMP = transmembrane pressure (2 bar)

<u>Sample Calculations for 0.5PESBM:</u>

For Sample Membrane 1:

Average m_1 = 1.3443 g

Δt = 30 s

ρ = 997 kg/m^3

$$V_1 = \frac{m_1}{\rho}$$

$$= \frac{(1.3443\ g) \times \left(\frac{1\ kg}{1000\ g}\right)}{997\,\frac{kg}{m^3}}$$

$$= 1.3483 \times 10^{-6}\ m^3$$

$$J_1 = \frac{V_1}{A\ \Delta t}$$

$$= \frac{(1.3483\ \times 10^{-6}\ m^3) \times \left(\frac{1000\ L}{1\ m^3}\right)}{0.00146\ m^2 \times 30\ s \times \frac{1\ h}{3600\ s}}$$

$$= 110.82\ \frac{L}{m^2h}$$

$$Permeability_1 = \frac{J_1}{TMP}$$

$$= \frac{110.82\frac{L}{m^2h}}{2\ bar}$$

$$= 55.41\ \frac{L}{m^2h \cdot bar}$$

Using the same calculation method, permeability of 0.5PESBM Sample 2 and 0.5PESBM Sample 3 were obtained:

$$Permeability_2 = 71.87\ \frac{L}{m^2h \cdot bar}$$

$$Permeability_3 = 73.37\ \frac{L}{m^2h \cdot bar}$$

$$Average\ permeability = \frac{55.41\ \frac{L}{m^2h\cdot bar} + 71.87\ \frac{L}{m^2h\cdot bar} + 73.37\ \frac{L}{m^2h\cdot bar}}{3}$$

$$= 66.89\ \frac{L}{m^2h \cdot bar}$$

Table F-1: Summary of Mass of Permeated Water over 900 s for 0.5PESBM, 1.0PESBM, 0.1PESPCM, 0.2PESPCM and 0.3PESPCM.

	Mass of Permeated Water, *m* (g)														
	0.5PESBM			**1.0PESBM**			**0.1PESPCM**			**0.2PESPCM**			**0.3PESPCM**		
Time (s)	**1**	**2**	**3**	**1**	**2**	**3**	**1**	**2**	**3**	**1**	**2**	**3**	**1**	**2**	**3**
30	0.82	1.88	1.83	3.57	3.79	3.07	0.07	0.05	0.02	0.03	0.02	0.05	0.02	0.01	0.02
60	1.63	1.87	1.85	3.53	3.77	3.11	0.02	0.02	0.04	0.01	0.01	0.02	0.03	0.02	0.03
90	1.09	1.85	1.85	3.53	3.77	3.05	0.01	0.03	0.01	0.02	0.01	0.01	0.02	0.01	0.02
120	1.35	1.88	1.83	3.49	3.74	3.02	0.03	0.01	0.01	0.01	0.03	0.01	0.02	0.03	0.01
150	1.59	1.80	1.83	3.47	3.74	3.01	0.01	0.01	0.02	0.03	0.01	0.03	0.01	0.01	0.01
180	1.38	1.81	1.82	3.45	3.70	3.02	0.04	0.02	0.03	0.02	0.02	0.01	0.03	0.01	0.02
210	1.37	1.82	1.84	3.42	3.72	2.97	0.01	0.01	0.01	0.02	0.01	0.02	0.01	0.02	0.01
240	1.37	1.79	1.78	3.40	3.69	2.96	0.01	0.04	0.01	0.01	0.03	0.01	0.03	0.01	0.03
270	1.37	1.79	1.83	3.35	3.69	2.93	0.01	0.02	0.02	0.03	0.01	0.01	0.01	0.01	0.01
300	1.38	1.77	1.81	3.34	3.65	2.92	0.01	0.01	0.05	0.01	0.04	0.01	0.01	0.02	0.03
330	1.36	1.78	1.80	3.35	3.67	2.91	0.04	0.05	0.01	0.04	0.01	0.03	0.02	0.01	0.01
360	1.38	1.77	1.80	3.28	3.65	2.89	0.01	0.01	0.02	0.01	0.01	0.02	0.01	0.02	0.02
390	1.37	1.75	1.79	3.26	3.62	2.88	0.02	0.03	0.01	0.03	0.03	0.01	0.02	0.01	0.01
420	1.33	1.74	1.79	3.26	3.63	2.86	0.01	0.01	0.01	0.01	0.01	0.03	0.01	0.03	0.02
450	1.37	1.74	1.79	3.22	3.61	2.81	0.03	0.02	0.03	0.02	0.01	0.01	0.01	0.01	0.03

Table F-1 (Continued)

480	1.35	1.73	1.76	3.18	3.59	2.83	0.01	0.01	0.07	0.01	0.01	0.01	0.03	0.01	0.01
510	1.36	1.72	1.78	3.18	3.58	2.80	0.01	0.03	0.01	0.01	0.02	0.01	0.01	0.01	0.01
540	1.36	1.72	1.77	3.15	3.60	2.80	0.03	0.01	0.01	0.02	0.01	0.01	0.03	0.02	0.01
570	1.35	1.70	1.76	3.14	3.54	2.76	0.01	0.01	0.03	0.02	0.03	0.05	0.01	0.01	0.02
600	1.35	1.71	1.76	3.08	3.54	2.79	0.01	0.01	0.01	0.01	0.01	0.01	0.01	0.01	0.01
630	1.36	1.69	1.71	3.09	3.55	2.71	0.01	0.02	0.02	0.02	0.01	0.02	0.01	0.03	0.01
660	1.34	1.68	1.80	3.07	3.54	2.71	0.01	0.04	0.02	0.02	0.02	0.01	0.01	0.01	0.03
690	1.36	1.72	1.73	3.02	3.51	2.69	0.04	0.01	0.01	0.01	0.01	0.01	0.01	0.01	0.01
720	1.33	1.65	1.74	3.00	3.51	2.65	0.01	0.05	0.01	0.04	0.02	0.04	0.03	0.01	0.01
750	1.33	1.67	1.75	3.00	3.48	2.57	0.01	0.01	0.02	0.01	0.01	0.01	0.01	0.02	0.02
780	1.33	1.67	1.72	3.01	3.52	2.55	0.03	0.02	0.01	0.02	0.04	0.01	0.01	0.01	0.01
810	1.34	1.65	1.72	2.93	3.47	2.56	0.01	0.03	0.04	0.03	0.01	0.02	0.02	0.01	0.01
840	1.32	1.66	1.73	2.93	3.45	2.49	0.02	0.05	0.02	0.01	0.01	0.01	0.01	0.03	0.02
870	1.34	1.65	1.72	2.90	3.48	8.74	0.01	0.01	0.01	0.02	0.01	0.02	0.02	0.01	0.01
900	1.35	1.65	1.71	2.92	3.43	2.42	0.06	0.01	0.05	0.01	0.03	0.01	0.02	0.02	0.01
Average	1.3443	1.7437	1.7800	3.2173	3.6077	3.0160	0.0203	0.0220	0.0213	0.0187	0.0170	0.0177	0.0167	0.0150	0.0160

Table F-2: Results of PWF and Permeability Calculations for 0.5PESBM, 1.0PESBM, 0.1PESPCM, 0.2PESPCM and 0.3PESPCM.

	0.5PESBM			**1.0PESBM**			**0.1PESPCM**			**0.2PESPCM**			**0.3PESPCM**		
	1	**2**	**3**	**1**	**2**	**3**	**1**	**2**	**3**	**1**	**2**	**3**	**1**	**2**	**3**
Average *m* (g)	1.3443	1.7437	1.7800	3.2173	3.6077	3.0160	0.0203	0.0220	0.0213	0.0187	0.0170	0.0177	0.0167	0.0150	0.0160
PWF (L/m^{2}h)	110.83	143.75	146.74	265.23	297.41	248.64	1.68	1.81	1.76	1.54	1.40	1.46	1.37	1.24	1.32
Permeability (L/m^{2}h·bar)	55.41	71.87	73.37	132.62	148.71	124.32	0.84	0.91	0.88	0.77	0.70	0.73	0.69	0.62	0.66
Average Permeability (L/m^{2}h·bar)	66.89			135.21			0.87			0.73			0.65		
Standard Deviation	9.96			12.40			0.03			0.03			0.03		